공학박사 학위논문

An investigation into the development of a high-performance and safe lithium metal anode free battery

고성능의 안전한 무음극 리튬 메탈 전지 개발을 위한 연구

2022년 8월

서울대학교 대학원
재료공학부

Orapa Tamwattana

An investigation into the development of a high-performance and safe lithium metal anode free battery

고성능의 안전한 무음극 리튬 메탈 전지 개발을 위한 연구

지도교수 강 기 석

이 논문을 공학박사 학위논문으로 제출함
2022 년 8 월

서울대학교 대학원
재료공학부
Orapa Tamwattana

Orapa Tamwattana의 박사 학위논문을 인준함
2022년 6월

위 원 장 장호원 (인)
부위원장 강기석 (인)
위 원 최장욱 (인)
위 원 임종우 (인)
위 원 **Nonglak Meethong** (인)

Abstract

The demand for energy is growing at an exponential rate. Greater use of energy has led to environmental challenges such as global climate change and increased levels of atmospheric carbon dioxide. As a result, alternative energy resources are an option to replace energy derived from fossil fuels. However, all of these alternative energy resources supply power intermittently, making it harder for people to use electricity efficiently. Energy storage devices that that are efficient, small, powerful, and portable are required. Also, existing technology designed to supply portable electric power, such as for mobile phones, laptops, and electric cars, must be developed. The current energy storage methods, such as lithium- ion batteries, are inefficient. So, new battery types are needed to meet the ever-increasing demand for electricity.

Another option is to use lithium metal anode-free batteries. Lithium metal anode-free batteries are the "holy grail" of high energy storage technology. This is due to their low weight, high capacity and low voltage. However, short cycle life, low Coulombic efficiency, and their somewhat hazardous characteristics make Li metal anode-free batteries difficult to use. All of these issues stem from internal battery issues. The lithium ions have nowhere to occupy since this battery is hostless. This means Li-ions can only be electroplated on Li metal or current collector surfaces. The anode's basic process may result in non-uniform lithium ion deposition. Lithium plating non-uniformities cause rapid electrolyte and Li source consumption, resulting in rapid electrolyte depletion and short cycle life with low Coulombic efficiency. Additionally, plating and stripping irregularly can cause Li dendrites to grow, which can penetrate the separator and reach the cathode, causing

short circuiting and runaway Joule heating.

There are two basic causes of non-uniform Li- ion deposition. First, a pristine current collector or Li- foil anode has rough surfaces that cause local current densities on the current collector surface. These irregularities guide localized Li- ion deposition. **Second**, a non-uniform spontaneous SEI layer is an uncontrollable quality. A rough SEI layer leads to uneven Li deposition. **Finally**, there is a serious safety issue. After multiple cycles that consume electrolyte and the lithium source, there is an increased risk of Li-dendrite development that breaches the separator and approaches the cathode. The resulting short circuit transfers electrons through the dendrite, causing a thermal runaway and explosion.

Based on the three severe drawbacks of Li-metal anode free batteries, the investigator conducted extensive research on these issues. **Part I** of the study focuses on guiding Li-ions to a uniform deposition using two strategies. **First,** a high dielectric constant SEI was employed to prevent localized current distribution. Using this approach, lithium plating will be more uniform under an SEI layer with a high polarity polymer. Coating a current collector with a high-dielectric SEI reduces the overpotential between the surfaces, lowers the local current density, and suppresses lithium protrusions. A PVDF (polyvinylidene difluoride) dielectric SEI allows for control of the PVDF crystallinity and, hence, Li-ion deposition. Furthermore, when dielectric nanoparticles are added to PVDF films, a high-dielectric ®-PVDF phase is created during film formation (LiF@PVDF). This promotes uniform lithium deposition/stripping in an anode-free half-cell. **Second**, the effect of the non-uniform SEI layer on the performance of the batteries is examined. In lithium batteries and anode-free batteries, the solid electrolyte interface (SEI) is one of the most significant components necessary for

electrochemical cycle efficiency. The reduction and decomposition of electrolyte near-surface metallic lithium occurs spontaneously due to the very low negative electrochemical potential of metallic lithium. The chemical composition of the organic and inorganic nanocrystalline SEI layer is uncontrollable. The coexistence of organic and inorganic nanocrystals results in uneven mechanical properties and ion conductivity in the SEI layer, promoting uncontrolled lithium deposition. This leads to poor Coulombic efficiency, a short cycle life, and a risk of fire in lithium batteries and anode-free batteries. A monolithic SEI layer is established in this study using simple electrochemical polishing, which eliminates organic nanocrystals, leaving just a monolithic inorganic nanocrystalline layer. This provides rigidity and homogenous ionic conductivity to the SEI layer. Extensive cryo-electron microscopy (Cryo-TEM) characterization, corroborated by cryogenic electron energy loss spectroscopy (EELS) and in-depth XPS profile research, reveals a flawless monolithic inorganic SEI layer that allows for homogenous lithium deposition and dissolution. In **Part II,** a lithium rechargeable battery system with an auxiliary electrode is presented that can detect internal short-circuits and prevent cell failure by inhibiting lithium metal dendritic growth. Based on this concept, an auxiliary electrode was designed that serves as both a safety sensor and a lithium scavenger. A flexible and self-standing auxiliary electrode can effectively alert the danger of a short circuit in real-time with no additional dendrite growth. This discovery may lead to new applications for safe rechargeable lithium metal batteries.

In conclusion, it is this researcher’s hope that these studies will provide valuable scientific knowledge, thereby inspiring others in development of a new generation of Li metal anode-free batteries. Finally, it is hoped that these types of batteries can

be employed commercially to move our planet toward a more sustainable environment using technology for humanity.

Keywords: Li metal anode, anode-free battery, Li dendrite, artificial SEI layer for anode, electrochemistry, Secondary rechargeable batteries.

Student number: 2016-22080

List of Figures

the ratio of SEI Li+ to unreacted metallic Li.

Figure 2.1.2.1: The FT-IR analysis peak area at 764 and 840 cm^{-1} of (a) α-PVDF. (b) β-PVDF and (c) LiF@PVDF samples

Figure 2.1.3.1. Schematic illustration of molecular level of PVDF and comparison of the properties of α-PVDF, β-PVDF and LiF@PVDF coated on Cu foil showing (a) Molecular structure of α-PVDF, β-PVDF and LiF@PVDF. (b) FT-IR spectra, (c) the dielectric constants, and (d) stress-strain curves. (e-g) Top view SEM images of pristine (e) α-PVDF, (f) β-PVDF, and (g) LiF@PVDF samples.

Figure 2.1.3.2. FT-IR spectra of α-PVDF, β-PVDF and LiF@PVDF

Figure 2.1.3.3 (a) FT-IR spectra of LiF@PVDF samples with different mass ratio. (b) EIS plots, (c) cycle stability, and (d) average discharge overpotential of Li/LiF@PVDF@Cu cells with different mass ratio. Though a trace amount of α-PVDF is observed for the β-PVDF and 10% LiF containing PVDF composite, we could eliminate the remaining α phase of PVDF with the ratio of LiF over 30%.These results clearly infer that sufficient amount of LiF is needed to induce high-dielectric film and thus improve electrochemical stability of Li deposition; however, the excess amount of LiF is also not desirable for cell performances showing high resistance and overpotential, leading to poor cycle stability.

Figure 2.1.3.4. (a) XRD patterns of LiF nanoparticles in a LiF@PVDF layer. (b)

loss tangent, (c) dielectric loss and (d) A.C. conductivity of α-PVDF, β-PVDF and LiF@PVDF

Figure 2.1.3.5. Properties of PVDF coatings: (a-c) cross-sectional SEM images of as-prepared αPVDF, □-PVDF and LiF@PVDF , respectively, coated on Cu foil, and, (d-f) bottom view SEM image of the α-PVDF, □-PVDF and LiF@PVDF coating taken off of the Cu substrate, respectively.

Figure 2.1.3.6. Comparison of morphologies of deposited Li on bare Cu for α-PVDF, β-PVDF and LiF@PVDF at various capacity loadings. (a-d) SEM images after depositing Li on bare Cu foils, (e-h) α-PVDF, (i-l) β-PVDF, and (mp) LiF@PVDF at 0.5, 1, 5 and 10 mAh cm^{-2}, respectively. The typical filamentary growth of lithium metal on the current collector begin to appear from the loading capacity of 5 mAh cm^{-2} for the reference bare Cu and the α-PVDF samples.

Figure 2.1.3.7. Cross-sectional SEM images of Li-deposited on bare Cu foil, α-PVDF, β-PVDF and LiF@PVDF. (a-d) cross-sectional SEM images after depositing Li on bare Cu foils at 0.5, 1, 5 and 10 mAh/cm^2, respectively. (e-h) SEM images after depositing Li on α-PVDF at 0.5, 1, 5 and 10 mAh/cm^2, respectively. (i-l) SEM images after depositing Li on β-PVDF at 0.5, 1, 5 and 10 mAh/cm^2, respectively. (m-p) SEM images after depositing Li on LiF@PVDF at 0.5, 1, 5 and 10 mAh/cm^2, respectively.

Figure 2.1.3.8. (a) is the comparison ideal thickness between Li metal thickness and LiF@PVDF (b) Table of ideal thickness.

Figure 2.1.3.9. Cross-sectional SEM images and EDS spectra of Li-deposited on bare Cu foil and LiF@PVDF. (a-d) Cross-sectional SEM images and EDS spectra after depositing Li on bare Cu foils at 0.5, 1, 5 and 10 mAh/cm^2, respectively. (e-h) EDS spectra after depositing Li on LiF@PVDF at 0.5, 1, 5 and 10 mAh/cm^2, respectively.

Figure 2.1.3.10. Electrochemical characterizations showing (a-c) CE at current densities of 1, 2 and 5 mA cm^{-2}, respectively, (d-f) voltage versus areal capacity profiles of LiF@PVDF at selected cycles for Li deposition/stripping at current densities of 1, 2 and 5 mA cm^{-2}, respectively.

Figure 2.1.3.11. Electrochemical properties of Li/Cu cells with bare Cu and LiF@PVDF coated Cu. Coulombic efficiency with cycling under the utilization of areal capacity of (a) 1 mAh/cm^2 and (b) 3 mAh/cm^2. Voltage profile of Li/LiF@PVDF@Cu cells at selected cycles the utilization of areal capacity of (c) 1 mAh/cm^2 and (d) 3 mAh/cm^2. A current density of 1 mA/cm^2 was applied for all tested cells.

Figure 2.1.3.12. SEM images of lithium morphology of cells after 50 cycles. (a-b) the morphology after 50 cycles of bare Cu, top and cross-sectional views, respectively. (c-d) the morphology after 50 cycles of a LiF@PVDF coating, top and cross sectional views, respectively.

Figure 2.1.3.13. Cycle properties of $LiFePO_4$/Cu and $LiFePO_4$/LiF@PVDF cells

(a) at a 0.5C rate and (b) 1C rate. Voltage profile of (c) $LiFePO_4$/Cu cells and (d) $LiFePO_4$/LiF@PVDF cells at selected cycles.

Figure 2.1.3.14. Morphological characterization of the cross-section of pristine LiF@PVDF coated at the thicknesses of (a) 2.5, (b) 6 and (c) 13 μm. Morphological characterization of the cross-section of pristine LiF@PVDF coated at the thicknesses of (d) 2.5, (e) 6 and (f) 13 μm. (g) Impedance spectra of LiF@PVDF samples with different coating thickness. (h) Cycling stability and (i) average discharge overpotential of Li/LiF@PVDF@Cu cells during cycling. The increase in the thickness of polymer films results in the increase in charge transfer impedances, which infers that the thickness of polymer films can affect the transport property of the film. The beneficial effect of dielectric layer could be compensated by the increase in impedance if the polymer coating becomes too thick so that the transport property through the coating is weakened.

Figure 2.1.3.15. Li plating and stripping behaviors at practical capacity loadings of LiF@PVDF. (a) voltage profile at a capacity loading of 5 mAh cm^{-2}, (iv) cross-sectional SEM images showing reversibility of Li plating and stripping according to stages i-v of the voltage profile in (a), (b) voltage profile at a capacity loading of 10 mAh cm^{-2}, (i-v) cross-sectional SEM images showing reversibility of Li plating and stripping according to stages i-v of the voltage profile in (b).

Figure 2.1.3.16. (a) Voltage profiles of Li deposition showing the interface overpotentials of bare Cu, α-PVDF, β-PVDF and LiF@PVDF samples, (b) Impedance spectra showing charge-transfer resistances of α-PVDF, β-PVDF and

LiF@PVDF samples, (c) The numerical system simulate the lithium concentration gradients on the artificial SEI polymer coated on bare Cu with the overpotentials of 0.1 V and 0.3 V. Schematic illustration of theoretical elucidation of the growth mechanisms of Li-ion depletion and mitigating the surface concentration difference during concentration polarization, (d) without high dielectric constant artificial SEI, and (e) with high dielectric constant artificial SEI.

Figure 2.1.3.17. (a) Li 1s, (b) F 1s and (c) C 1s XPS spectra for bare Cu after 10 cycles in Li/Cu cells. (d) Li 1s, (e) F 1s and (f) C 1s XPS spectra of Cu foils with peeling off LiF@PVDF film after 10 cycles in Li/LiF@PVDF@Cu cells. The binding energy was calibrated with C 1s at 284.8 eV.

Figure 2.1.3.18. Schematic diagram of the numerical model system used to simulate the lithium concentration gradients on the artificial SEI polymer coated on bare Cu

Figure 2.2.2.1. a) Camera image of cell undergoing in-situ optical microscopy deposition/ dissolution with a current density of 40 $mAcm^2$ and 0.5 mAh/cm^2. b) Schematic of cell configuration for in-situ OM transparent cell. These experiments have been tested under Argon atmosphere.

Figure 2.2.3.1. Cryogenic electron microscopy (Cryo-TEM) analysis of SEI nanostructure formed at different electrochemical stripping at 1V. and 2V. and XPS analysis on the SEI layer after Li stripping at the 1^{st} cycle in Cu/Li cells. a) and d), Li metal deposited on the 200-Cu mesh using 1 M LiTFSi 3wt% $LiNO_3$ in

DOLDME electrolyte with 1.267 mA, for 30 minutes. Stripping Li by working potential reach 1 V (b,e) and 2 V (c,f). g) and j) Li 1s spectra for 1V and 2V stripping, respectively. h) and k) C 1s spectra for 1V and 2V stripping, respectively. The quantified atomic composition ratios of the SEI at different sputtering times i) 1V stripping and l) 2V stripping. All the XPS results were cycled by using 1 M LiTFSi 3wt% $LiNO_3$ in DOLDME electrolyte and The binding energy was calibrated with C 1s at 284.8 eV.

Figure 2.2.3.2. Electron energy loss spectroscopy (EELS) from cyro-EM characterization. a) and e), STEM image and Li K- edge spectra for SEI layer of 1V stripping. b) and f), STEM image and C K- edge spectra for SEI layer of 1V stripping. c) and g), STEM image and Li K- edge spectra for SEI layer of 2V stripping. d) and h), STEM image and C K- edge spectra for SEI layer of 2V stripping. IN all EELS analysis, the cell was cycling with 1.267 mA current density and 30-minute deposition. Electrolyte 1 M LiTFSi 3wt% $LiNO_3$ in DOLDME.

Figure 2.2.3.3. Morphology characterization of surface and cross-section after cycles. SEM images of top view of 1V stripping after 10 cycles a), 100 cycles b) and 1V cross-section view after 100 cycles c). 2V stripping after 10 cycles d) and 100 e) and 2 V cross-section after 100 cycles f). As well as, capture images of in-situ optical microscopy for 1V g) and 2V h) stripping. All morphology characterization has been done with 1 M LiTFSi 3wt% $LiNO_3$ in DOLDME electrolyte.

Figure 2.2.3.4. COMSOL simulation of Li deposition through homogeneous and

inhomogeneous SEI layer. a) , Li deposited on protuberance of Cu foil without SEI. b) , Li deposited on protuberance of Cu foil with a double layer of SEI. c), Li deposited through inhomogeneous SEI with crack layer model (SEI forming from 1V stripping). d), Li deposited through homogeneous single inner SEI layer (SEI forming from 2V). e)-i) the mechanism schematic of 1 V. and 2 V. cut off.

Figure 2.2.3.5. Electrochemical behavior of 1 Voltage and 2 Voltage cut off by Li/Cu and $LiFePO_4$ cells. All cells were cycled in 1 M LiTFSi 3wt% $LiNO_3$ in DOLDME electrolyte. a). Coulombic efficiency of Li/Cu cells cycled by 1V, 2V, and 2V 50 cycles and change to 1V, respectively, at current density 1 mA/cm^2 and areal capacity 0.5 mAh/cm^2. Voltage profiles of different cycles for Li/Cu cells cycled at 1V b) and 2V c) cut off. d), cycling performance and capacity after 50 pre-cycles of 1 and 2V stripping, respectively. e) voltage profiles of $LiFePO_4$/Cu cell at selected cycles after 50 pre-cycles of 2V stripping.

Figure 2.2.3.6. Electrochemical behavior of 1 Voltage and 2 Voltage cut off by Li/Cu cells. a) and b) coulombic efficiency of Li/Cu cells cycled by 1V and 2V at current density 3 mA/cm^2 and 5 mAh/cm^2, areal capacity 0.5 mAh/cm^2 respectively. c) and d), average charge and discharge overpotential of 1 V and 2 V, respectively, at 1 mA/cm^2 and areal capacity 0.5 mAh/cm^2.

Figure 2.2.3.7. Pre-cycling in Li/Cu cell. All the cell was cycling with 1 M LiTFSi 3wt% $LiNO_3$ in DOLDME electrolyte.

Figure 2.2.3.8. Electrochemical behavior of 1Voltage and 2 Voltage cut off by

$LiFePO_4$/Cu cells. a) cycling performance of $LiFePO_4$/Cu cells and b), capacity retention between 1V and 2V anode stripping respectively. c) and d), voltage profiles of $LiFePO_4$/Cu cell at selected cycles of 1 and 2V stripping, respectively.

Figure 3.1.1. Vertical growth rate of dendrite at various current densities. The black and blue lines represented vertical growth rate of dendrite and areal capacity, respectively. This experiment was conducted in sandwich cell. The piece of lithium foil was first pressed onto the case part of the cell and cover by customized PVDF rings (outer diameter = 16.5 mm, inner diameter = 8 mm, thickness = 100 μm). The electrolyte was dropped on the surface of lithium. Finally, the second lithium foil was plated on top of the customized PVDF. The whole cell was assembled in an Ar-filled glovebox using a CR2032-type coin cell with 300 μm thick Li foil. The estimate of vertical growth rate, with respect to the planar growth in the inner site of customizes PVDF rings, was possible by checking the time required for short-circuiting involving sudden voltage drops.

Figure 3.2.1. Schematic mechanism of an auxiliary electrode sensor for safe rechargeable lithium metal batteries. (a) In a conventional battery system, initially formed dendric seeds will grow and create an internal circuit across the separator positioned between the two electrodes, causing to voltage of the battery to drop to 0 V (*vs.* Li/Li^+). (b) With the aid of auxiliary electrode, growing lithium dendrites will reach at auxiliary electrode before they make connection with the positive electrode. Lithium dendrites will not grow further while the auxiliary electrode consumes lithium ions. The reaction of the auxiliary electrode with lithium ions signals danger before a catastrophic event occurs with no damage to the battery.

Figure 3.2.2. Images of a flexible graphite layer with 30% PVDF-HFP and 70% flake graphite composition. The pristine graphite layer was not torn and damaged by bending and folding.

Figure 3.2.3. Fabrication processes of a thin graphite layer are described step by step.

Figure 3.2.4. Typical potential profile of a graphite layer with color change of graphite by lithiation. The pristine graphite layer that is fully de-lithiated is black in color. The color of graphite layer becomes yellow with lithiation. Each cell was discharged with a current density of 10 mA g^{-1} to its cut-off voltage and disassembled to obtain graphite images.

Figure 3.2.5. The delay time that can suppress the growth of lithium dendrite depending on the current density. The larger the capacity of the auxiliary electrode, the longer the allowable dendrite growth delay time.

Figure 3.2.6. Images showing the contact angle of dropped electrolyte on (a) separator and (b) an auxiliary graphite layer. The electrolyte on the separator maintains a high contact angle for up to 60 seconds. Conversely, as soon as the electrolyte was dropped onto the graphite layer, it penetrated the graphite layer.

Figure 3.2.7. (a) Nyquist plot of a SUS-SUS symmetric cell with a graphite layer between the plates. (b) A schematic illustration of the cell configuration to measure

EIS. Due to the electronic conductivity of the graphite layer, two separator sheets on each side were used to block the electronic path. (c) Ionic conductivity is measured in various cell configurations to determine the effect of each component.

Figure 3.3.1. (a) Detailed cell configuration for *in situ* observations. (b) Images of the auxiliary electrode and positive electrode were taken over deposition time. A mossy-like lithium was observed on the copper foil that gradually grew over the time. (c) The voltage profile of both $V1_{\text{Lithium-Copper}}$ and $V2_{\text{Graphite-Lithium}}$ during electroplating on copper foil. (d) $V1_{\text{Lithium-Copper}}$ and $V2_{\text{Graphite-Lithium}}$ from 10 to 13 minutes. I Images of the area between the auxiliary electrode and negative electrode after 23 minutes. No trace of lithium deposition was observed, indicating that the mossy-like lithium did not penetrate the graphite layer.

Figure 3.3.2. (a) A schematic illustration of cell configuration for *in-situ* optical measurement. (b) Optical microscopy images of the Li-Li symmetric cell were taken in galvanostatic mode. (c) Potential curve of Li-Li symmetric cell.

Figure 3.3.3. Typical potential profile and disassembly cell image of Li-Li symmetric cell (a) without a graphite auxiliary electrode (b) with a graphite auxiliary electrode.

Figure 3.3.4. (a) Schematic of the cell configuration. (b) The first charge voltage profile with a 1000 mA g^{-1} current density and a second charge voltage profile with a 10 mA g^{-1} current density. (c) Images of separators and auxiliary electrodes from a disassembled cell.

List of Tables

Table of Contents

Chapter 1. Introduction

1.1. Research motivation and objectives

The demand for alternative energy resources is undeniably expanding. Due to global climate change, pollution, and increasing strain on fossil fuel reserves such as petroleum, experts throughout the world are focusing their efforts on creating alternative energy resources[1,2]. It is critical to have energy storage systems (ESS) in place to store electrical energy for use in a variety of devices, from electronics to electric vehicles. Additionally, the modern lifestyle of people increases the demand for electricity. As a result, development of batteries and other energy storage devices is crucial for many modern technologies. Lithium-ion batteries are the most extensively used energy storage system at present. This is because Li- ion batteries are simple to use and are safe. They have been utilized in a multitude of ways for many years [3,4]. However, it can be observed that Li -ion batteries are no longer sufficient to meet the demands of modern society. Considering a straightforward example, the utilization of lithium-ion batteries in electric vehicles is depicted in **Figure 1.1.** This demonstrates that lithium-ion batteries are incapable of powering vehicles. Electric vehicles have a range of approximately 400 kilometers, which is still insufficient in comparison to today's gasoline vehicles[5, 6]. Accordingly, there is an urgent need for new forms of electric energy storage systems. The following parameters must be addressed when designing a battery with a high gravimetric and volumetric energy density. Initially**,** the theoretical capacity of the cathode must be considered. **Second,** the difference in voltage between the cathode and anode is important. Last**,** the total weight and size of the battery pack must be determined. These three elements must be

considered in developing batteries, particularly typical Li-ion batteries. The primary mechanism by which this sort of battery operates uses the transport of lithium ions from a cathode to an anode, which implies that the amount of lithium ions in the cathode is a good measure of the battery's capacity. The greater the capacity of the cathode and anode, the more energy the battery will store. As a result, cathode development continues to be of interest and is a critical factor in the development of Li-ion batteries[7-9].

The primary role of an anode is to provide a space for the lithium ions that are released from the cathode. An anode must have the greatest possible amount of room for lithium ions per unit of battery weight to maximize the gravimetric and volumetric energy density of the battery. The anode appears to be the greatest limiting factor in battery development. This is because as the cathode's capacity increases, the anode's lithium-ion support area must concurrently rise for the battery to function properly. This indicates that batteries with high gravimetric and volumetric energy density cannot be developed only on the basis of the anode size. So, development of Li-metal anode free batteries is extremely important because they do not have an anode. This means that they will be lighter and smaller than batteries with anodes. Additionally, anode-free batteries have limitless space available to support lithium ions from the cathode. Therefore, development of high gravimetric and volumetric energy density batteries in the future will not be constrained. As illustrated in **Figure 1.1**, it is possible to develop these batteries effectively.

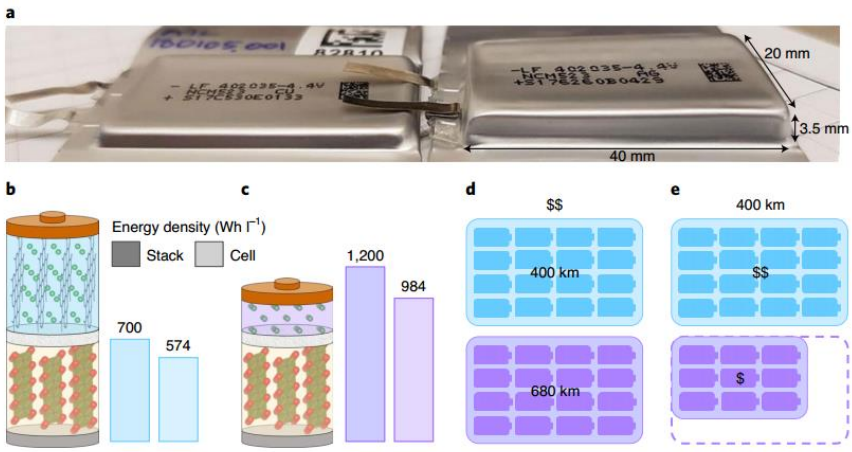

Figure. 1.1 Comparison of anode-free and lithium-ion cells. (a) Image of an anode-free (left) and Li-ion pouch cell (right) having the same capacity. Schematic of an NMC532 Li-ion (b) and an anode-free cell (c) and their respective energy densities at the stack level (double-sided positive electrode, separator, double-sided negative electrode, separator) with the cell level projected to an 18650 cell format. Illustration of Li-ion (top, blue) and anode-free (bottom, purple) battery packs made with the same number of cells and their costs (d) and for the same vehicle range (e). Reprinted by permission from springer Nature, *Nature energy*, ref 6, Copyright 2020.

1.2. Introducing Li metal anode free batteries

An anode-free battery is defined as a battery that contains no anode materials. Negatively charged material is not included in the battery, leaving only the current collector. This allows the battery to be lighter and have a higher gravimetric and volumetric energy density than a conventional Li-ion battery. With a theoretical capacity of up to 3860 mAh/g, a Li-metal battery has 0 voltage (Li/Li^+)[10-12]. This means that if Li metal is used as the negative electrode, the

potential difference in the battery has the greatest value. Although the terms, lithium-metal batteries and anode-free batteries, are difficult to grasp, both Li-metal batteries and anode-free batteries are functional and their energy calculations are similar. The amount of lithium present on the current collector surface determines whether the current collector is made of Cu or Li metal. Lithium ions can be plated or deposited on a current collector surface, rather than being inserted into or forming an alloy with the anode. Thus, the reaction of lithium ions on the anode side will be $Li^+ + e^- \rightarrow Li(s)$, and the Li metal and anode-free batteries are the same[13-15]. The only difference is the initial lithium content of the anode, as well as the initial weight of the anode, which are both the same, as illustrated in **Figure 1.2.**

While lithium-metal anode free batteries offer a high energy density, they have not been extensively used despite their superior performance. This is due to safety concerns, short cycle life, and low Coulombic efficiency, all of which are caused by the fundamental processes of Li metal function in anode-free batteries. Lithium metal anode-free batteries have no room for Li-ions. So, lithium ions travelling from the cathode will only be plated on Cu or Li metal surfaces in a process akin to electroplating[16,17]. However, lithium ions are rarely plated or deposited uniformly for several reasons. **First**, the uncontrollable rough surfaces of pristine Li metal and Cu foil, along with any other irregularities on the surface of the Cu or Li metal foil results in localized concentrations of charge and inductance on the surface. Due to the localized electric distribution, Li-ions are guided to local deposition, resulting in non-uniform plating and dendrite formation[18-20]. **Second**, a significant SEI layer forms on the surface of the anode. Once a battery is charged, an SEI layer is quickly formed and maintained. This is because the electrolyte's electrochemical

stability window is quite narrow. In most situations, the electrolyte's electrochemical stability window cannot resist potential levels below about 0.1 V[21,22]. This is another reason for the formation of SEI and irreversible by-products on the surface of the anode throughout each cycle. Most notably, SEI is an irreversible by-product of electrochemistry that has irregular chemical and mechanical properties since it occurs spontaneously. As a result, there is unequal lithium ionic conductivity and mechanical characteristics across the SEI layer, resulting in uneven lithium ion deposition across the whole layer[23-25].

There are two primary factors that contribute to uneven deposition of lithium ions on the anode, leading to the potential for significant negative impact on this type of battery. **First,** non-uniform Li plating increases the electrode's high surface area. This increased battery surface area will consume greater amounts of electrolyte with each cycle, until the battery eventually stops working because it has no more electrolyte. **Second,** uneven lithium surfaces can result in the formation of dead or inactive lithium metal. Stripping away lithium ions from non-uniformly deposited Li metal will result in a non-uniform dissolution of the lithium metal, which will promote generation of inactive lithium metal or dead lithium as a result of the process. Dead Li occurs in every cycle and consumes the Li source in the battery, resulting in the battery eventually running out of Li. Then the Coulombic efficiency of this type of battery becomes low and its lifespan is shortened, as shown in **Figure 1.3. Third,** short circuiting may occur during cycling due to Li dendrites. As a result, the by-products and dead Li metal layers become thicker, while the electrolyte is consumed in each cycle. Li dendrites form with aggressively growing sharp tips that can penetrate the separator and contacting the positive terminal of the battery[26,27]. Inducted electron flow within the battery results in generation of

heat leading to thermal runaway. The heat generated by the battery can caused a fire or an explosion, posing a threat to both human life and property[28-30]. As a result of these three detrimental factors, Li metal anode free batteries remain uncommon. Efforts have been made to resolve these three issues. The first and second difficulties arise as a result of the nature of the rough surface of plated Li-metal and the nature of the electrolyte (limited electrochemical stability window). These problems can be resolved by developing an artificial SEI layer that prevents electrolyte decomposition and promotes uniform SEI formation. This results in uniform Li deposition and additionally presents a physical SEI barrier to suppress Li-dendrite formation[31,32]. Earlier researchers attempted to explore techniques for Li-dendrite short-circuit protection by developing an application sensor for a separator that could detect Li-dendrite penetration. Prior to the Li-dendrite shorting circuiting, the sensor will issue an alert. The cathode side disables the cell prior to the battery exploding[33].

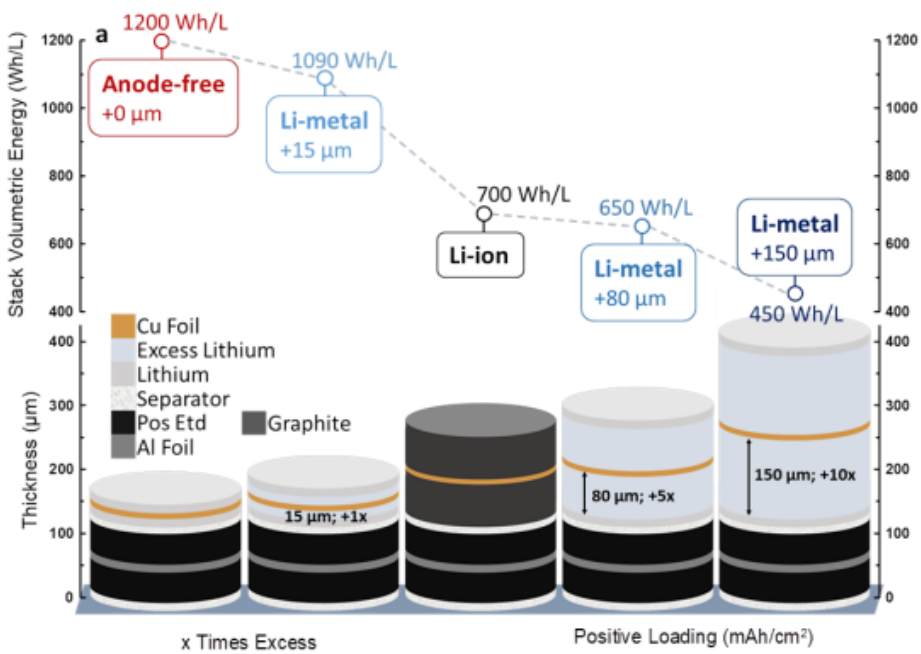

Figure 1.2. Energy density for cell stacks with various amounts of excess lithium (top) and their respective stack diagrams (bottom). Reprinted by permission from springer Nature, *Nature energy*, ref 6, Copyright 2020.

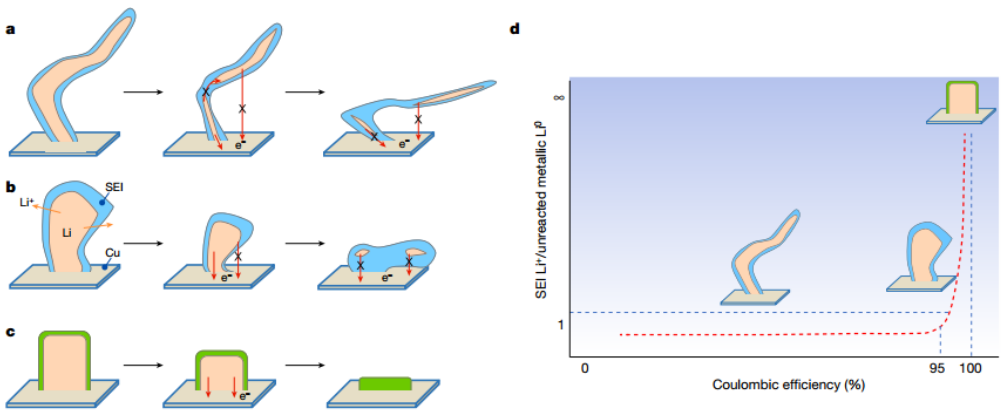

Figure. 1.3. Schematic of inactive Li formation mechanism in different electrolytes, based on TGC quantification, cryo-FIB–SEM and cryo-TEM observation. (a) Li deposits with whisker morphology and high tortuosity are more likely to lose electronic connection and maintain poor structural connection, leaving large amounts of unreacted metallic Li0 trapped in the SEI. (b) Li deposited with a large granular size and less tortuosity tends to maintain a good structural electronic connection, in which only small amounts of metallic Li0 are stuck in tortuous SEI edges. (c) An ideal Li deposit should have a columnar microstructure with a large grain size, minimum tortuosity and homogeneous distribution of SEI components, facilitating a complete dissolution of metallic Li0. (d) A general correlation of morphology of Li deposits, Coulombic efficiency and the ratio of SEI Li+ to unreacted metallic Li. Reprinted by permission from springer Nature, *Nature*, Copyright 2019.

1.3. Purpose of this research and outline

In addition to the issues described above, the fundamental concern with Li metal anode-less batteries is that they are not yet suitable for commercial use. The problem is that lithium ions cannot be consistently deposited, which leads to a variety of issues in the fabrication process. Due to fundamental limitations, lithium ions cannot be uniformly plated. These limitations include:

1. The textured surface of the pristine Li and Cu foils.
2. A non-uniform distribution of the spontaneously generated SEI layer.

As an anode-less battery continues to cycle, it consumes electrolyte and lithium to produce electrical energy. It will continue to do so until the battery short-circuits. The problems that must be address in this study will be discussed further in subsequent sections.

The research was separated into two major phases: In **Part I**, the researcher will concentrate on the two factors that contribute to uneven lithium-ion plating. The study is subdivided into two investigations, one for each of the causes: **Chapter 2.1** High-Dielectric Polymer Coating for Uniform Lithium Deposition in Anode-Free Lithium Batteries, and, **Chapter 2.2:** Leaching Organic SEI by Electrochemical Dissolution Leads to a Monolithic Inorganic SEI and Enhancing Cycle Stability for Anode-free Batteries.

The study in Chapter 2.1 aims to improve the performance of Li-metal anode batteries by addressing the problem of local electric distribution on the surface of the current collector. As part of this research, an artificial SEI layer was created utilizing artificial SEI technology. The resulting SEI layer has a dielectric constant that is quite high, whereas Li deposition aids in the uniform distribution of

electricity. This results in uniform Li deposition on the current collector surface and thus reducing the consumption of the electrolyte and the lithium source in the battery. For these reasons, battery life is increased. With the aid of a PVDF polymer, an artificial SEI was created with different dielectric constants. The polymer was occurs in three phases, α, β, and LiF@PVDF phases. All three have dielectric constants that are significantly different from one another. The differential dielectric constant was found to have a significant impact on performance that could be used to reduce the local current density on the coated surface.

The study detailed in **Chapter 2.2**, Leaching Organic SEI by Electrochemical Dissolution Leads to a Monolithic Inorganic SEI and Enhancing Cycle Stability for Anode-free Batteries, the researcher investigated the effect of a uniform SEI layer on the performance of a lithium anode-free battery. In addition to the organic and inorganic SEI layers, a multi-layer spontaneously formed SEI layer was generated on the anode. It was discovered that after many cycles, the outer organic SEI layer is more easily broken and dissolves in the electrolyte. As a result, the surface of the outer layer is uneven. The SEI layer's characteristics are also affected as a result of this unequal distribution. A lithium-ion layer was produced that was uneven, resulting in electrolyte consumption and formation of Li dendrites with subsequent short circuiting. It is necessary to remove all of the organic layer, leaving only the inorganic SEI layer. In effect, the SEI is polished until only inorganic material remains. This layer is more stable and uniform than the organic SEI layer, resulting in a more uniform Li-ion plating process. This increases the cycle stability and performance of the batteries. Throughout this study, high-tech tools including a CryO-TEM, *in-situ* optical microscope and

COMSOL simulation were utilized. Also included in Part II is a study of Li-dendrite growth prevention methods to avoid short-circuiting, which is covered in **Chapter 3**, A bifunctional auxiliary electrode for safe lithium metal batteries. In this study, sensor technology was examined to see if it could prevent the short-circuiting phenomenon from occurring. To detect short circuit phenomena in this study, a graphite separator was used as a detector. In the presence of graphite, it is established that chemical lithiation will occur spontaneously as soon as the Li metal reaches it. This gives us the opportunity to stop using the battery before a short circuit occurs. Furthermore, the graphite separator has the ability to absorb Li, allowing the life cycle to be extended until the graphite is completely lithiated.

From both studies, the mechanism of Li metal anode-free batteries is elucidated, as well as the major problems encountered, until solutions were found and the battery's capabilities were further developed. Alternatively, the investigation must be continued. Three major problems must be resolved in a single implementation to increase the battery's life cycle and make this type of battery as secure as possible. Using an artificial SEI layer with dual functions, for example, it is possible to prevent both the local distribution and the non-uniformity of spontaneously SEI at the same time.

1.4. References

1. Z. A. Needell, J. McNerney, M. T. Chang and J. E. Trancik, *Nature Energy*, 2016, **1**, 16112.

2. M. S. Dresselhaus and I. L. Thomas, *Nature*, 2001, **414**, 332-337.

3. M. Armand and J. M. Tarascon, *Nature*, 2008, **451**, 652-657.

4. J. M. Tarascon and M. Armand, *Nature*, 2001, **414**, 359-367.

5. R. Weber, M. Genovese, A. J. Louli, S. Hames, C. Martin, I. G. Hill and J. R. Dahn, *Nature Energy*, 2019, **4**, 683-689.

6. A. J. Louli, A. Eldesoky, R. Weber, M. Genovese, M. Coon, J. deGooyer, Z. Deng, R. T. White, J. Lee, T. Rodgers, R. Petibon, S. Hy, S. J. H. Cheng and J. R. Dahn, *Nature Energy*, 2020, **5**, 693-702.

7. Z.-K. Tang, Y.-F. Xue, G. Teobaldi and L.-M. Liu, *Nanoscale Horizons*, 2020, **5**, 1453-1466.

8. A. Manthiram, *Nature Communications*, 2020, **11**, 1550.

9. H. Pan, S. Zhang, J. Chen, M. Gao, Y. Liu, T. Zhu and Y. Jiang, *Molecular Systems Design & Engineering*, 2018, **3**, 748-803.

10. D. Lin, Y. Liu and Y. Cui, *Nature Nanotechnology*, 2017, **12**, 194-206.

11. X.-B. Cheng, R. Zhang, C.-Z. Zhao and Q. Zhang, *Chemical Reviews*, 2017, **117**, 10403-10473.

12. B. Liu, J.-G. Zhang and W. Xu, *Joule*, 2018, **2**, 833-845.

13. Z. Yu, H. Wang, X. Kong, W. Huang, Y. Tsao, D. G. Mackanic, K. Wang, X. Wang, W. Huang, S. Choudhury, Y. Zheng, C. V. Amanchukwu, S. T. Hung, Y. Ma, E. G. Lomeli, J. Qin, Y. Cui and Z. Bao, *Nature Energy*, 2020, **5**, 526-533.

14. C. Niu, D. Liu, J. A. Lochala, C. S. Anderson, X. Cao, M. E. Gross, W. Xu, J.-G. Zhang, M. S. Whittingham, J. Xiao and J. Liu, *Nature Energy*, 2021, **6**, 723-732.

15. J. Qian, B. D. Adams, J. Zheng, W. Xu, W. A. Henderson, J. Wang, M. E. Bowden, S. Xu, J. Hu and J.-G. Zhang, *Advanced Functional Materials*, 2016, **26**, 7094-7102.

16. J. Xiao, *Science*, 2019, **366**, 426-427.

17. R. Zhang, X.-B. Cheng, C.-Z. Zhao, H.-J. Peng, J.-L. Shi, J.-Q. Huang, J. Wang, F. Wei and Q. Zhang, *Advanced Materials*, 2016, **28**, 2155-2162.

18. G. Li, Z. Liu, Q. Huang, Y. Gao, M. Regula, D. Wang, L.-Q. Chen and D. Wang, *Nature Energy*, 2018, **3**, 1076-1083.

19. H. Ye, S. Xin, Y.-X. Yin, J.-Y. Li, Y.-G. Guo and L.-J. Wan, *Journal of the American Chemical Society*, 2017, **139**, 5916-5922.

20. S. Liu, A. Wang, Q. Li, J. Wu, K. Chiou, J. Huang and J. Luo, *Joule*, 2018, **2**, 184-193.

21. Q. Li, J. Chen, L. Fan, X. Kong and Y. Lu, *Green Energy & Environment*, 2016, **1**, 18-42.

22. A. Wang, S. Kadam, H. Li, S. Shi and Y. Qi, *npj Computational Materials*, 2018, **4**, 15.

23. X. Cao, X. Ren, L. Zou, M. H. Engelhard, W. Huang, H. Wang, B. E. Matthews, H. Lee, C. Niu, B. W. Arey, Y. Cui, C. Wang, J. Xiao, J. Liu, W. Xu and J.-G. Zhang, *Nature Energy*, 2019, **4**, 796-805.

24. J. Wang, W. Huang, A. Pei, Y. Li, F. Shi, X. Yu and Y. Cui, *Nature Energy*, 2019, **4**, 664-670.

25. Y. Li, W. Huang, Y. Li, A. Pei, D. T. Boyle and Y. Cui, *Joule*, 2018, **2**, 2167-2177.

26. A. Mukhopadhyay and K. Jangid Manoj, *Science*, 2018, **359**, 1463-1463.

27. D. Puthusseri, M. Parmananda, P. P. Mukherjee and V. G. Pol, *Journal of The Electrochemical Society*, 2020, **167**, 120513.

28. X. Feng, M. Ouyang, X. Liu, L. Lu, Y. Xia and X. He, Energy Storage Materials, 2018, 10, 246-267.

29. K. Liu, Y. Liu, D. Lin, A. Pei and Y. Cui, Science Advances, 4, eaas9820.

30. A. Mukhopadhyay and K. Jangid Manoj, Science, 2018, 359, 1463-1463.

31. R. Xu, X.-Q. Zhang, X.-B. Cheng, H.-J. Peng, C.-Z. Zhao, C. Yan and J.-Q. Huang, *Advanced Functional Materials*, 2018, **28**, 1705838.

32. G. Zheng, S. W. Lee, Z. Liang, H.-W. Lee, K. Yan, H. Yao, H. Wang, W. Li, S. Chu and Y. Cui, *Nature Nanotechnology*, 2014, **9**, 618-623.

33. H. Wu, D. Zhuo, D. Kong and Y. Cui, *Nature Communications*, 2014, **5**, 5193.

Chapter 2. Directing the uniform deposition of Li

2.1. High-Dielectric Polymer Coating for Uniform Lithium Deposition in Anode-Free Lithium Batteries

(The content of this chapter has been published in *ACS Energy letter*, Reproduced with permission from Tamwattana O. et al. High-Dielectric Polymer Coating for Uniform Lithium Deposition in Anode-Free Lithium Batteries. *ACS Energy Lett.*, 2021, 6, 4416−4425, Copyright 2021, American Chemical Society)

2.1.1. Introduction

The demand for high-performance energy storage devices is increasing with the emergence of new technology such as electric vehicles and drones.[1-3] Lithium metal has long been considered the ideal anode material due to its high theoretical capacity and low redox potential (−3.04 V *vs*. the standard hydrogen electrode) [4, 5] toward the high-energy lithium batteries. The anode-free lithium rechargeable battery is of the recent intense interest, as it can offer even higher energy density while containing no specific anode materials in its system. The anode-free battery utilizes the lithium supplied from the cathode, which deposits on the current collector at the anode side[6-9], thus its successful adoption heavily relies on the

stable lithium metal deposition/stripping. Unfortunately, despite the extensive research efforts, the reliable lithium metal anode operation has been still challenging due to issues such as dendritic lithium growth and the formation of inactive lithium during repeated cycling, which are yet to be resolved[10-12]. Its 'hostless' electrode nature causes uncontrollable morphology/volume changes of lithium metal and the accompanying side reactions involving the formation of thick solid electrolyte interphase (SEI) layer upon cycles. The uneven electrode surface typically induces nonuniform electric field building up near the protuberances[13, 14]. Subsequently, lithium grows preferentially on the protuberances, which further exacerbate a locally developed high electric field, triggering the formation of lithium dendrites. Similar phenomena are observed during the stripping processes, where the non-uniform reaction front often engenders the inactive lithium remaining at the electrode[15]. They are accompanied with the low coulombic efficiency and the risk of the short-circuit current flow[16, 17].

Various attempts have been previously made to address these issues such as by exploring new electrolyte compositions to govern the growth of lithium metal or modifying the solid electrolyte interphase (SEI), which led to the improvement to some extent[18-21]. The modifications of the SEI layers were usually conducted by adding various additives in the electrolyte, such as lithium nitrate ($LiNO_3$)[22, 23], halogenated lithium salt (LiX)[24, 25], or gas-phase dopants[15] to form a robust SEI on lithium metal. Alternatively, an artificial SEI layer was pre-coated on the surface of lithium metal anodes, including polymers[26-29], ceramic nanoparticles[30-32], and carbon-based materials[21, 33]. In particular, various polymer-based layers were investigated due to the chemical inertness, mechanical properties and a scalable/low-cost process, such as nano-porous poly(dimethylsiloxane) films[34], a

polymer network with single conducting ion[35] and soft self-healing polymers [36, 37], which could serve as a protective SEI layer for lithium metal anodes. Moreover, Lopez *et al*. [26] reported that the morphology of the lithium is strongly influenced by the chemistry of the coating layers, identifying their dielectric constant as one of the key descriptors of the lithium deposit size. It implied that the artificial SEI should not only provide a physical barrier with high mechanical strength but also effectively govern the chemical/electrical interaction of lithium ions for the uniform lithium transport. In the similar vein, the use of high-dielectric nanoparticles has been also demonstrated to be effective in regulating the lithium transport at the interface between the electrode and electrolyte.[32, 38] It was supposed that the uniform dispersion of the high-dielectric nanoparticles on the electrode could homogenize the electric field near the surface of the lithium metal, thus aiding in regulating the lithium-ion flux. This dielectric modification was found to be viable in improving the charge-transfer kinetics and lowering the interfacial resistance, suggesting that the use of the high-dielectric nanoparticles can be generally applied to regulating the lithium-ion transport.

Inspired by these previous works, herein we attempt to design a polymer-based artificial SEI layer, taking advantage of its good mechanical property and scalable process, through tailoring dielectric properties of the layer by embedding high-dielectric nanoparticles. Subsequently, its efficacy is validated in the anode-free battery system with respect to the lithium deposition/stripping behavior. PVDF-based polymer was chosen as the base coating material due to its facile process of coating in conventional electrode fabrication and its decent dielectric property. We demonstrate that the combined dielectric nanoparticle/polymer modification results in the synergistic effect in regulating the lithium plating behavior. It is shown that

the presence of dielectric nanoparticles dispersed in the polymer not only enhances the dielectric properties in sum, but also induces the spontaneous formation of the high-dielectric ®-PVDF phases, strengthening the dielectric effect of the medium. From the comparative investigations with other PVDF-based polymer layers, we present that the anode-free system with the LiF@PVDF displays one of the best cycling stabilities under practical conditions, whose underlying mechanisms are elucidated with respect to lithium deposition/stripping behaviors. The effect of the dielectric medium on the performance enhancement is further verified by the computational simulation under the various electric field environments.

2.1.2. Experiment section

2.1.2.1. Synthesis and characterization of α-phase, β-phase and LiF@PVDF

PVDF coated on Cu was prepared using PVDF powder (Sigma-Aldrich average Mw 534,000 by GPC). LiF powder (Sigma-Aldrich) as received were ball milled at 760 rpm for 12 hr. LiF nanoparticles mixed in N,N-dinethylacetamide (DMAc, 99%, Sigma-Aldrich) at 60 °C with magnetic stirring overnight. LiF powder was synthesized using a planetary ball mill (Fritsch, Pulverisette 5). The PVDF solution was coated on Cu foil using a doctor blade coater. Solvent was removed by evaporation on a hotplate at 65 °C for 90 min, resulting in crystallization of PVDF in a predominately ®phase. The systhesis of PVDF with a predominant αphase was done by fast drying samples in an oven at 120 ℃℃ for 15 min. Lithium fluoride powder (<100 μm, 99.98%) was purchased from Sigma-Aldrich. Polyvinylidene

fluoride binder for the positive electrodes was purchased from Sigma-Aldrich. Characterization tools. The surface morphologies of the lithium metal and electrodes were measured using field-emission scanning electron microscopy (SU-70, Hitachi). The binding nature of SEI layer on Cu foils were analyzed by using X-ray photoelectron spectroscopy (XPS) (Thermo VG Scientific, Sigma Probe, U.K.) after 10 cycles in Li/Cu cells. The crystalline phases of PVDF were confirmed using Fourier transformed infrared spectroscopy (FTIR). FTIR spectra were recorded on a Perkin Elmer Spectrum Two FTIR spectrometer. The dielectric properties were test using a Keysight E4990A Impedance Analyzer, operating at 20 Hz to 10 MHz. The charge-tranfer resistence of the interface was determined over the frequency range of 1.0 Ghz to 1.0 Hz (VSP-300, Bio-Logic Science Instruments, France).

To determine the ratio between the α and β-phases in the samples, the highest characteristic peaks of the two phases were used, and the equation below was employed[39, 40]

$$F(\beta) = \frac{A_\beta}{(K_\beta/K_\alpha)A_\alpha + A_\beta} F(\beta) = \frac{A_\beta}{(K_\beta/K_\alpha)A_\alpha + A_\beta} \quad (1)$$

where $F(\beta)\,F(\beta)$ represents the β-phase content. $A_\alpha\,A_\alpha$ and $A_\beta\,A_\beta$ are the absorbance at 764 and 840 cm^{-1}, respectively. $K_\alpha K_\alpha$ and $K_\beta K_\beta$ are the absorption coefficients at their respective wave numbers, which had values of 6.1×10^4 and 7.7×10^4 $cm^2\,mol^{-1}$, respectively. The results of FT-IR showed that the αphase peak almost disappeared in the LiF@PVDF sample. The analysis peak area has shown in Figure 2.1.2.1.

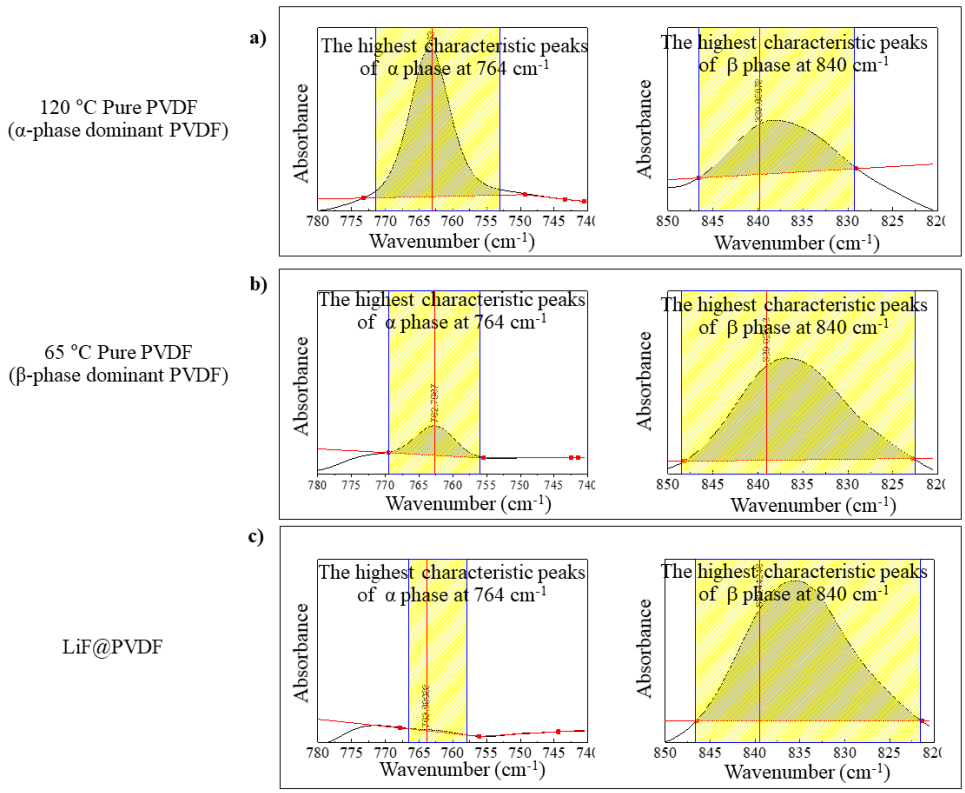

Figure 2.1.2.1: The FT-IR analysis peak area at 764 and 840 cm^{-1} of (a) α-PVDF. (b) ®-PVDF and (c) LiF@PVDF samples

2.1.2.2. Electrochemical characterization

Electrochemical characterizations were performed in CR2032-type coin cells using a potentio-galvanostat (WonA Tech, WBCS 3000, Korea). In the electrochemical characterizations, a two-electrode configuration was adopted in a 2032-type coin cell employing Cu foil as a working electrode and Li metal as a counter electrode. A 300 µm thick Li foil and battery grade electrolyte, 3 wt% lithium nitrate ($LiNO_3$), 1M (lithium bis(trifluoromethanesulfonyl)imide) (LiTFSi) in 1,3dioxolane (DOL)/dimethyl ether (DME) mixture, (volume 1:1), were used

with a Celgard 2400 separator for cell assembly. Applied current density and areal capacity are noted as legends in individual figures for Li/Cu half-cell test and cut-off of 1 V was applied for dissolution process of Li/Cu half cells. For anode-free full cell, $LiFePO_4$ cathode was prepared by casting slurry mixed with a weight ratio of 85:10:5 for active materials, binder and super P carbon. $LiFePO_4$ cathodes have averabe mass loading of 5 mg/cm^2. The same electrolyte was used for anode-free full cell tests. Charge and discharge of anode-free full cells were carried out at 0.5C and 1C-rate, respectively, between 2.5 and 3.8 V at room temperature.

2.1.2.3. COMSOL Simulation.

The simulation was calculated using a numerical COMSOL electrodeposition model with a tertiary Nernst−Planck interface. The model was designed to consist of Li metal, electrolyte, and Cu current collector. The overpotential for Li deposition is set to 0.1 and 0.3 V. The initial Li-ion concentration in electrolyte is set to 1 M.

2.1.3. Results and discussion

2.1.3.1. Morphology, dielectric constant and mechanical properties of α-phase, β-phase and LiF@PVDF

PVDF exhibits a relatively high dielectric constant compared with other fluoropolymers[41, 42] and is highly stable in lithium-ion batteries. It is generally a semi-crystalline polymer with a complex structure that includes three representative crystalline forms, α, β and γ-phases. The structure of the β-phase possesses fluorine and hydrogen atoms located on the opposite sides of the polymer

backbone, giving it a high polarity. On the other hand, the α and β-phases have them in an antiparallel dipole structure and are non-polar; thus, the β-phase PVDF typically displays stronger dielectric properties.[43-46] It has been known that the fraction of each polymorphic phase in the PVDF can be influenced by various processing parameters, such as material concentration, type of casting solvent, and poling temperature [44, 47, 39, 45, 48-50] or additional field applied such as external pressure, mechanical stretching, and electric bias [51-54]. In our investigations, we prepared three types of artificial SEI layers based on PVDF phases with varying dielectric constants, *e.g.*, α-phase PVDF, β-phase PVDF and the PVDF blended with LiF nanoparticles. The α-PVDF and β-PVDF samples were prepared by coating a PVDF casting solution on a Cu foil and controlling their crystallization temperatures at 120 ºC and at 65 ºC, respectively[39, 45, 55, 56]. The blend PVDF sample (LiF@PVDF) was synthesized by controlling its drying temperature at 65 ºC and mixing it with LiF nanoparticles in a 30:70 LiF:PVDF weight ratio. Figure 2.1.3.1a schematically illustrates the polymer structures of each PVDF samples, where it was supposed that the addition of the LiF nanoparticles would generate the dielectric interaction with the PVDF phase, enhancing the yield of the β-phase during the PVDF film formation, as will be further discussed later.

The prepared α-PVDF, β-PVDF and LiF@PVDF films were characterized with respect to their crystalline structure using Fourier transform infrared (FTIR) spectroscopy, as presented in Figure 2.1.3.1b. All the samples displayed the common vibration peaks of characteristic PVDF structures at 871, 1176, 1220, and 1401 cm^{-1} [57, 58] (denoted with 0) as shown in Figure 2.1.3.1b and Figure 2.1.3.2. In addition, the typical vibration modes of the α-type structure at 976, 796, 764, 615 and 530 cm^{1} [59-61] (denoted with *) were primarily observed in the α-PVDF sample,

whereas those of the β-type structure at 840, 510 and 483 cm^{-1} [62-65] (denoted with ■) were clearly displayed in the β-PVDF and LiF@PVDF samples. It was noteworthy that both α-PVDF and β-PVDF samples exhibited the mixed nature of the α- and β-phases to some extent containing noticeable amounts of impurity phases, in consistent with the previous reports[58, 62, 66, 67]. The estimation of the α and β-phase fractions in each sample revealed 34 and 91% of the phase purity for the α-PVDF and the β-PVDF samples, respectively see Table 2.1.3.1[39] On the contrary, nearly no trace of the α-phase was detected in the LiF@PVDF sample, indicating the effect of the high-dielectric LiF nanoparticle dispersion during the PVDF film formation. While the synthesis of high-dielectric ®-phase usually requires the extra process for the purity control[43-46], the results indicate that simple addition of high-dielectric nanoparticles could be effective in regulating the PVDF phase. We also found that mass ratio of 30% LiF is sufficient to induce β phase of PVDF in LiF@PVDF composite as shown in Figure 2.1.3.3 In Figure 2.1.3.4a, the XRD patterns of the LiF@PVDF film is provided, confirming the presence of the crystalline LiF nanoparticles. Figure 2.1.3.1c presents the dielectric properties of the α-PVDF, β-PVDF and LiF@PVDF samples measured in the frequency range of 10^2 to 10^5 Hz. It clearly demonstrates that the β-PVDF exhibits higher dielectric constant than α-PVDF in agreement with the previous reports[68-70], and more importantly, the LiF@PVDF film displays the highest value well over 20 at 1000Hz. Considering that the dielectric constants of PVDF are usually in the range between 4 and 20 at 1000 Hz according to the literatures[70-72], it infers that the high dielectric property of the LiF@PVDF film is likely to be aided not only by the β-phase itself but also by the presence of the LiF nanoparticles. (More details on the measurements regarding the dielectric properties can be found in Figure 2.1.3.4b-

d.)

In order to evaluate the mechanical property as the artificial SEI layer, we measured the stress–strain curves of each PVDF films in Figure 2.1.3.1d. It reveals that tensile strengths of the α-PVDF, β-PVDF and LiF@PVDF films are approximately ~13, 2.5 and 8 MPa, respectively. Young's moduli, as calculated from the slope of the linear region of the curves, were found to be ~470, 160 and 290 MPa, respectively, which are consistent with values reported in the literature for PVDF films[73]. The considerably higher tensile strength and Young's modulus in α-PVDF are attributable to a denser microstructure and lesser porosity, as will be discussed later with the SEM studies. Elongation values at breakage are in the range of 4-7% for all the samples, and did not change noticeably with the addition of LiF nanoparticles in the PVDF matrix. It indicates that the ceramic nanoparticles are homogeneously dispersed in the PVDF matrix creating few or no extra defects. Toughness was measured to be 38.36 J/m^3 for α-PVDF, 11.78 J/m^3 for β-PVDF and 39.07 J/m^3 for LiF@PVDF, as estimated from the area under the stress–strain curve of each sample, signifying considerable increases in both stiffness and toughness due to the presence of LiF nanoparticles. The top-view SEM images in Figure 2.1.3.1df illustrate the surface morphology of the coating layers. α-PVDF manifests a dense and uniform layer, whereas relatively porous structures were found in the cases of the β-PVDF and LiF@PVDF layers. It agrees with the previous observations that the βphase PVDF generally exhibits a morphology with a greater density of porousity[40, 45, 68]. The average thickness of the three samples was approximately 2.5 μm, as shown in Figure 2.1.3.5a-c. Despite the different surface morphologies, the backsides of α-PVDF, β-PVDF and LiF@PVDF appear to be non-porous and replicate the texture of the underlying Cu foil (Figure 2.1.3.5df).

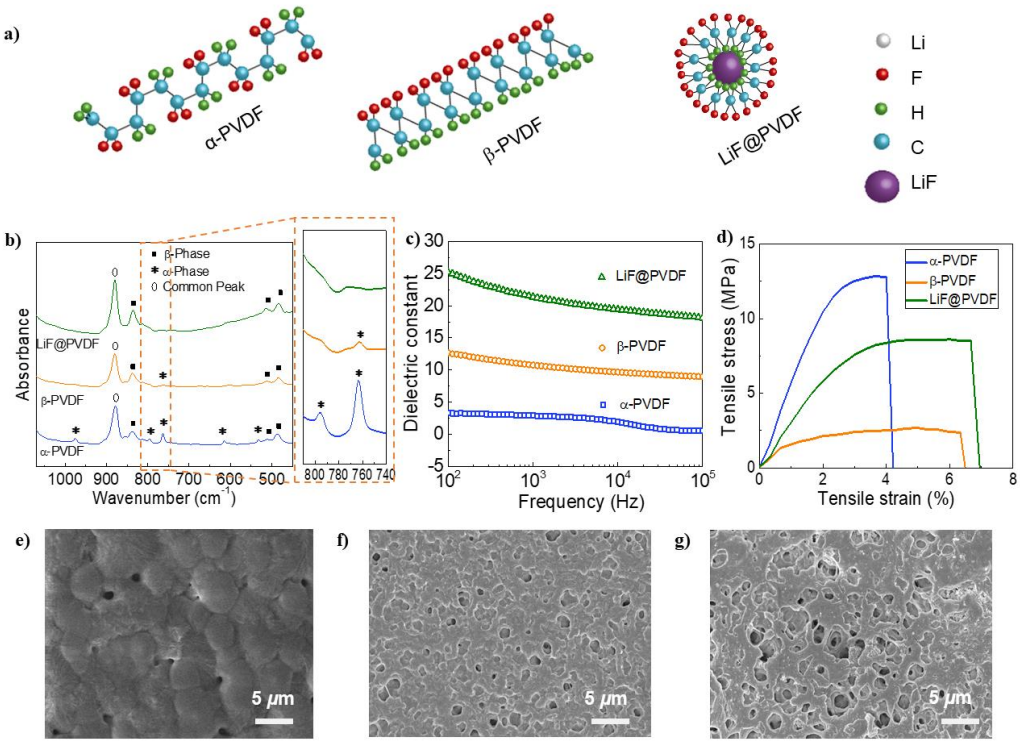

Figure 2.1.3.1. Schematic illustration of molecular level of PVDF and comparison of the properties of α-PVDF, β-PVDF and LiF@PVDF coated on Cu foil showing (a) Molecular structure of α-PVDF, ®-PVDF and LiF@PVDF. (b) FT-IR spectra, (c) the dielectric constants, and (d) stress-strain curves. (e-g) Top view SEM images of pristine (e) α-PVDF, (f) ®-PVDF, and (g) LiF@PVDF samples.

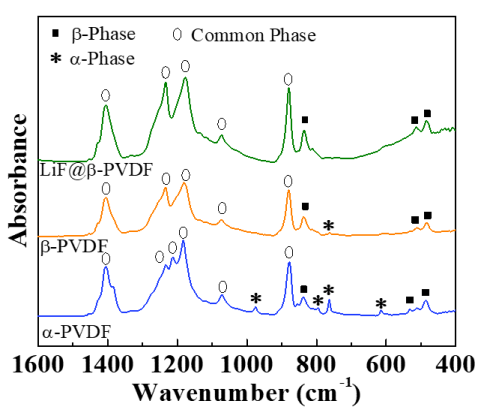

Figure 2.1.3.2. FT-IR spectra of α-PVDF, β-PVDF and LiF@PVDF

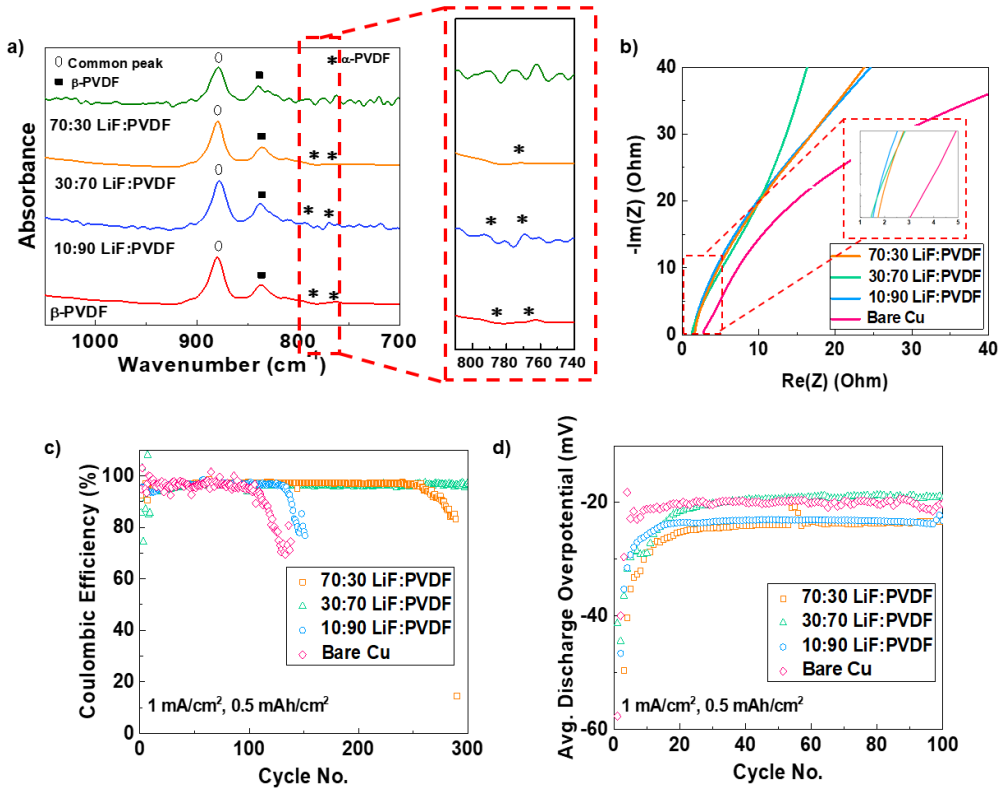

Figure 2.1.3.3 (a) FT-IR spectra of LiF@PVDF samples with different mass ratio. (b) EIS plots, (c) cycle stability, and (d) average discharge overpotential of Li/LiF@PVDF@Cu cells with different mass ratio. Though a trace amount of α-PVDF is observed for the β-PVDF and 10% LiF containing PVDF composite, we could eliminate the remaining α phase of PVDF with the ratio of LiF over 30%.These results clearly infer that sufficient amount of LiF is needed to induce high-dielectric film and thus improve electrochemical stability of Li deposition; however, the excess amount of LiF is also not desirable for cell performances showing high resistance and overpotential, leading to poor cycle stability.

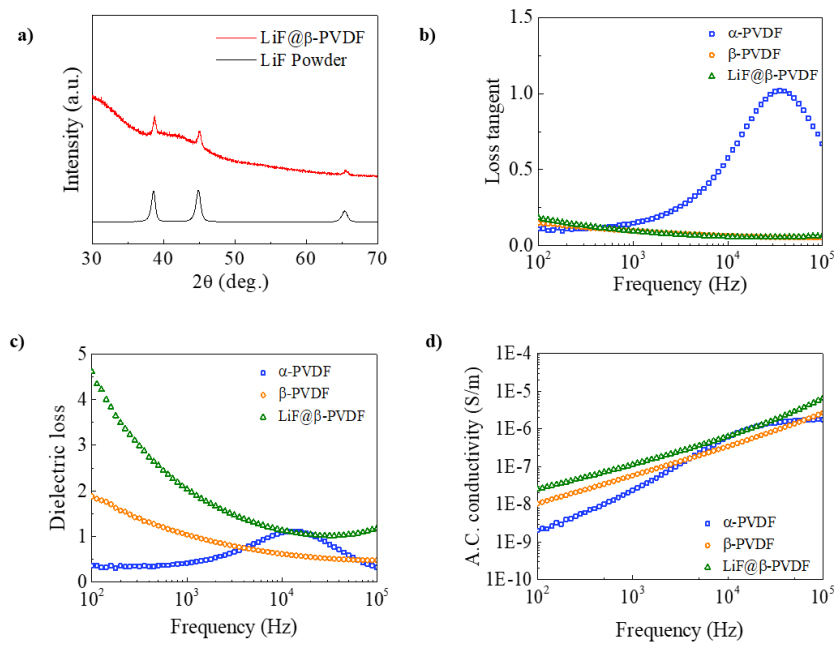

Figure 2.1.3.4. (a) XRD patterns of LiF nanoparticles in a LiF@PVDF layer. (b) loss tangent, (c) dielectric loss and (d) A.C. conductivity of α-PVDF, β-PVDF and LiF@PVDF

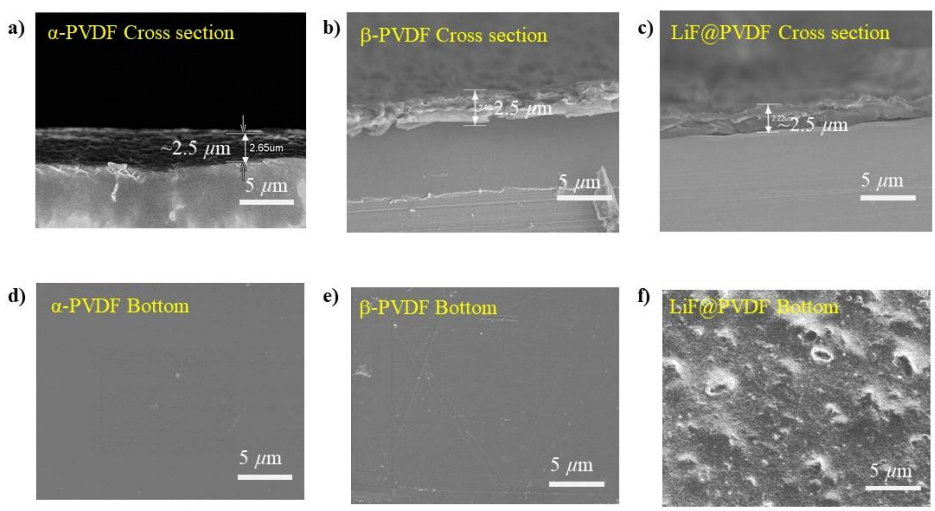

Figure 2.1.3.5. Properties of PVDF coatings: (a-c) cross-sectional SEM images of

as-prepared αPVDF, β-PVDF and LiF@PVDF , respectively, coated on Cu foil, and, (d-f) bottom view SEM image of the α-PVDF, ®-PVDF and LiF@PVDF coating taken off of the Cu substrate, respectively.

Table 2.1.3.1: The fraction of β-phase in each sample

120 °C Pure PVDF (α-phase dominant PVDF)	65 °C Pure PVDF (β-phase dominant PVDF)	LiF@PVDF
0.3485325657	0.912620867	0.997657989

2.1.3.2. Evolution of Li deposition on bare Cu, α-phase, β-phase and LiF@PVDF

Employing the current collectors coated with these films, we examined the lithium plating behaviors by probing the microstructures of lithium deposits using several loading capacities. Figure 2.1.3.6 depicts the top view images of the electrodes with the loading capacities increasing from 0.5, 1, 5 to 10 mAh cm^{-2} at a constant current density of 1 mA cm^{-2}. As a reference, the lithium deposition was also monitored on the bare Cu current collector (left column, Figure 2.1.3.6a-d). The images in the figure clearly reveal that the deposition of the lithium is strongly influenced by the presence of the PVDF surface layer on the current collector. In the case of the bare Cu case, micron-sized lithium deposits begin to appear at a loading capacity of 0.5 mAh cm^{-2}. Similar behavior was observed in the α-PVDF coated case at the same low loading capacity (Figure 2.1.3.6e and 2f). The subsequent lithium growth takes place primarily from the pre-existing deposits, which engenders more aggressive filament-like protrusions, as seen in Figure

2.1.3.6c and g. With the further deposition up to 10 mAh cm^{-2}, the filament-like protrusions tend to merge together, making bigger columnar morphology. It is believed that the merge of the protrusions is partly attributable to the mechanical pressure imposed by the separator in the coin-cell. On the other hand, the β-PVDF coated Cu allowed lithium to be relatively uniformly deposited at capacity loadings of 0.5 and 1 mAh cm^{-2}. Figure 2.1.3.6i and j display that the ®-PVDF surface layer is solely observable without the cracking of the film, indicating the absence of the nonuniform micron-sized lithium deposits underneath. When the capacity loading approaches to 5 mAh cm^{-2}, bulges on the surface start to appear, indicating that the non-uniform lump of lithium deposits pushes the film upward in Figure 2.1.3.6k. Eventually, the ®-PVDF layer mechanically fails at the highest areal capacity loading of 10 mAh cm^{-2} (Figure 2.1.3.6l), exposing the lithium deposits similar to the case in Figure 2.1.3.6d and h.

Noteworthy was that the LiF@PVDF film successfully maintains the stable surface at all areal capacity loadings, as shown in Figure 2.1.3.6 m-p. Even at the capacity loading of 10 mAh cm^{-2}, the signature of the bulges was not observable underneath the LiF@PVDF films. Further evidence of the uniform lithium growth under the LiF@PVDF film could be found from the cross-sectional views of electrode after the deposition in Figure 2.1.3.7. It comparatively depicts the microstructures of all samples under various loading capacities, and clearly presents that the lithium growth is much more uniform with the LiF@PVDF film than other cases. The absence of the protrusion during the lithium growth also ensures the mechanical stability of the LiF@PVDF film, which would be beneficial for the long-term cycles. Moreover, the thickness of the lithium deposition was found to be remarkably close to the expected thickness estimated from the charge

applied to the electrode, confirming that the dense lithium film was obtained underneath the LiF@PVDF, as shown in Figure 2.1.3.8 and S7.

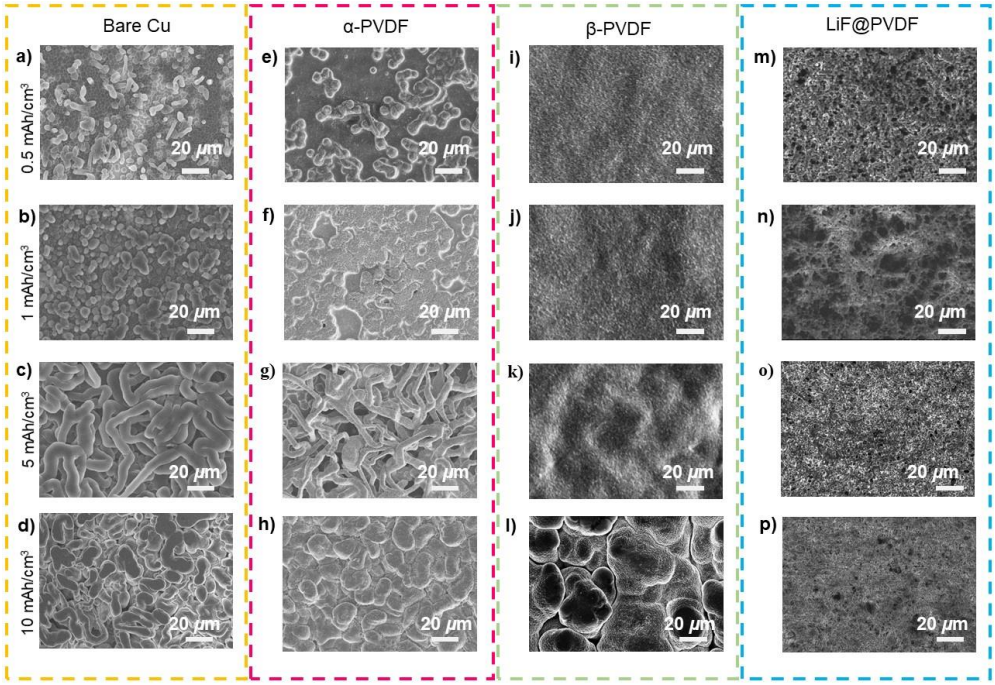

Figure 2.1.3.6. Comparison of morphologies of deposited Li on bare Cu for α-PVDF, β-PVDF and LiF@PVDF at various capacity loadings. (a-d) SEM images after depositing Li on bare Cu foils, (e-h) α-PVDF, (i-l) ®-PVDF, and (mp) LiF@PVDF at 0.5, 1, 5 and 10 mAh cm^{-2}, respectively. The typical filamentary growth of lithium metal on the current collector begin to appear from the loading capacity of 5 mAh cm^{-2} for the reference bare Cu and the α-PVDF samples.

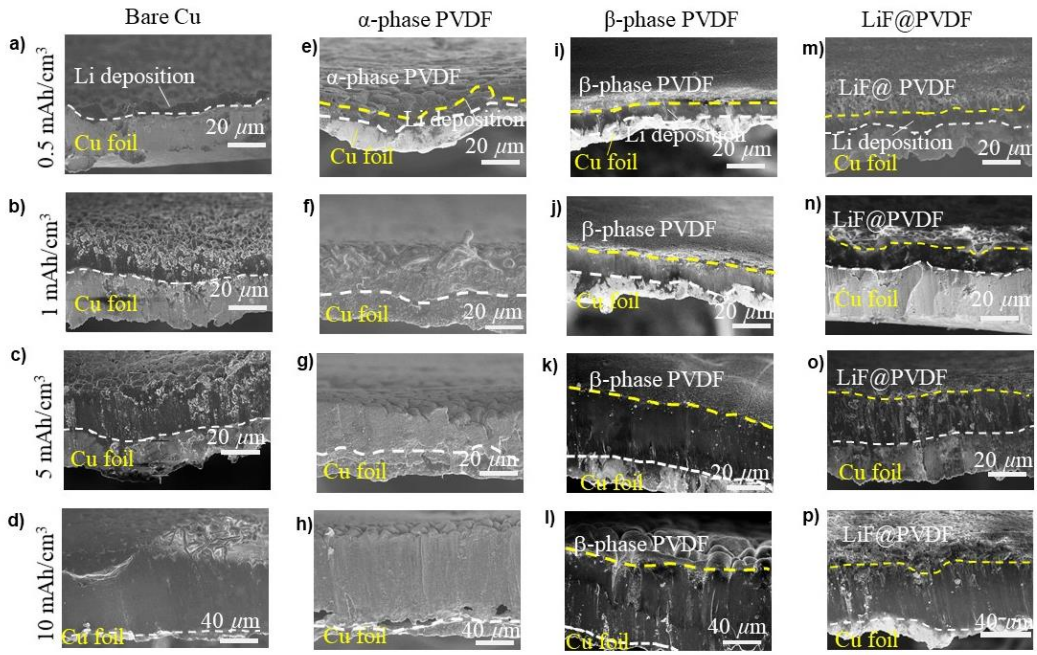

Figure 2.1.3.7. Cross-sectional SEM images of Li-deposited on bare Cu foil, α-PVDF, β-PVDF and LiF@PVDF. (a-d) cross-sectional SEM images after depositing Li on bare Cu foils at 0.5, 1, 5 and 10 mAh/cm^2, respectively. (e-h) SEM images after depositing Li on α-PVDF at 0.5, 1, 5 and 10 mAh/cm^2, respectively. (i-l) SEM images after depositing Li on ®-PVDF at 0.5, 1, 5 and 10 mAh/cm^2, respectively. (m-p) SEM images after depositing Li on LiF@PVDF at 0.5, 1, 5 and 10 mAh/cm^2, respectively.

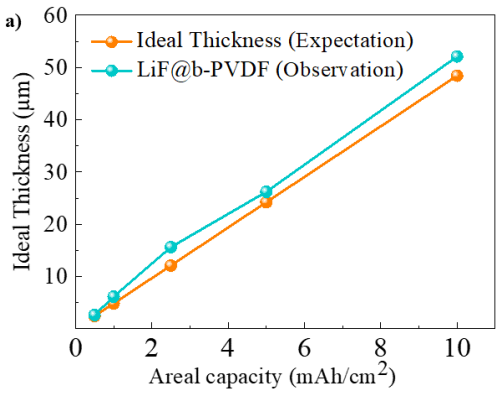

b)

Areal capacity (mAh/cm²)	Ideal Thickness (μm)	Average Thickness of Li Deposition (μm)
		LiF@β-PVDF
0.5	2.4212	2.621
1	4.8424	6.15
2.5	12.106	15.62
5	24.2120	26.2
10	48.4240	52.1

Figure 2.1.3.8. (a) is the comparison ideal thickness between Li metal thickness and LiF@PVDF (b) Table of ideal thickness.

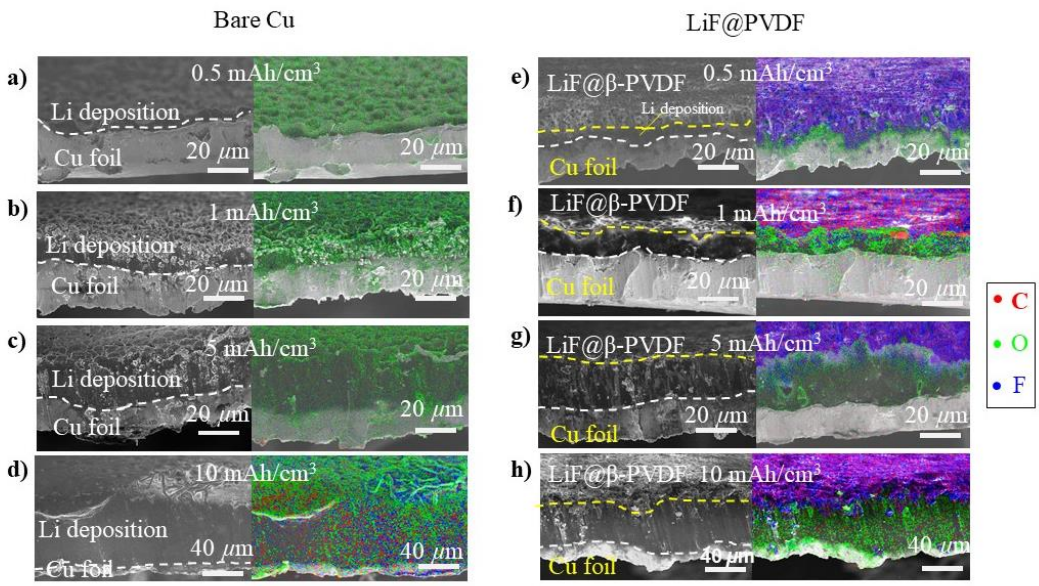

Figure 2.1.3.9. Cross-sectional SEM images and EDS spectra of Li-deposited on bare Cu foil and LiF@PVDF. (a-d) Cross-sectional SEM images and EDS spectra after depositing Li on bare Cu foils at 0.5, 1, 5 and 10 mAh/cm², respectively. (e-h) EDS spectra after depositing Li on LiF@PVDF at 0.5, 1, 5 and 10 mAh/cm², respectively.

Table 2.1.3.2: Coulombic efficiency (CE) of LiF@PVDF cells compared with other polymeric coating modifications

Current density	Areal capacity	Cycle number	CE(%)	References
1	0.5	200	98	β-PVDF coated, 2017[27]
		300	96.57	This work
2	0.5	60	96.5	β-PVDF coated, 2017[27]
		150	92.9	Polyimide coating, 2016[28]
		200	96.66	This work
5	0.5	60	92.5	β-PVDF, 2017[27]
		100	90.2	This work
1	1	120	97	Silly putty, 2017[37]
		100	98.2	PDMS coating, 2017[34]
		100	97.4	Cu_3N + SBR, 2017[29]
		100	97	LiF+ PVDF-HFP, 2018[25]
		200	98.4	This work

2.1.3.3. Electrochemical performance and reversible cycle ability

The electrochemical performances of the anode-free lithium half-cells employing current collectors coated with αPVDF, β-PVDF and LiF@PVDF were comparatively evaluated under various conditions in Figure 2.1.3.10 and Figure 2.1.3.11. Figure 2.1.3.10a-c illustrates the Coulombic efficiency (CE) of each cell, *i.e.*, the capacity ratio of lithium deposition *vs.* stripping, as a function of cycle number, when the electrochemical half-cells were cycled at 1, 2 and 5 mA cm^{-2} with a fixed deposition capacity of 0.5 mAh cm^{-2}. It was found that the electrode of bare current collector and the one with α-PVDF exhibited unstable values of CEs, which led to a sudden short circuit within 100 cycles at 1 and 2 mA cm^{-2}. Even

shorter cycle stability and inferior CE values were recorded when operated at a higher current density of 5 mA cm^{-2}, indicating the uncontrolled lithium growth at high current densities. On the other hand, markedly stable CE values could be achieved for electrodes with β-PVDF and LiF@PVDF along with the robust cycling stability. In particular, LiF@PVDF sample could exhibit the highest cycle stability over 300 cycles at all the current densities with stable CE values (96.6%, 96.7%, 90.2% after 300 cycles at 1 mA cm^{-2}, after 200 cycles at 2 mA cm^{-2}, and after 100 cycles at 5 mA cm^{-2}, respectively). We would like to note that the cycle stability of the LiF@PVDF-based cell outperforms those of most previous reports of polymeric coating remedies on lithium metals as tableted in Table 2.1.3.2 with respect to the cycle number and CE values. Enhanced cycle stabilities of LiF@PVDF compared to bare Cu were also confirmed with the utilization of higher areal capacity of 1 and 3 mAh/cm^2, as shown in Figure 2.1.3.11. The enhanced performance of LiF@PVDF cell is attributable to the stable and uniform lithium deposition behaviors in Figure 2.1.3.6. Dendritic lithium filaments and dead lithium were evidently observed on the bare Cu current collector after 50 cycles, which contrasts to the cycled LiF@PVDF coated electrode with relatively smooth surface, as probed by SEM images in Figure 2.1.3.12. Figure 2.1.3.10d-f display the electrochemical profiles of the cell employing LiF@PVDF layer at each current density, revealing that relatively low voltage hysteresis could be also maintained. With the uniform lithium deposition possible on the current collector with the LiF@PVDF layer, the densely plated lithium would support a good connection within the electrode during cycles, which would promote the facile charge transfer, lowering the overpotential in the dissolution process. In the light of practical applicability, furthermore, we also examined the electrochemical

properties in anode-free full cell configuration coupling with $LiFePO_4$ cathodes in Figure 2.1.3.13, which again demonstrates performance enhancements of Cu foil with LiF@PVDF coating even with the harsh condition of limited lithium sources in anode-free full batteries. The impact of polymer coating thickness was also discussed in Figure 2.1.3.14 where thickening of the coating layers leads to the increase in resistance and thus the optimization of the thickness of dielectric film is needed considering other properties.

We further examined the morphological reversibility of lithium at high areal capacities of 5 and 10 mAh cm^{-2} on the LiF@PVDF-coated current collector by collecting series of cross-sectional SEM images during electrochemical cycling as marked in Figure 2.1.3.15. It is observed that the lithium metal begins to be plated underneath the conformally coated LiF@PVDF layer (Figure 2.1.3.15a-i) and becomes approximately 16 μm thick after the discharge of 2.5 mAh cm^{-2}, which is close to the expected lithium film thickness considering the capacity (Figure 2.1.3.15a-ii). Up to the discharge capacity of 5 mAh cm^{-2}, no significant change in the morphology was observable except for the simple growth of the lithium film thickness ~ 28 μm in Figure 2.1.3.15a-iii, exhibiting evidently uniform lithium deposition. The reversible stripping of lithium metal was also witnessed in Figure 2.1.3.15a-iv, maintaining the intact interface with the LiF@PVDF film during the charging process. At the end of the charge in Figure 2.1.3.15a-v, all the lithium metal was fully stripped out, recovering the pristine state of the current collector with a great reversibility. Reversibility of the plating and stripping of lithium was further investigated utilizing a larger capacity of 10 mAh cm^{-2} in Figure 2.1.3.15b. The dense lithium metal layer was plated with a thickness of 26 μm after a capacity of 5 mAh cm^{-2} (Figure 2.1.3.15b-ii), consistent with the result

in Figure 2.1.3.15a-iii. The subsequent discharge of 10 mAh cm^{-2} yielded a 53 μm-thick and uniform lithium deposition layer underneath LiF@PVDF film on the current collector (Figure 2.1.3.15b-iii). Importantly, the 53 μm-thick lithium plate could be reversibly dissolved as shown in Figure 2.1.3.15b-iv and completely stripped out, recovering the pristine current collector coated with LiF@PVDF layer in Figure 2.1.3.15b-v. These observations manifestly prove that the high-dielectric LiF@PVDF artificial SEI films are capable of inducing homogeneous and reversible plating/stripping of lithium metal up to a significantly large utilization level.

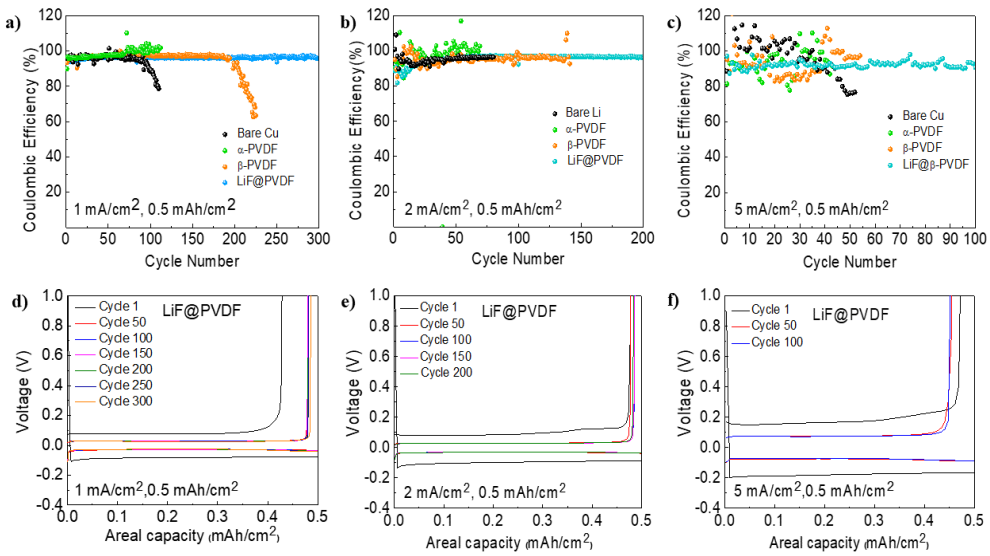

Figure 2.1.3.10. Electrochemical characterizations showing (a-c) CE at current densities of 1, 2 and 5 mA cm^{-2}, respectively, (d-f) voltage versus areal capacity profiles of LiF@PVDF at selected cycles for Li deposition/stripping at current densities of 1, 2 and 5 mA cm^{-2}, respectively.

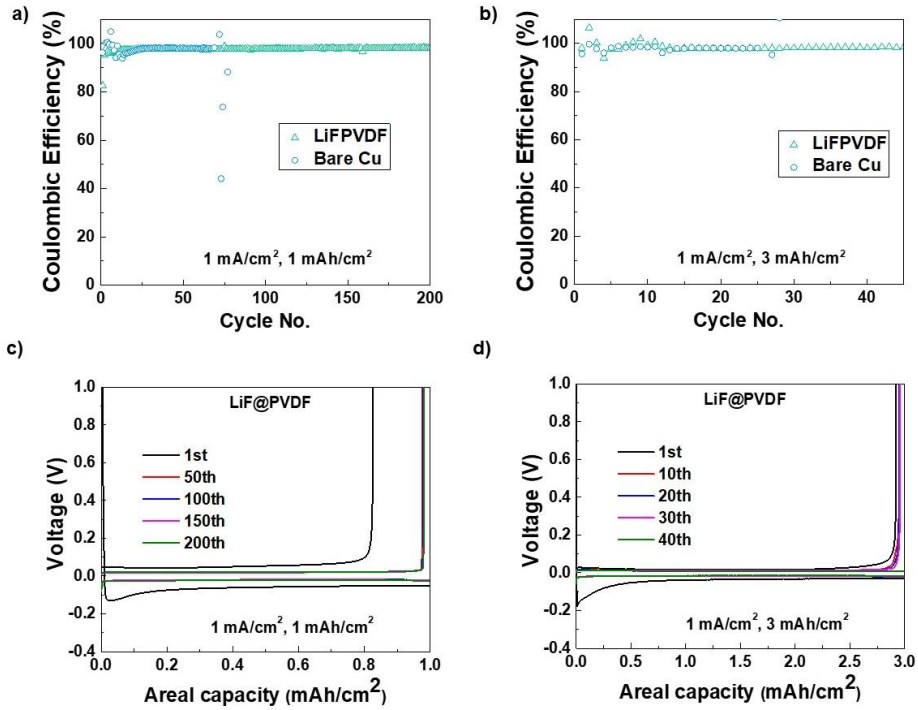

Figure 2.1.3.11. Electrochemical properties of Li/Cu cells with bare Cu and LiF@PVDF coated Cu. Coulombic efficiency with cycling under the utilization of areal capacity of (a) 1 mAh/cm^2 and (b) 3 mAh/cm^2. Voltage profile of Li/LiF@PVDF@Cu cells at selected cycles the utilization of areal capacity of (c) 1 mAh/cm^2 and (d) 3 mAh/cm^2. A current density of 1 mA/cm^2 was applied for all tested cells.

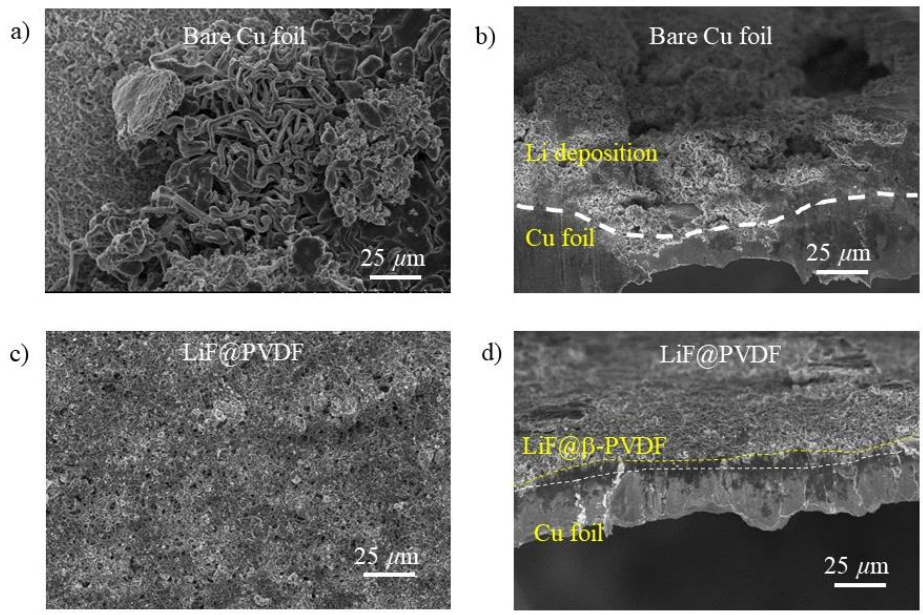

Figure 2.1.3.12. SEM images of lithium morphology of cells after 50 cycles. (a-b) the morphology after 50 cycles of bare Cu, top and cross-sectional views, respectively. (c-d) the morphology after 50 cycles of a LiF@PVDF coating, top and cross sectional views, respectively.

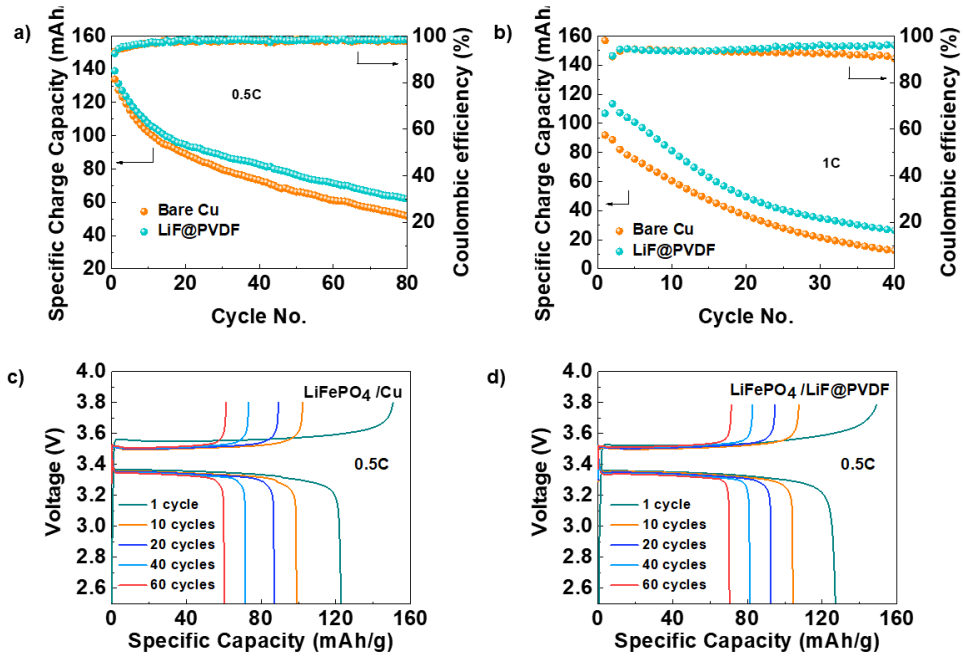

Figure 2.1.3.13. Cycle properties of $LiFePO_4$/Cu and $LiFePO_4$/LiF@PVDF cells (a) at a 0.5C rate and (b) 1C rate. Voltage profile of (c) $LiFePO_4$/Cu cells and (d) $LiFePO_4$/LiF@PVDF cells at selected cycles.

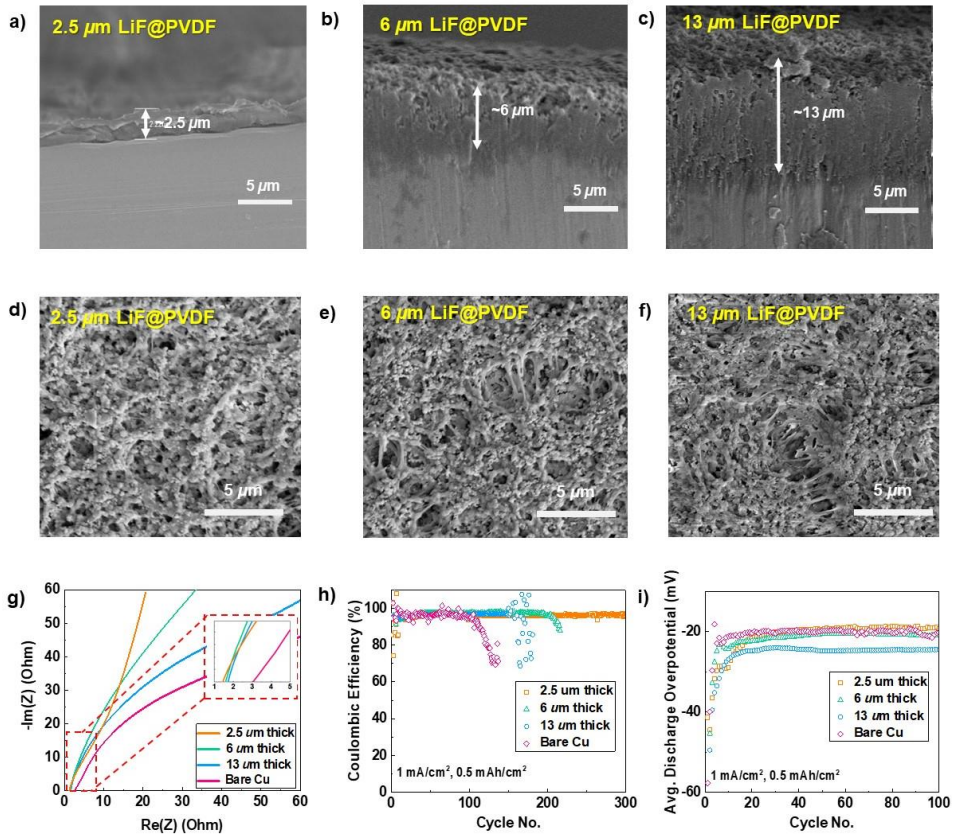

Figure 2.1.3.14. Morphological characterization of the cross-section of pristine LiF@PVDF coated at the thicknesses of (a) 2.5, (b) 6 and (c) 13 μm. Morphological characterization of the cross-section of pristine LiF@PVDF coated at the thicknesses of (d) 2.5, (e) 6 and (f) 13 μm. (g) Impedance spectra of LiF@PVDF samples with different coating thickness. (h) Cycling stability and (i) average discharge overpotential of Li/LiF@PVDF@Cu cells during cycling. The increase in the thickness of polymer films results in the increase in charge transfer impedances, which infers that the thickness of polymer films can affect the transport property of the film. The beneficial effect of dielectric layer could be compensated by the increase in impedance if the polymer coating becomes too thick so that the transport property through the coating is weakened.

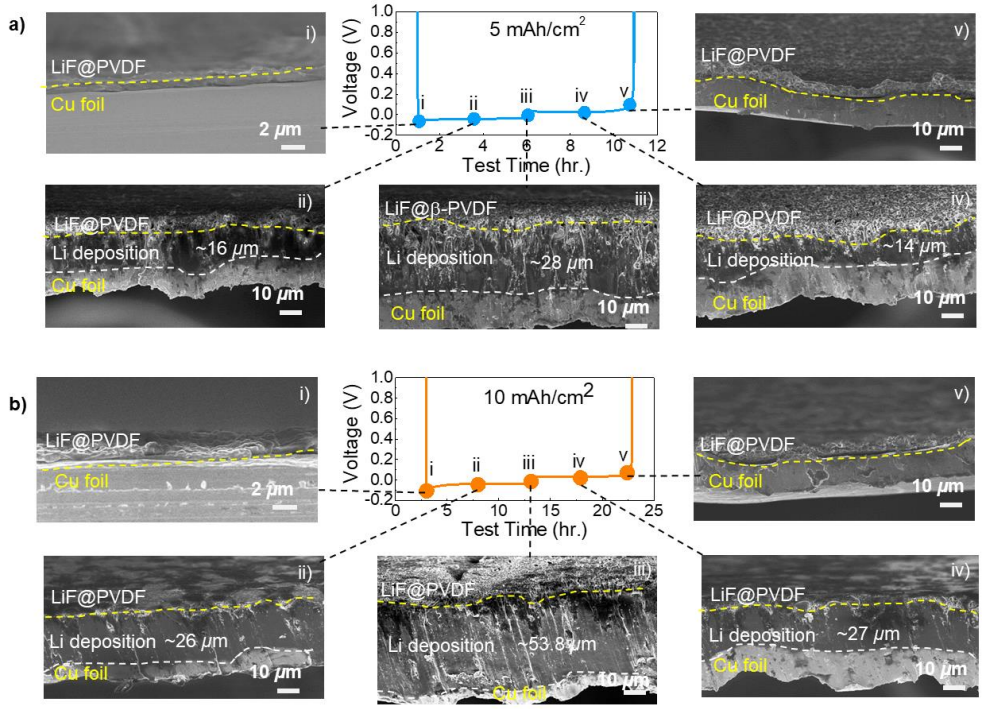

Figure 2.1.3.15. Li plating and stripping behaviors at practical capacity loadings of LiF@PVDF. (a) voltage profile at a capacity loading of 5 mAh cm^{-2}, (iv) cross-sectional SEM images showing reversibility of Li plating and stripping according to stages i-v of the voltage profile in (a), (b) voltage profile at a capacity loading of 10 mAh cm^{-2}, (i-v) cross-sectional SEM images showing reversibility of Li plating and stripping according to stages i-v of the voltage profile in (b).

2.1.3.4. Elucidate the function of high dielectric constant of SEI by experiment and theory detail

To better understand the distinct lithium deposition behavior, we investigated the effect of the dielectric medium on the charge-transfer resistance and the overpotential. Figure 2.1.3.16a shows that the electrode with LiF@PVDF presents the lowest overpotential during the lithium plating process than those of the ®-PVDF and α-PVDF samples, indicating a smaller charge-transfer resistance at the interface (Figure 2.1.3.16b). Moreover, the initial dip of the potential, which is known to arise due to the energy barrier for lithium nucleation, was found to be the smallest for the electrode coated with LiF@PVDF, indicating the correlation between the coating medium and the lithium deposition kinetics. [35, 74] It is supposed that the high dielectric medium homogenizes the electric field at the interface and mitigates the locally high current density region, thus reducing the overall interface overpotential. Note that the surface analysis results reveal that the SEI component on Cu foils after cycling is almost identical regardless of PVDF coatings as shown in Figure 2.1.3.17, which rules out any potential impact of altered SEI structure by side reactions of PVDF with Li metals[75]. The consequence of the low interface overpotential could be examined on the distinct lithium deposition behavior by the simple comparative simulation in Figure 2.1.3.16c. The numerical simulation was carried out considering the interface medium during the lithium deposition (Figure 2.1.3.18), when different effective overpotentials were applied with 0.1 and 0.3V. It is shown that the lithium conformally grows on the initial triangular shape of the current collector at 0.1 V overpotential, while the lithium deposits in irregular

shapes plating the current collector nonuniformly at 0.3V overpotential. Moreover, the concentration gradient (M) on the surface (represented in color) indicates that lithium ions are rapidly depleted near the surface in the case of a 0.3 V overpotential, which increases the interface resistance further.

Based on the understanding, we propose the underlying mechanism of lithium deposition behaviors upon the high-dielectric artificial coating as schematically illustrated in Figure 2.1.3.16 d and e. During the plating process, the high electric field is locally developed on the protuberances for the uncoated current collector (Figure 2.1.3.16d). Accordingly, the lithium depositions mainly take place at protuberances, where the further growth exacerbates the localized electric field, leading to roughening of the surface. Moreover, the continuous consumption of lithium ions near the surface at the protuberances accelerates the depletion of local concentration of lithium ions, finally reaching the sand time at which lithium begins to grow in a dendritic feature.[76-78] On the contrary, a high-dielectric coating offers a dipole layer arranged alongside the surface of current collectors, which can guide the lithium ions into more homogenous pathway (Figure 2.1.3.16e). The uniform lithium-ion flux through high-dielectric media enables smooth deposition of lithium metals as evidenced in our previous SEM images. Even with the potential formation of protuberances, the high-dielectric layer alleviates the irregularity of local ion concentrations by spreading out lithium ion pathways through the conformal charge-polarized layer. The redistribution of lithium-ion flux within high-dielectric matrix equalizes the lithium-ion concentrations at the surface of lithium metals. The effective regulation of lithium-ion flux leads to the lower overpotential and prolonged sand time on the coated current collectors, resulting in the uniform lithium deposition up to remarkably high utilization level. Modulating

lithium-ion flux in an undeviating manner also promotes homogeneous electrochemical lithium dissolutions, achieving high Coulombic efficiency and reversibility of anode-free type lithium cells.

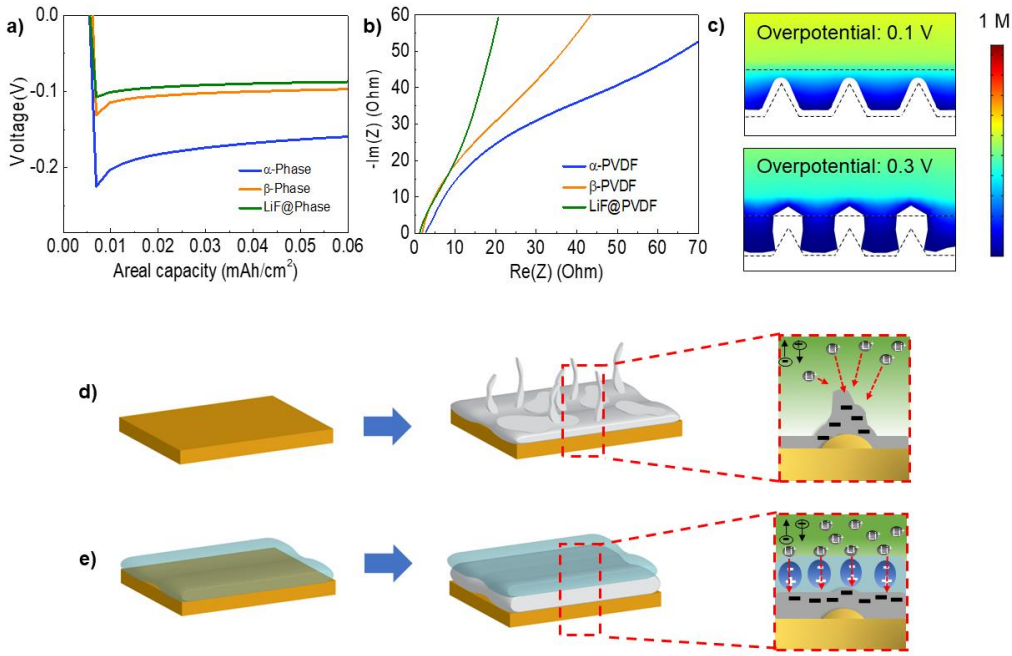

Figure 2.1.3.16. (a) Voltage profiles of Li deposition showing the interface overpotentials of bare Cu, α-PVDF, ®-PVDF and LiF@PVDF samples, (b) Impedance spectra showing charge-transfer resistances of α-PVDF, ®-PVDF and LiF@PVDF samples, (c) The numerical system simulate the lithium concentration gradients on the artificial SEI polymer coated on bare Cu with the overpotentials of 0.1 V and 0.3 V. Schematic illustration of theoretical elucidation of the growth mechanisms of Li-ion depletion and mitigating the surface concentration difference during concentration polarization, (d) without high dielectric constant artificial SEI, and (e) with high dielectric constant artificial SEI.

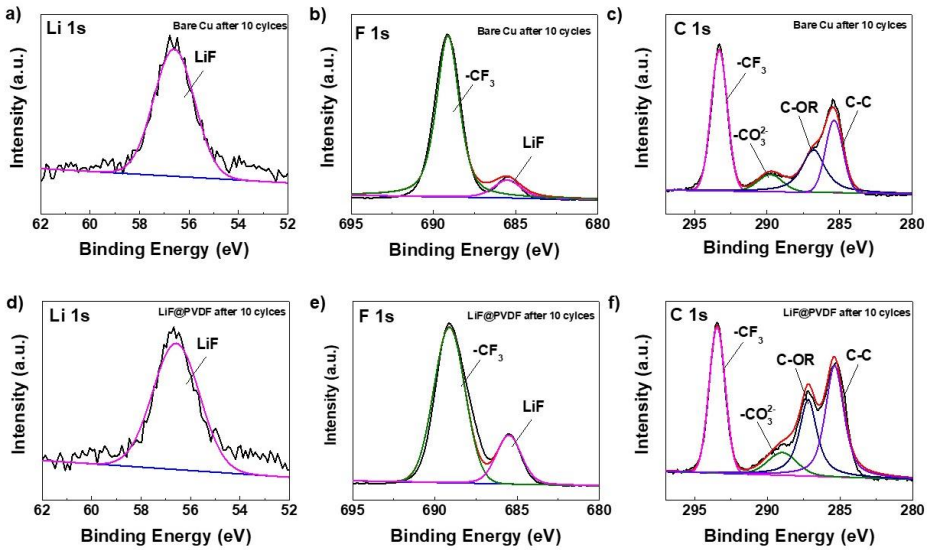

Figure 2.1.3.17. (a) Li 1s, (b) F 1s and (c) C 1s XPS spectra for bare Cu after 10 cycles in Li/Cu cells. (d) Li 1s, (e) F 1s and (f) C 1s XPS spectra of Cu foils with peeling off LiF@PVDF film after 10 cycles in Li/LiF@PVDF@Cu cells. The binding energy was calibrated with C 1s at 284.8 eV.

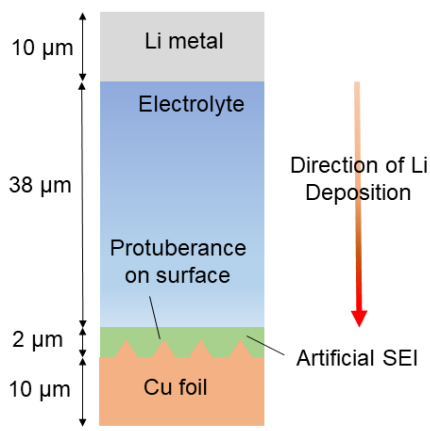

Figure 2.1.3.18. Schematic diagram of the numerical model system used to simulate the lithium concentration gradients on the artificial SEI polymer coated on bare Cu

2.1.4. Conclusion

We have addressed the efficacy of dielectric coating media on the lithium deposition behaviors in anode-free lithium batteries and suggested a new high-dielectric polymeric artificial interphase by successfully regulating the phase of PVDF with the incorporation of high-dielectric nanoparticles. Compared with the lower dielectric and lower surface-area α-PVDF interphase, highly polarized ®-PVDF and LiF@PVDF coated current collectors were demonstrated to promote remarkably homogeneous lithium depositions underneath the polymer layers. By engendering uniform depositions with LiF@PVDF layer, the effective electrochemical stripping of lithium deposits was also confirmed for a significantly large utilization level up to 10 mAh cm^{-2}, which exhibits one of the best cycle stabilities for polymeric coating approaches. Computational simulations supported the idea that high-dielectric media could decrease the overpotential between electrodes, lower the lithium-ion concentration differences at the surface of lithium deposits, and thus resulting in a reduction of the local current density and the uniform deposition of lithium metals. This study is expected to enrich the fundamental understandings on the lithium deposition behaviors particularly regarding the dielectric function of artificial layers and spur further efforts on the developments of high-dielectric, mechanically/chemically robust, and easily processable polymeric interphase for highly stable lithium metal plating/stripping in anode-free type lithium cells.

2.1.5. Reference

1. J. M. Tarascon and M. Armand, *Nature*, 2001, **414**, 359-367.

2. S. Chu and A. Majumdar, *Nature*, 2012, **488**, 294-303.

3. M. S. Whittingham, *Proceedings of the IEEE*, 2012, **100**, 1518-1534.

4. X.-B. Cheng, R. Zhang, C.-Z. Zhao and Q. Zhang, *Chemical Reviews*, 2017, **117**, 10403-10473.

5. P. Albertus, S. Babinec, S. Litzelman and A. Newman, *Nature Energy*, 2018, **3**, 16-21.

6. A. J. Louli, A. Eldesoky, R. Weber, M. Genovese, M. Coon, J. deGooyer, Z. Deng, R. T. White, J. Lee, T. Rodgers, R. Petibon, S. Hy, S. J. H. Cheng and J. R. Dahn, *Nature Energy*, 2020, **5**, 693-702.

7. J. Qian, B. D. Adams, J. Zheng, W. Xu, W. A. Henderson, J. Wang, M. E. Bowden, S. Xu, J. Hu and J.-G. Zhang, *Advanced Functional Materials*, 2016, **26**, 7094-7102.

8. S. Nanda, A. Gupta and A. Manthiram, *Advanced Energy Materials*, 2021, **11**, 2000804.

9. A. J. Louli, M. Coon, M. Genovese, J. deGooyer, A. Eldesoky and J. R. Dahn, *Journal of the Electrochemical Society*, 2021, **168**, 020515.

10. W. Xu, J. Wang, F. Ding, X. Chen, E. Nasybulin, Y. Zhang and J.-G. Zhang, *Energy & Environmental Science*, 2014, **7**, 513-537.

11. S. F. Liu, X. L. Wang, D. Xie, X. H. Xia, C. D. Gu, J. B. Wu and J. P. Tu,

Journal of Alloys and Compounds, 2018, **730**, 135-149.

12. X. Sun, X. Zhang, Q. Ma, X. Guan, W. Wang and J. Luo, *Angewandte Chemie International Edition*, 2020, **59**, 6665-6674.

13. P. Bai, J. Li, F. R. Brushett and M. Z. Bazant, *Energy & Environmental Science*, 2016, **9**, 3221-3229.

14. C. Brissot, M. Rosso, J. N. Chazalviel and S. Lascaud, *Journal of Power Sources*, 1999, **81-82**, 925-929.

15. S. Moon, H. Park, G. Yoon, M. H. Lee, K.-Y. Park and K. Kang, *Chemistry of Materials*, 2017, **29**, 9182-9191.

16. A. W. Golubkov, R. Planteu, P. Krohn, B. Rasch, B. Brunnsteiner, A. Thaler and V. Hacker, *RSC Advances*, 2018, **8**, 40172-40186.

17. Y. Zhu, J. Xie, A. Pei, B. Liu, Y. Wu, D. Lin, J. Li, H. Wang, H. Chen, J. Xu, A. Yang, C.-L. Wu, H. Wang, W. Chen and Y. Cui, *Nature Communications*, 2019, **10**, 2067.

18. N.-W. Li, Y.-X. Yin, C.-P. Yang and Y.-G. Guo, *Advanced Materials*, 2016, **28**, 1853-1858.

19. Y. Li, Y. Sun, A. Pei, K. Chen, A. Vailionis, Y. Li, G. Zheng, J. Sun and Y. Cui, *ACS Central Science*, 2018, **4**, 97-104.

20. K. Yan, H.-W. Lee, T. Gao, G. Zheng, H. Yao, H. Wang, Z. Lu, Y. Zhou, Z. Liang, Z. Liu, S. Chu and Y. Cui, *Nano Letters*, 2014, **14**, 6016-6022.

21. G. Zheng, S. W. Lee, Z. Liang, H.-W. Lee, K. Yan, H. Yao, H. Wang, W. Li, S. Chu and Y. Cui, *Nature Nanotechnology*, 2014, **9**, 618-623.

22. Y. Liu, D. Lin, Y. Li, G. Chen, A. Pei, O. Nix, Y. Li and Y. Cui, *Nature Communications*, 2018, **9**, 3656.

23. W. Li, H. Yao, K. Yan, G. Zheng, Z. Liang, Y.-M. Chiang and Y. Cui, *Nature Communications*, 2015, **6**, 7436.

24. R. Pathak, K. Chen, A. Gurung, K. M. Reza, B. Bahrami, J. Pokharel, A. Baniya, W. He, F. Wu, Y. Zhou, K. Xu and Q. Qiao, *Nature Communications*, 2020, **11**, 93.

25. R. Xu, X.-Q. Zhang, X.-B. Cheng, H.-J. Peng, C.-Z. Zhao, C. Yan and J.-Q. Huang, *Advanced Functional Materials*, 2018, **28**, 1705838.

26. J. Lopez, A. Pei, J. Y. Oh, G.-J. N. Wang, Y. Cui and Z. Bao, *Journal of the American Chemical Society*, 2018, **140**, 11735-11744.

27. J. Luo, C.-C. Fang and N.-L. Wu, *Advanced Energy Materials*, 2018, **8**, 1701482.

28. W. Liu, D. Lin, A. Pei and Y. Cui, *Journal of the American Chemical Society*, 2016, **138**, 15443-15450.

29. Y. Liu, D. Lin, P. Y. Yuen, K. Liu, J. Xie, R. H. Dauskardt and Y. Cui, *Advanced Materials*, 2017, **29**, 1605531.

30. E. Kazyak, K. N. Wood and N. P. Dasgupta, *Chemistry of Materials*, 2015, **27**, 6457-6462.

31. A. C. Kozen, C.-F. Lin, A. J. Pearse, M. A. Schroeder, X. Han, L. Hu, S.-B. Lee, G. W. Rubloff and M. Noked, *ACS Nano*, 2015, **9**, 5884-5892.

32. Y. Lu, Z. Tu and L. A. Archer, *Nature Materials*, 2014, **13**, 961-969.

33. K. Yan, Z. Lu, H.-W. Lee, F. Xiong, P.-C. Hsu, Y. Li, J. Zhao, S. Chu and Y. Cui, *Nature Energy*, 2016, **1**, 16010.

34. B. Zhu, Y. Jin, X. Hu, Q. Zheng, S. Zhang, Q. Wang and J. Zhu, *Advanced Materials*, 2017, **29**, 1603755.

35. J. Wang, W. Huang, A. Pei, Y. Li, F. Shi, X. Yu and Y. Cui, *Nature Energy*, 2019, **4**, 664-670.

36. G. Zheng, C. Wang, A. Pei, J. Lopez, F. Shi, Z. Chen, A. D. Sendek, H.-W. Lee, Z. Lu, H. Schneider, M. M. Safont-Sempere, S. Chu, Z. Bao and Y. Cui, *ACS Energy Letters*, 2016, **1**, 1247-1255.

37. K. Liu, A. Pei, H. R. Lee, B. Kong, N. Liu, D. Lin, Y. Liu, C. Liu, P.-c. Hsu, Z. Bao and Y. Cui, *Journal of the American Chemical Society*, 2017, **139**, 4815-4820.

38. C. Yada, A. Ohmori, K. Ide, H. Yamasaki, T. Kato, T. Saito, F. Sagane and Y. Iriyama, *Advanced Energy Materials*, 2014, **4**, 1301416.

39. J. R. Gregorio and M. Cestari, *Journal of Polymer Science Part B: Polymer Physics*, 1994, **32**, 859-870.

40. P. Martins, A. C. Lopes and S. Lanceros-Mendez, *Prog. Polym. Sci.*, 2014, **39**, 683-706.

41. J. Nunes-Pereira, C. M. Costa and S. Lanceros-Méndez, *Journal of Power Sources*, 2015, **281**, 378-398.

42. H. Teng, *Applied Sciences*, 2012, **2**, 496-512.

43. T. Hattori, M. Kanaoka and H. Ohigashi, *Journal of Applied Physics*, 1996, **79**,

2016-2022.

44. C. Ribeiro, V. Sencadas, J. L. G. Ribelles and S. Lanceros-Méndez, *Soft Materials*, 2010, **8**, 274-287.

45. V. Sencadas, R. Gregorio Filho and S. Lanceros-Mendez, *Journal of Non-Crystalline Solids*, 2006, **352**, 2226-2229.

46. H.-J. Ye, W.-Z. Shao and L. Zhen, *Journal of Applied Polymer Science*, 2013, **129**, 2940-2949.

47. J. Zheng, A. He, J. Li and C. C. Han, *Macromolecular Rapid Communications*, 2007, **28**, 2159-2162.

48. A. Salimi and A. A. Yousefi, *Journal of Polymer Science Part B: Polymer Physics*, 2004, **42**, 3487-3495.

49. J. S. Andrew and D. R. Clarke, *Langmuir*, 2008, **24**, 670-672.

50. A. M. Gaur and D. S. Rana, *Journal of Inorganic and Organometallic Polymers and Materials*, 2019, **29**, 1637-1644.

51. N. J. English and C. J. Waldron, *Physical Chemistry Chemical Physics*, 2015, **17**, 12407-12440.

52. V. Ballenegger and J. P. Hansen, *Molecular Physics*, 2004, **102**, 599-609.

53. L. Lee, S.-J. Park and S. Kim, *Solid State Ionics*, 2013, **234**, 19-24.

54. H. Kim, F. Torres, D. Villagran, C. Stewart, Y. Lin and T.-L. B. Tseng, *Macromolecular Materials and Engineering*, 2017, **302**, 1700229.

55. A. Ferreira, P. Costa, H. Carvalho, J. M. Nobrega, V. Sencadas and S. Lanceros-

Mendez, *Journal of Polymer Research*, 2011, **18**, 1653-1658.

56. V. Sencadas, R. Gregorio and S. Lanceros-Méndez, *Journal of Macromolecular Science, Part B*, 2009, **48**, 514-525.

57. M. A. Bachmann, W. L. Gordon, J. L. Koenig and J. B. Lando, *Journal of Applied Physics*, 1979, **50**, 6106-6112.

58. X. Cai, T. Lei, D. Sun and L. Lin, *RSC Advances*, 2017, **7**, 15382-15389.

59. T. Boccaccio, A. Bottino, G. Capannelli and P. Piaggio, *Journal of Membrane Science*, 2002, **210**, 315-329.

60. R. H. Upadhyay and R. R. Deshmukh, *Journal of Electrostatics*, 2013, **71**, 945-950.

61. F. Mokhtari, M. Shamshirsaz and M. Latifi, *Polymer Engineering & Science*, 2016, **56**, 61-70.

62. R. Gregorio Jr, *Journal of Applied Polymer Science*, 2006, **100**, 3272-3279.

63. J. Gomes, J. Serrado Nunes, V. Sencadas and S. Lanceros-Mendez, *Smart Materials and Structures*, 2010, **19**, 065010.

64. A. Salimi and A. A. Yousefi, *Polymer Testing*, 2003, **22**, 699-704.

65. Y. Peng and P. Wu, *Polymer*, 2004, **45**, 5295-5299.

66. S. Barrau, A. Ferri, A. Da Costa, J. Defebvin, S. Leroy, R. Desfeux and J.-M. Lefebvre, *ACS Applied Materials & Interfaces*, 2018, **10**, 13092-13099.

67. T. Nishiyama, T. Sumihara, Y. Sasaki, E. Sato, M. Yamato and H. Horibe, *Polymer Journal*, 2016, **48**, 1035-1038.

68. R. Gregorio and E. M. Ueno, *Journal of Materials Science*, 1999, **34**, 4489-4500.

69. P. Thomas, S. Satapathy, K. Dwarakanath and K. J. a. p. a. Varma, 2013.

70. A. N. Arshad, M. H. M. Wahid, M. Rusop, W. H. A. Majid, R. H. Y. Subban and M. D. Rozana, *Journal of Nanomaterials*, 2019, **2019**, 5961563.

71. S. Song, Z. Zheng, Y. Bi, X. Lv and S. Sun, *Journal of Materials Science*, 2019, **54**, 3832-3846.

72. J. Li, Q. Meng, W. Li and Z. Zhang, *Journal of Applied Polymer Science*, 2011, **122**, 1659-1668.

73. Y. Pei and X. C. Zeng, *Journal of Applied Physics*, 2011, **109**, 093514.

74. A. Pei, G. Zheng, F. Shi, Y. Li and Y. Cui, *Nano Letters*, 2017, **17**, 1132-1139.

75. L. H. Abrha, Y. Nikodimos, H. H. Weldeyohannes, T. T. Hagos, D.-Y. Wang, C.-J. Huang, S.-K. Jiang, S.-H. Wu, W.-N. Su, M.-C. Tsai and B. J. Hwang, *ACS Applied Energy Materials*, 2021, **4**, 3240-3248.

76. C. Léger, J. Elezgaray and F. Argoul, *Physical Review E*, 1998, **58**, 7700-7709.

77. H. J. S. Sand, *The London, Edinburgh, and Dublin Philosophical Magazine and Journal of Science*, 1901, **1**, 45-79.

78. A. J. Bard and L. R. Faulkner, *Electrochemical Methods*, 2001, **2**, 580-632.

2.2. Leaching Organic SEI by Electrochemical Dissolution Leads to monolithic inorganic SEI and Enhancing Cycle Stability for Anode Free Battery.

2.2.1. Introduction

The dramatic growth in demand for high-density energy storage required to fulfill the needs of today's electric vehicles and grid storage has resulted in a worldwide effort in conventional rechargeable lithium-ion batteries during the past five years[1]. However, lithium-ion batteries have advanced virtually as far as they are capable of. As a result of its poor energy density and high cost[2-4]. Among the most effective methods is to remove the standard graphite anode. This is because it has the potential to dramatically boost the energy density of batteries while also lowering their cost. Zero lithium excess or anode-free lithium batteries (AFLBs) may provide approximately 60% better volumetric energy densities than Li-ion cells, which offer a range of up to 680 kilometers for electric cars[5-7]. However, the performance of anode-free lithium batteries is largely influenced by Li nucleation and growth. The primary issue arises from the unregulated development of Li on the host-less substrate, which results in the formation of dendrites, dead lithium, and a massive decomposition of electrolytes. Inhomogeneity SEI is recognized to be the primary cause of uncontrolled proliferation of Li. SEI was produced as a result of an electrochemical reduction process at the first Li-plated electrode[8-10]. The decomposition of complex salts and solvents at the collector current surface

influences the nanostructure and mechanical characteristics of SEI, which have a significant effect on Li deposition and dissolution. Inadequate mechanical and ionic conductivity qualities of SEI may result in uneven deposition and dissolution, resulting in needle-like morphology, a large surface area, and, ultimately, electrolyte dry up[11-14]. SEI is a framework composed of inorganic and organic nanocrystals that is used in common Li-ion batteries with graphite anodes[15-18]. SEI's organic framework is characterized by a low molecular weight and a wide variety of molecular chains. The uneven molecular weight distribution of this organic framework is mechanically unstable[19-23], results in non-uniform Li deposition, promotes dendrite formation, and depletes the electrolyte. The majority of these organic frameworks decompose in the presence of a common solvent. On the other hand, owing to the high molecular weight of the inorganic SEI layer, the inorganic structure offers constant stiffness and ion conductivity. A large portion of this layer is formed as a result of the breakdown of salts. The ideal SEI, on the other hand, should have monolithic ionic conductivity as well as being mechanically robust. Even with commercial complicated electrolyte systems, this is a very unusual occurrence. This layer is mainly derived from salt decomposition. However, the ideal SEI should be monolithic ionic conductivity and mechanically stable. This rarely happens in commercial complex electrolyte systems. A number of research projects have been undertaken to produce a novel electrolyte with excellent stability to Li, a stable form of SEI that is consistently durable[24-26], or temperature control for optimizing the stability of the SEI layer to be stable for both mechanical and ionic conductivity[13, 27]. However, we provide here a simple electrochemical polishing approach in which the dissolving voltage cut off is controlled at 2V, allowing for SEI organic polishing while leaving just a

homogeneously inorganic inner layer to be maintained. Cryogenic electron microscopy has proven this polishing of an organic-rich outer layer to leave just an inorganic-rich layer (Cryo-TEM)[28, 29] and depth profile X-ray photoelectron spectroscopy (XPS). The single layer of inorganic-rich layer provides the homogeneous ionic conductivity of SEI layer, leading to uniform deposition and dissolution of Li, less dead Li, less surface area, and improve the cycle stability[14, 20]. The single layer of inorganic-rich material provides the SEI layer with homogenous ionic conductivity, resulting in uniform Li deposition and dissolution, reduced dead Li, and a smaller surface area, all of which increase cycle stability. We hope that this study would be the inspiration for people to pay attention to electrochemical dissolution changing the nanostructure of SEI.

2.2.2. Experiment section

2.2.2.1. Materials and Characterization

Cathode ($LiFePO_4$) was prepared by casting a slurry mixture containing 85wt% active material, 5wt% polyvinylidene fluoride binder (PVDF), and 10wt% Super P conductive carbon in N-methyl-2-pyrrolidone (NMP) onto an aluminum (Al) current collector foil. The electrode was dried for 75ºC for 12 hr. under vacuum and punched into disks with a diameter of 0.9525 cm. Lithium metal foil (300 μm thick, 1.27 cm diameter) and 1 M LiTFSi, 3 wt% $LiNO_3$ in 1,3dioxolane (DOL)/dimethyl ether (DME) mixture, (volume 1:1), were used with a Celgard 2400 separator for Li/Cu and $LiFePO_4$/Cu cell assembly.

All samples were washed with 1,3-dioxolane (DOL) and dried inside the glovebox before characterization. The surface and cross-section morphologies of the lithium

metal and electrodes were measured using field-emission scanning electron microscopy (SU-70, Hitachi). In-situ optical microscopy was used as a homemade designed cell (ECLIPSE LV150N, Nikon, Japan). Cryo-TEM experiments were performed on JEOL-200F (JEOL Ltd) equipped with an UltraScan 1000XP CCP detector (Gatan) and a HAADF detector at 200kV acceleration voltage with cryo-TEM holder (Model 626, Gatan). To prevent air exposure, rinsed Cu TEM grid is carefully mounted onto cryo-TEM holder by being transferred in Teflon-sealed grid box and opening grid box in liquid nitrogen. Electron dose rate is controlled to 2~3$e^-/Å^2$ s at low magnification and 200~300 $e^-/Å^2$ s at high magnification to avoid beam damage during Cryo-TEM imaging. Cryo-STEM EELS line scan was performed using probe size of 1.5nm with 0.5s exposure time.

2.2.2.2. Battery Electrochemistry

All battery electrochemistry was done in an argon-filled glovebox utilizing CR2032-type coin batteries and a potentio-galvanostat (WonA Tech, WBCS 3000, Korea). In the Li/Cu half-cell test, a negative area capacity of 0.5 mAh/cm2 was applied with a current density of 1 mA/cm2, and dissolution was applied until the working voltage reached 1 V for 1 V cutoff and 2 V for 2 V cutoff. Charge and discharge rates for the LiFePO4/Cu anode free cell were 0.2 C-rate, and LiFePO4 had a mass loading of 8.74 mg per cell. Cryo-TEM was performed using a "200-mesh" Cu lacey carbon TEM grid, cycling at 1.267 mA for 30 minutes, and stripping away Li until the working potential reached 1V and 2V. After disassembling the cell in the glovebox, the Cu grid was washed with 1,3-dioxolane (DOL) solvent to remove Li salt and dried before to analysis. For in-situ

OM, we used a Li foil as the counter-electrode and a 100-L electrolyte drop, with the electrodes receiving an alternating current of 40mA/cm2, 0.5mAh/cm2. **Supplementary Figure 2.2.2.1a and S5b** illustrate an in-situ OM setup using a handmade electrochemical cell.

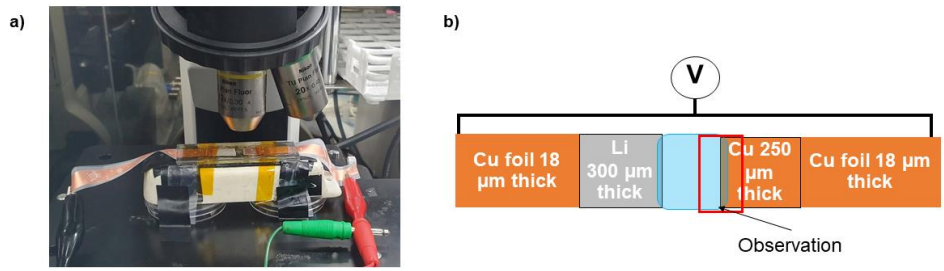

Figure 2.2.2.1. a) Camera image of cell undergoing in-situ optical microscopy deposition/ dissolution with a current density of 40 $mAcm^2$ and 0.5 mAh/cm^2. b) Schematic of cell configuration for in-situ OM transparent cell. These experiments have been tested under Argon atmosphere.

2.2.2.3. COMSOL Simulation.

The simulation was performed using a model with a tertiary Nernst-Planck interface and a numerical COMSOL electrodeposition. The model was composed of a conductor made of Li metal, an electrolyte, and a current collector made of Cu. The outside SEI layer was found to be 70 nm thick, whereas the inner layer is 100 nm thick. On the outer SEI layer, the cracking area was randomly fractured. The Li deposition overpotential is set at 0.4 V. The initial concentration of Li-ion in the electrolyte is fixed at 1 M. Li has a diffusion coefficient of 2.93e-10, 0.586e-10, and 0.293e-10, respectively, in the electrolyte, outer layer, and inner layer.

2.2.3. Results and discussion

2.2.3.1. Electrochemical leaching to remove the organic SEI layer

Basically, our electrochemical approach is based on a strategy of electrochemical stripping at a high voltage of 2 V. We initially saw pictures of Li metal particles generated after the first electrochemical plating using cryogenic electron microscopy (Cryo-TEM). As shown in **Figure 2.2.3.1a**, the low magnification shows the circular morphology of Li metals relevant to the previous study.[9, 10, 13, 30]. As the magnification of the cryo-TEM increases to the nanoscale, The SEI nanostructures could be seen in the **Figure 2.2.3.1d**. **Figure 2.2.3.1d** demonstrates a constant SEI thickness of roughly 30 nm on the Li surface, as seen by the dashed line (both white and yellow color). As can be seen, the borders of the Li particles have a darker contrast than the SEI area shown by the white dotted line. This signifies that there are elements in this clause with a greater atomic number than Li[10, 31]. However, after the dark zone It features a brighter outer layer with a yellow dotted inner layer. As a consequence, we would anticipate that the two layers would combine to create the SEI layer during the first Li plating. To continue our investigation of the SEI layer throughout the dissolution process, we performed Cryo-TEM analysis for the first cycle (deposition and dissolution) for both 1 V and 2 V cut off. As seen in Figure 2.1.3.1b, the low magnification of 1 V striping gives a snapshot of the SEI structure's hollow form. After removing all Li metal from the Cu surface, the SEI hollow structure remained shrunk. The SEI nanostructures were clearly visible in **Figure 2.2.3.1e** after 1V stripping at a high magnification.

The dashed line retains the same double SEI as the initial deposition. However, the outer layer seemed to be thinner than the first and included cracks. In comparison, **Figure 2.2.3.1f** depicts a 2V cutoff at the SEI's nanoscale. The SEI layer in this picture is distinct from the original deposition and the 1V stripping. The 2V stripping seems to completely remove the outer layer. (high contrast) and removed everything except the inner layer (dark contrast). Additionally, the average SEI layer thickness at 2V was 20nm, which is remarkably comparable to the thickness of the initial deposition's dark area. According to previous literature in ether base electrolytes, the double SEI layer is inorganic and organic[32-34]. The inner layer is mostly composed of salts, whereas the outer layer is composed of the solvent decomposing to generate an organic outer layer. As a result, at 1V, the dual layer is still visible. During dissolution, the outer layer cracks and partly dissolves the particles (which are finer than those formed by Li deposition) in the electrolyte. This is consistent with previous research on cracking and organic SEI layers that are soluble. Whereas, 2V electrochemical dissolution allows for the complete removal of all organic layers, leaving just the inorganic layer, which is stiffer and more homogeneous in SEI.

2.2.3.2. Inorganic and organic chemical content in SEI layer

To elucidate the clarity of the double SEI, X-ray photoelectron microscopy (XPS) analysis was performed for depth profiling **Figure 2.2.3.1g-i** shows the SEI layer after first cycle (deposition-dissolution) 1V and 2V. The spectrum of Li 1s was chosen to represent inorganic species. It is often composed of LiF, Li_3N, Li_2O, and $ROCO_2Li$, all of which decompose primarily from electrolyte salts. The Cu foil

current collector stripping Li for the first cycle i**n Figure 2.2.3.1g-i**, at 0 to 30 minute sputter time (0 nm), 1V cut off seems to have a low lithium contain, and have a high content of Carbon. Meanwhile, after 30 minutes of sputter time (10 nm), Lithium contains is increase and Carbon contains is decrease. Corresponding to the Cryo-TEM image result, that the thickness of an outer organic-rich layer is about 10 nm. In contrast, the 2 V cut-off show the constant of intensity both Lithium and Carbon from 0 to 80 minute sputter time(20 nm) as shown **in Figure 2.2.3.1j-l**. In this regard, this result confirms that 2 V cut off remains only a monolithic layer of the inorganic layer. Likewise, we also conduct the cryogenic electron energy loss spectroscopy (EELS) through Cryo-TEM to test the content of Carbon and Lithium at the SEI layer. Although XPS in-depth profiling can provide information on the chemical composition it contains, however to obtain the correct chemical composition in a single SEI layer, EELS is the most powerful chemical element analysis in the nano-level SEI layer. As shown in **Figure 2.2.3.2a-h**, after the first dissolution of Li 1V and 2V , Lithium contain had been analyzed. We selected the thick edge of the circular hollow shape of the SEI region and tested a line scan from the outer edge of the SEI to the inside. The 1V solubility containing lithium and carbon showed opposite lithium and carbon concentrations. The lithium contains show less intensity from the surface, after 10 nm distance, it keeps increasing as shown **in Figure 2.2.3.2 a and 1e.** In contrast, carbon contain shows a high intensity at the outer surface and keeps decreasing after 10 nm. This result is consistent with Cryo-TEM and XPS dept-profile images, which confirm that the organic-rich outer layer is about 10 nm thick. On the other hand, the first striping of 2V shows opposite carbon and lithium signals. Lithium is highly concentrated on the outer surface but the carbon concentrations were similar with the line scan. This

confirms that the monolithic inorganic layer maintains a uniform ionic conductive SEI layer.

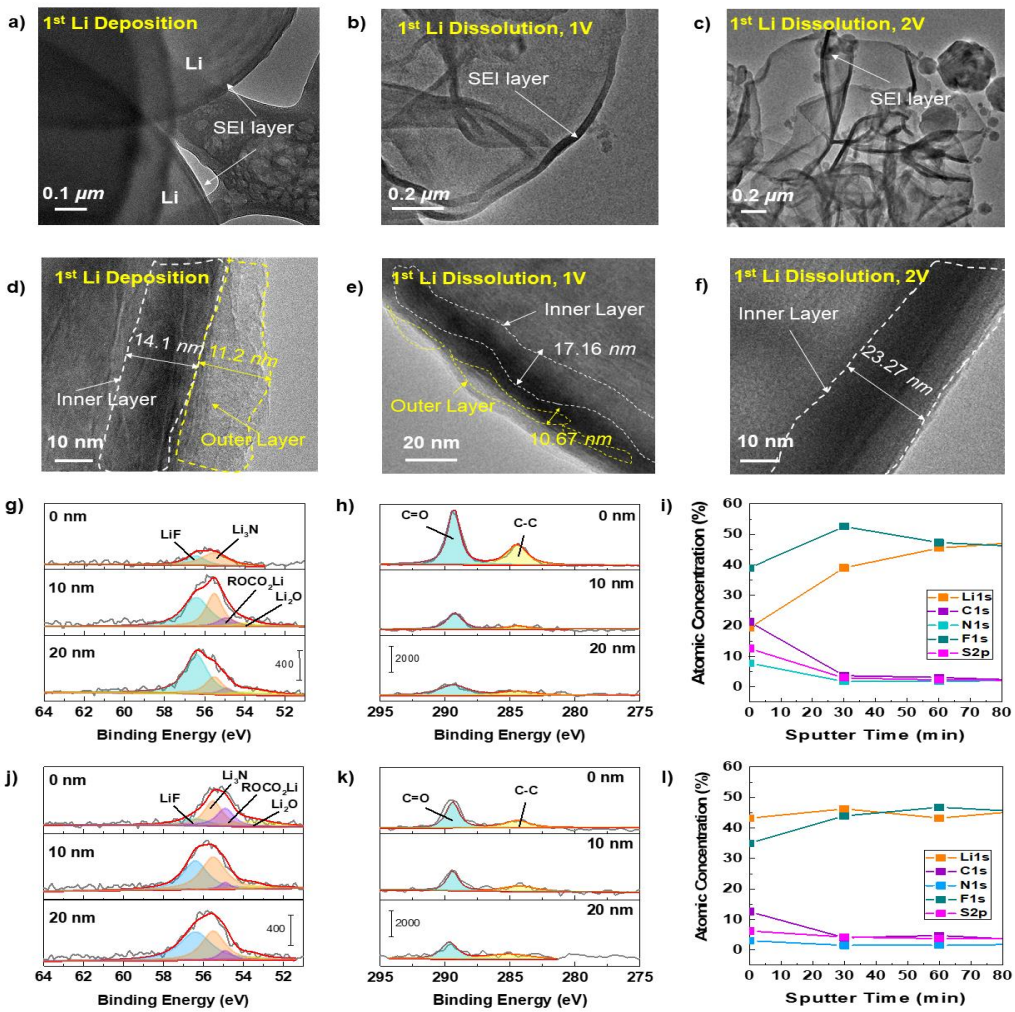

Figure 2.2.3.1. Cryogenic electron microscopy (Cryo-TEM) analysis of SEI nanostructure formed at different electrochemical stripping at 1V. and 2V. and XPS analysis on the SEI layer after Li stripping at the 1st cycle in Cu/Li cells. a) and d), Li metal deposited on the 200-Cu mesh using 1 M LiTFSi 3wt% $LiNO_3$ in DOLDME electrolyte with 1.267 mA, for 30 minutes. Stripping Li by working potential reach 1 V (b,e) and 2 V (c,f). g) and j) Li 1s spectra for 1V and 2V

stripping, respectively. h) and k) C 1s spectra for 1V and 2V stripping, respectively. The quantified atomic composition ratios of the SEI at different sputtering times i) 1V stripping and l) 2V stripping. All the XPS results were cycled by using 1 M LiTFSi 3wt% $LiNO_3$ in DOLDME electrolyte and The binding energy was calibrated with C 1s at 284.8 eV.

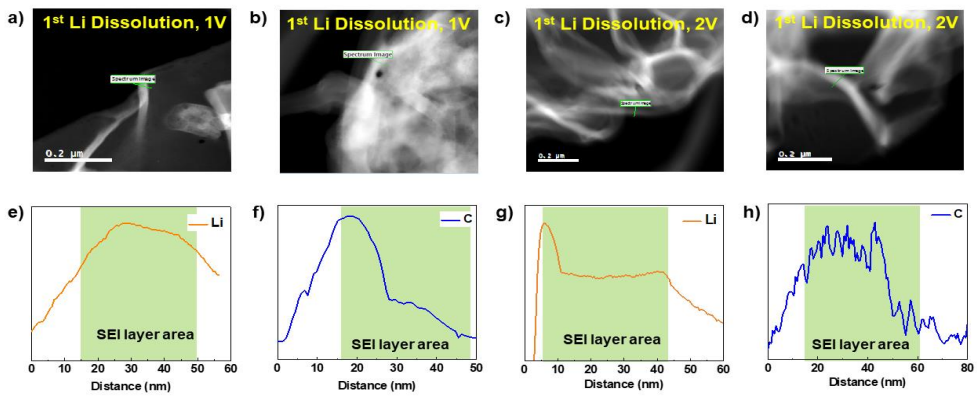

Figure 2.2.3.2. Electron energy loss spectroscopy (EELS) from cyro-EM characterization. a) and e), STEM image and Li K- edge spectra for SEI layer of 1V stripping. b) and f), STEM image and C K- edge spectra for SEI layer of 1V stripping. c) and g), STEM image and Li K- edge spectra for SEI layer of 2V stripping. d) and h), STEM image and C K- edge spectra for SEI layer of 2V stripping. IN all EELS analysis, the cell was cycling with 1.267 mA current density and 30-minute deposition. Electrolyte 1 M LiTFSi 3wt% $LiNO_3$ in DOLDME.

2.2.3.3. Post-cycling analysis.

We used scanning electron microscopy (SEM) to describe the effect between homogeneity and non-homogeneity. As shown in **Figure 2.2.3.3a and b**, 1V cut after 10 and 100 cycles respectively shows cracking and high surface area of the surface morphology. These results represent a non-uniform accumulation of Li. This is mainly due to the inhomogeneous SEI layer and the uneven electrical distribution to the Cu foil leading to rupture of the SEI layer and improper Li morphology. Moreover, **Figure 2.2.3.3c** shows remain of residual SEI and dead Li after 100 cycles thick about 76 μm, which is thicker than 2V cut off at 100 cycles (**Figure 2.2.3.3f**). In contrast, 2V cut-off both 10 and 100, surface are show smooth and perfect SEI layer corresponding with previous literature, that use $LiNO_3$ ether-based electrolyte[9]. This demonstrates that even if the cell cycled 100 times, the SEI remained consistent. It has a low surface area and less dead SEI. As shown **in Figure 2.2.3.3f** in cross-section view, the thickness of remain SEI and dead Li are only 30 μm.

In addition, to analyze the performance of the cycle in real time. We performed in-situ optical microscopy (in-situ OM) experiments. As shown **in Figure 2.2.3.3g**, 1V cycling show rapidly consumption of Li source and electrolyte, leading to increasing of high local current density, extremely rapidly uneven Li growth and breaking of SEI as show 50 cycles image capture. As shown **in Figure 2.2.3.3g** and, 1V cycling shows the rapid use of a Li source and electrolyte. This leads to an increase in high local current density, extremely rapid non-uniform Li growth, generated dead Li and SEI breakage from 50 capture cycles. The shiny silver lithium caused the black SEI layer to suddenly crack. On the other hand, 2V

maintains stable performance of 400 cycles without breaking the SEI, **as shown in Figure 2.2.3.3h.** Meanwhile, the color of the SEI layer in in-situ OM shows different. In 1V show slide silver color of the SEI layer, which possibly comes from dead Li contained in the layer. In contrast, 2V shows only the black color of the SEI layer, without the silver color of the dead Li. These results confirm that clipping 2 V with a uniform SEI layer can result in consistent Li-ion deposition and dissolution in the SEI layer. each round This greatly improves the efficiency of the cycle. Furthermore, the uniform ionic conductivity of SEI nanostructure has been identified as the controlling parameter of Li transport, we still need to quantify where SEI ionic conductivity affects the Li-ion deposition behavior. **As shown in Figure 2.2.3.4a**, a COMSOL simulation of typical Li deposition on the Cu foil (dash line is a boundary of Cu foil current collector) without SEI layer. Without the SEI layer, Li appears to be plated on the edge of the Cu foil due to the local current density and Li-ion concentration gradient in the interface between the electrode and the electrolyte. However, in practical, all the electrochemical battery cells, always form the SEI layer, which is in our case form a double layer of SEI. Thus we also simulate the general double layer of SEI **in Figure 2.2.3.4 b** shows the Li deposition behavior after Cu foil form a double SEI layer.

In practice, however, all electrochemical battery cells generate an SEI layer, in which case we simulate double SEI layers. Two layer of SEI in **Figure 2.2.3.5b**, showing the Li deposition behavior after the Cu foil creates the second SEI layer. We model the Li diffusion of outer SEI layer lower than the electrolyte for 1/5 time and inner layer slower than outer layer for 1/10 time to simulate the effect of the difference of Li diffusion in a double layer of SEI. According to previous studies, the organic SEI layer is known as the fast Li+ transport[35, 36] and, in particular,

mechanical elasticity. As the result, a Cu anode with a SEI layer twice the slow rate of Li diffusion, showing a more intense non-uniform Li plating than without SEI. This phenomenon is consistent with previous studies as a result of SEI's low ionic conductivity can cause significant dendrites to grow. Because the poor ionic conductivity of SEI increases the local current density, causing uneven Li plating[37, 38]. Additionally, to study the cracking of the double SEI layer due to 1V, we also simulated the SEI layer after peeling off the 1V with the cracked SEI surface as shown **in Figure 2.2.3.4c**. As a result, crack regions with higher ionic conductivity are more induced to Li ion plating than other areas, leading to Li-needle growth morphology. While the case of the 2V strip shows off the Li smooth deposit as shown **in Figure 2.2.3.4d**. This smooth deposit comes from the homogeneous SEI layer. Moreover, the 2V strip out shows smoother Li plated than normal double SEI layer. Because removing the outer layer enhance the Li diffusion of SEI. From the COMSOL simulations, the effect of SEI ion conduction and Li plating behavior in the nanostructures was clearly explained. Similarly to the schematic model of the mechanism as shown in **Figure 2.2.3.4e-i.** In the first deposition of Li, SEI formed several organic and inorganic layers. The inner layer is the inorganic layer. and the outer layer is the organic layer **as shown in Figure 2.2.3.4e**. After we dissolution Li at the 1 V cut-off, the organic layer can break. Therefore, it will cause uneven ion conduction and cause uneven Li plating as shown **in Figure 2.2.3.4f and 3g**. In contrast, at the 2 V cut-off, the organic layer is removed. The remainder of the inorganic layer, which has a uniform ion conductivity of SEI, therefore, after the second deposition, the Li-ion is evenly impregnated in the case of a 2 V cut-off, but in the case of a 1V cut-off is shown. that dendrite grows due to the uneven ion conductivity of the SEI layer, as shown **in Figure 2.2.3.4h and 3i**.

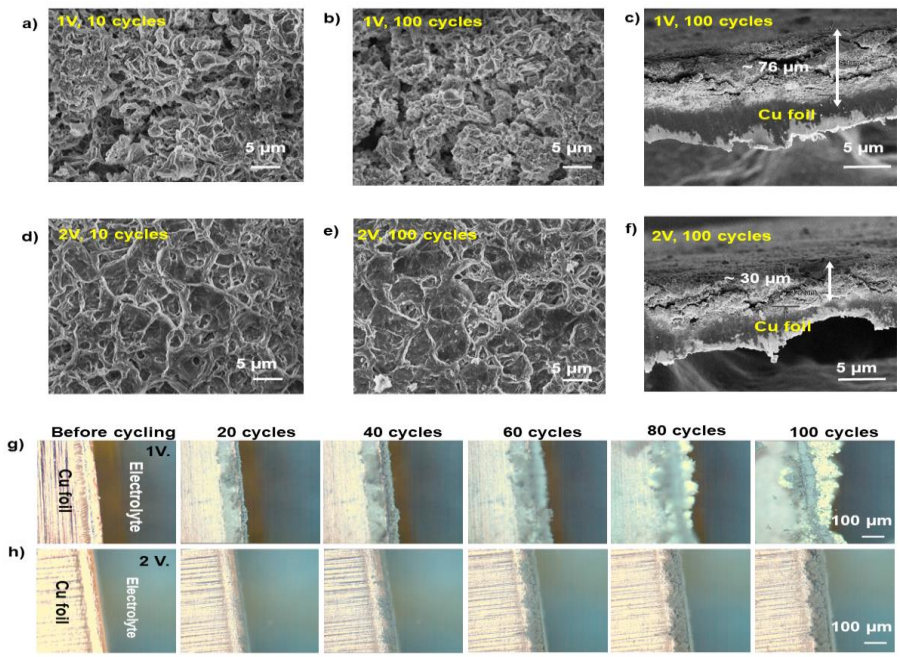

Figure 2.2.3.3. Morphology characterization of surface and cross-section after cycles. SEM images of top view of 1V stripping after 10 cycles a), 100 cycles b) and 1V cross-section view after 100 cycles c). 2V stripping after 10 cycles d) and 100 e) and 2 V cross-section after 100 cycles f). As well as, capture images of in-situ optical microscopy for 1V g) and 2V h) stripping. All morphology characterization has been done with 1 M LiTFSi 3wt% $LiNO_3$ in DOLDME electrolyte.

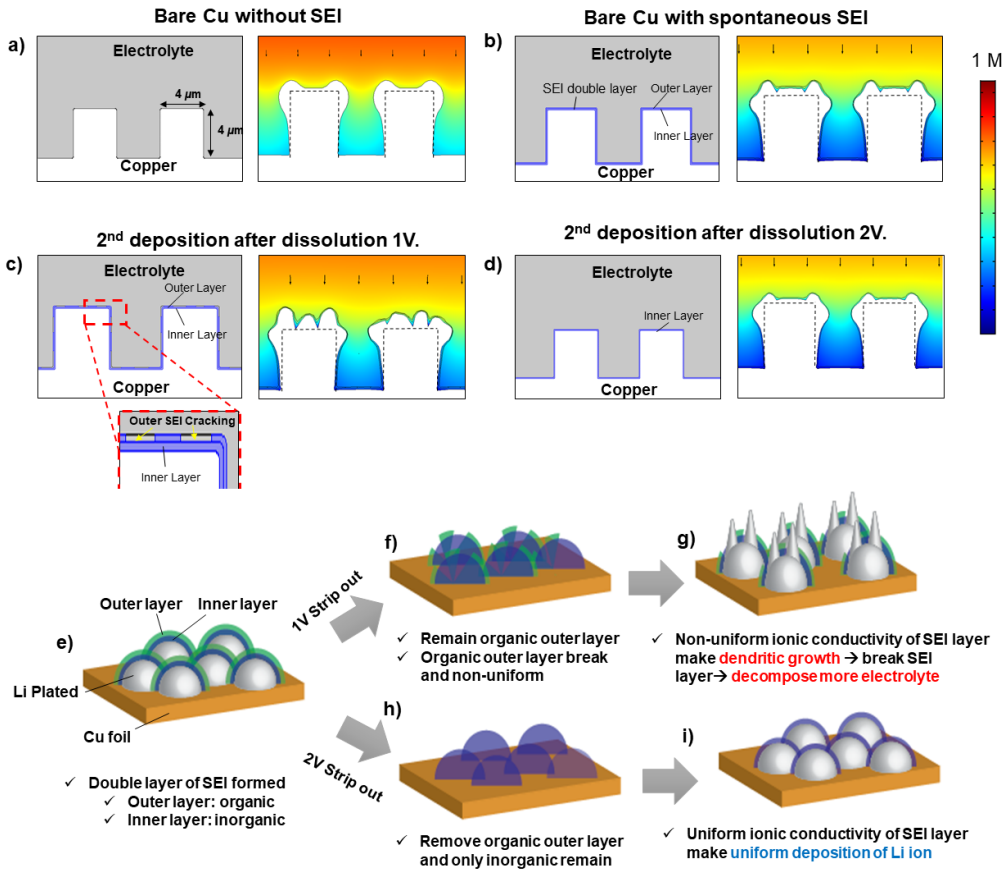

Figure 2.2.3.4. COMSOL simulation of Li deposition through homogeneous and inhomogeneous SEI layer. a) , Li deposited on protuberance of Cu foil without SEI. b) , Li deposited on protuberance of Cu foil with a double layer of SEI. c), Li deposited through inhomogeneous SEI with crack layer model (SEI forming from 1V stripping). d), Li deposited through homogeneous single inner SEI layer (SEI forming from 2V). e)-i) the mechanism schematic of 1 V. and 2 V. cut off.

2.2.3.4. Enhanced cycle stability demonstrated by anode free batteries

In this study, an ether-based electrolyte (1 M LiTFSi 3%wt $LiNO_3$ in DOL/DME) was used as an electrolyte in this experiment. The Cu/Li coin cell configuration has been tested with 1 mA/cm^2 in 30 minutes per deposition (0.5 mAh/cm^2). The voltage cut-off for dissolution has been set for 1V as a reference, which this voltage cut off has been widely used for Cu/Li electrochemical cell test[24, 39-41]. However, the ideal voltage cut-off for strip out Li is 0V (Reduction potential -3.04 V vs. the standard hydrogen electrode). We increase the strip out voltage cut-off of the cell to 2V and found the unexpectedly enhanced the long cycle stability up to 400 cycles, without degradation for coulombic efficiency as shown in **Figure 2.2.3.5a**. In contrast, the reference cell with 1V shows coulombic efficiency rapidly decreasing after 100 cycles similar to other literature previous report[42-44]. The quick capacity loss in Cu/Li cells has been well known as used out of the electrolyte. The electrolyte and Li source from the cathode is extremely limited in zero surplus lithium batteries. Both electrolyte and Li sources are rapidly depleted due to continuous electrolyte degradation and dead Li production. Irregular Li plating can cause Li to grow abnormally. This leads to SEI breakage and further high surface area creation[30, 45]. The high surface area of the Li deposition is the major cause of consumption electrolyte. Moreover, the unwanted Li needle-like morphology generates the dead Li in the stripping process[46]. However, with 2V cut-off, better cycle stability is achieved. Due to the uniform plating of Li compared to 1V, the uniform deposition of Li is mainly due to the homogeneous SEI layer [11-13]. To prove this fact, we therefore test the stability of the electrochemical cycle, by pre-

cycles the cell with 2V for 50 cycles to achieve a homogeneous SEI on Cu foil before 1V is converted to normal condition. As shown in **Figure 2.2.3.5a**, after cycling 2V for 50 cycles and switch to 1 V, the cycle stability enhanced to 200 cycles. This means that pre-cycles of 2V has built uniform SEI layer, leading to guide Li-ion uniformly plated. Even though switching to a normal situation (1V) the homogeneously SEI still protects and improves the cycle stability better than solely 1V. Moreover, we conduct more hard condition of electrochemical test, 3 and 5 mA/cm^2 as show in **Figure 2.2.3.6 a and b.** The test results show much improvement of cycle stability. **Figure 4b and 4c** demonstrate the voltage profile of 1V and 2V Li/Cu cell of Li deposition and dissolution process. At the first cycle, both 1V and 2V show a little large overpotential, which are quite similar value for both of them. However, after some cycles, 2V show decreasing of voltage hysteresis, in contrast 1V case show continuously increasing of overpotential. To more clearly define, we plot average overpotential stripping and plating for both of 1V and 2V as show in **Figure 2.2.3.6 c and d**. Cleary elucidates that 1V case has a steadily increasing overpotential, which means that the internal resistance during electrochemical cycling raises up. The 1V cut off increases avg. overpotential over -60 mV for plating and 60 mV for striping after 100 cycles. The increased voltage hysteresis after several cycles in bare Cu is due to the forming of an abnormally thick SEI layer and dead Li. The useless thick SEI layer and dead Li can cause Li to struggle in the deposition and dissolution behavior, leading to high internal resistance and overpotential[13, 47, 48]. In contrast, 2V cut of shows consistency lower overpotential than 1V. Even though after 80 cycles, where 1V starts shows rapid increase overpotential, but 2V still remains stable overpotential. This coincidence confirms that the deposition and dissolution behavior of 2V is easily and uniformly

process. Therefore, the stable SEI layer from 2V can cause uniform Li deposition suppress high surface area, and dendritic growth. To further, demonstrates the benefits of high potential 2V on anode-free batteries. Cu foil was paired with a traditional $LiFePO_4$ cathode using the same electrolyte with Li/Cu half-cell test: 1M LiTFSi 3wt% $LiNO_3$ in DOLDME electrolyte in coin cell configuration.

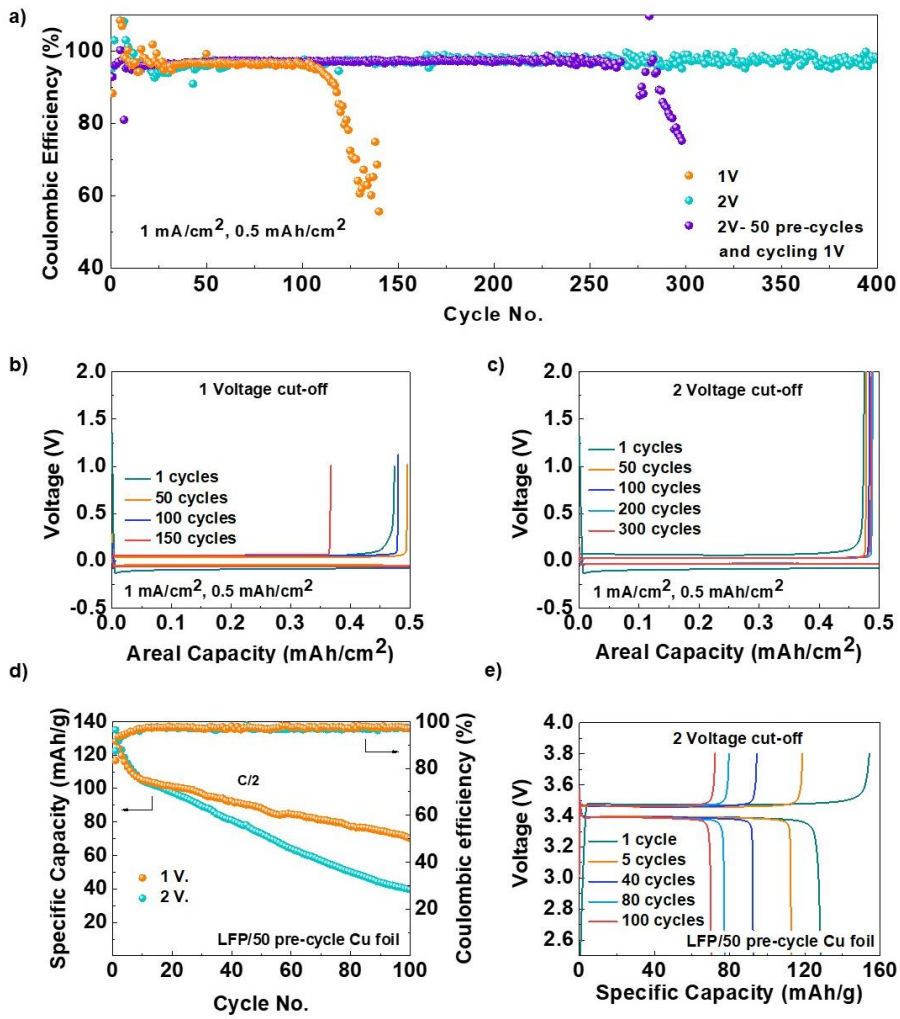

Figure 2.2.3.5. Electrochemical behavior of 1 Voltage and 2 Voltage cut off by Li/Cu and $LiFePO_4$ cells. All cells were cycled in 1 M LiTFSi 3wt% $LiNO_3$ in DOLDME electrolyte. a). Coulombic efficiency of Li/Cu cells cycled by 1V, 2V, and 2V 50 cycles and change to 1V, respectively, at current density 1 mA/cm^2 and

areal capacity 0.5 mAh/cm^2. Voltage profiles of different cycles for Li/Cu cells cycled at 1V b) and 2V c) cut off. d), cycling performance and capacity after 50 pre-cycles of 1 and 2V stripping, respectively. e) voltage profiles of $LiFePO_4$/Cu cell at selected cycles after 50 pre-cycles of 2V stripping.

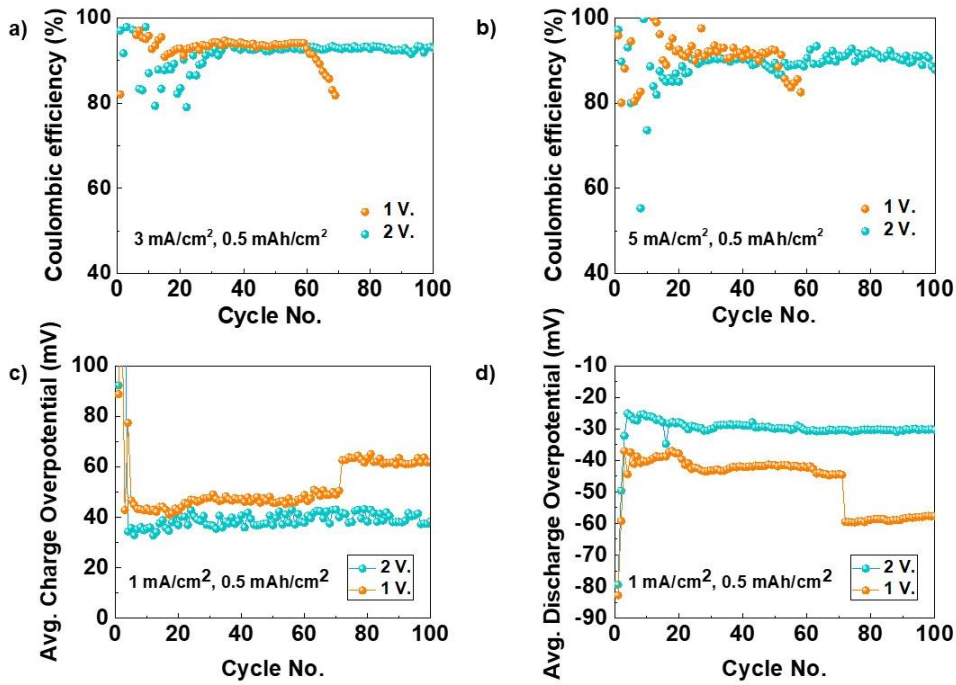

Figure 2.2.3.6. Electrochemical behavior of 1 Voltage and 2 Voltage cut off by Li/Cu cells. a) and b) coulombic efficiency of Li/Cu cells cycled by 1V and 2V at current density 3 mA/cm^2 and 5 mAh/cm^2, areal capacity 0.5 mAh/cm^2 respectively. c) and d), average charge and discharge overpotential of 1 V and 2 V, respectively, at 1 mA/cm^2 and areal capacity 0.5 mAh/cm^2.

2.2.3.5. Extended cycling stability performance demonstrated by LiFePO4/Cu cells

To further demonstrate the beneficial effect of high voltage cut off at 2V on the anode free battery performance, Cu foil was pre-form the SEI layer by Li/Cu coin cell configuration paired with a traditional $LiFePO_4$ cathode using the same electrolyte with Li/Cu half-cell test: 1M LiTFSi 3wt% $LiNO_3$ in DOLDME electrolyte in coin cell configuration. We pre-cycling Li/Cu for 50 cycles for both 1V and 2V anode cut off, after that, we take the Cu foil with SEI form paired with $LiFePO_4$ as show the result of cycle stability **in Figure 2.2.3.5d.** However, we employ 50 cycles as a pre-cycling stage for a reason. Since we evaluated the cycle stability of many pre-formed SEI in Li/Cu cells (10, 25, 50, and 100 cycles of recycle), the 50 pre-cycles demonstrated the most stable spin, as indicated **in the Figure 2.2.3.7.** As shown in the **Figure 2.2.3.5d**, the difference between the charge and discharge voltage plateau with 2V pre-form SEI is decreasing relative to 1V pre-form SEI, benefitting from uniform deposition and dissolution of the anode, leading to less capacity loss in each cycle. As a result, the 2V pre-form SEI cell show much better stability after 100 cycles remain 70.13 mAh/g and 54.66 % capacity retention, compare to the 1V pre-form SEI cell have a capacity remain at 100 cycles 39.6 mAh/g and 29.33% capacity retention as shown **in Figure 2.2.3.5e**. Moreover, we also test the Cu/LFP full cell test in convenience condition. As shown in **Figure 2.2.3.8 a-d** this cell configuration is Cu/LFP and control the voltage as 3.8-2.45 for 1V cut off condition and 3.8-1.45 for 2 V cut off condition without delithiated capacity from LFP. Thus, in this method, the voltage of the anode won’t accurate and in the early cycle, but after several cycles, the capacity

will lose and finally the voltage cut off of the anode will reach the 1 V and 2 V eventually. As the results shown in **Figure 2.2.3.8 a-d,** even though in this condition 2V cut-off showed more improvement than 1V cut-off. This confirms that the changing of the SEI layer in nanostructure is a powerful method to improve the performance of the battery. Our new findings inspired people to attend to the Li dissolution effect to SEI nanostructure not only the Li deposition effect to SEI.

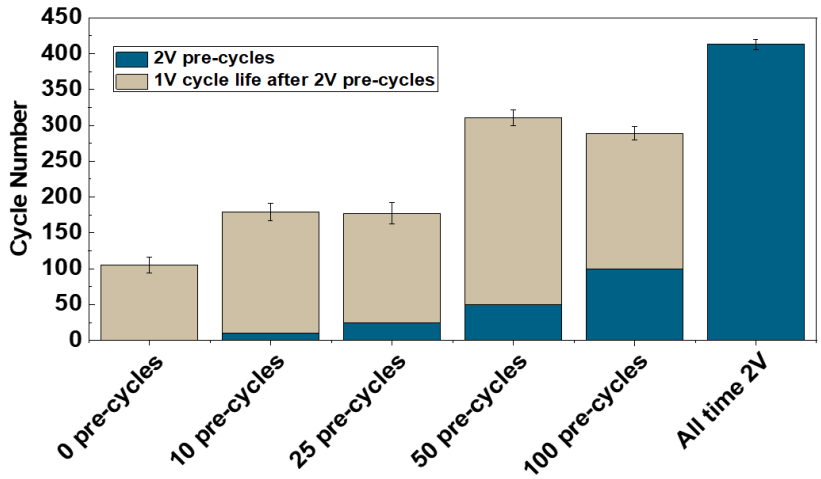

Figure 2.2.3.7. Pre-cycling in Li/Cu cell. All the cell was cycling with 1 M LiTFSi 3wt% $LiNO_3$ in DOLDME electrolyte.

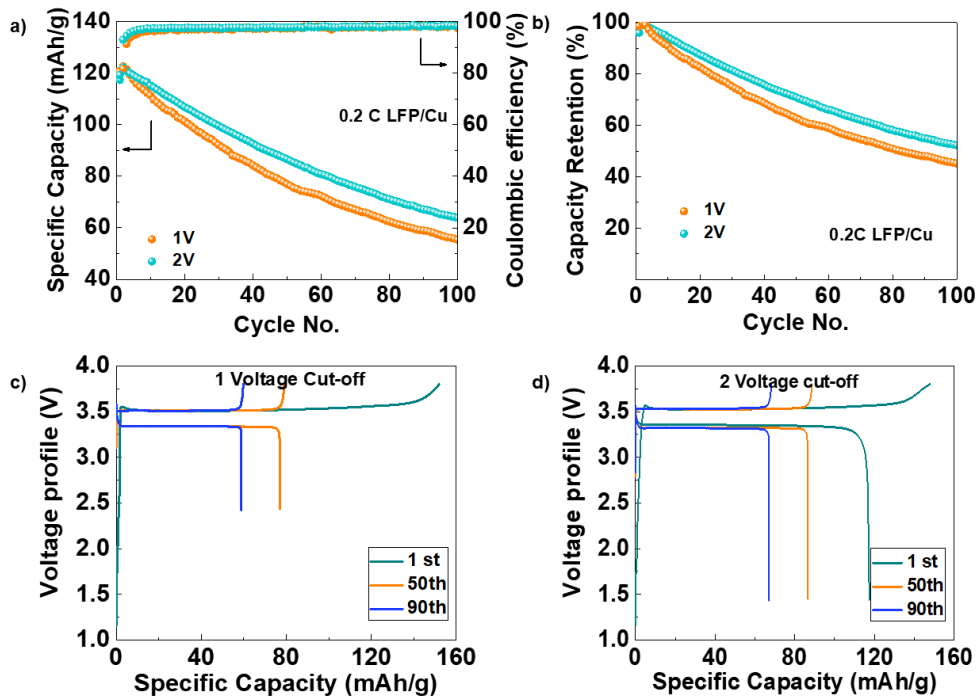

Figure 2.2.3.8. Electrochemical behavior of 1Voltage and 2 Voltage cut off by $LiFePO_4$/Cu cells. a) cycling performance of $LiFePO_4$/Cu cells and b), capacity retention between 1V and 2V anode stripping respectively. c) and d), voltage profiles of $LiFePO_4$/Cu cell at selected cycles of 1 and 2V stripping, respectively.

2.2.4. Conclusion

In conclusion, we've discussed a simple technique. However, this is not a simple process. In electrochemical stripping, a monolithic inorganic SEI layer is formed by polishing the organic nanocrystal SEI layer. The nanostructure of SEI layer characterization features by Cryo-TEM. Cryo-TEM reveals the nanostructure of SEI layer 1V and 2V. The outer organic layer is easily dissolved and cracked during the cycle. This leads to a non-homogeneous SEI layer, which results in uneven

deposition and dissolution of Li. Therefore, polishing an outer organic layer can enhance the uniformity of SEI. 2V anode dissolution cut off to remove the outer organic layer and remain only homogenous inorganic SEI layer, leading to uniform Li plated and strip out. The 2V cut off cycle stability in Li/Cu half-cell reach 400 cycles in 1 M LiTFSi 3%$LiNO_3$ in DOLDME, compare with 1V cut off only can go as 100 cycles before rapid dried out electrolyte leading to degradation of cycle stability. The new finding in this study opens a new research question to explore. Especially, the unknown polishing outer organic layer by electrochemical Li dissolution effect to SEI nanostructure will be critical in giving insight for caring Li dissolution process leading to rationally designing nanostructure SEI layer by simple electrochemical.

2.2.5. Reference

1. G. Berckmans, M. Messagie, J. Smekens, N. Omar, L. Vanhaverbeke and J. Van Mierlo, *Energies*, 2017, **10**, 1314.

2. J. Betz, G. Bieker, P. Meister, T. Placke, M. Winter and R. Schmuch, *Advanced Energy Materials*, 2019, **9**, 1803170.

3. O. Schmidt, A. Hawkes, A. Gambhir and I. Staffell, *Nature Energy*, 2017, **2**, 17110.

4. B. Nykvist and M. Nilsson, *Nature Climate Change*, 2015, **5**, 329-332.

5. P. Albertus, S. Babinec, S. Litzelman and A. Newman, *Nature Energy*, 2018, **3**, 16-21.

6. R. Weber, M. Genovese, A. J. Louli, S. Hames, C. Martin, I. G. Hill and J. R.

Dahn, *Nature Energy*, 2019, **4**, 683-689.

7. A. J. Louli, A. Eldesoky, R. Weber, M. Genovese, M. Coon, J. deGooyer, Z. Deng, R. T. White, J. Lee, T. Rodgers, R. Petibon, S. Hy, S. J. H. Cheng and J. R. Dahn, *Nature Energy*, 2020, **5**, 693-702.

8. C. Yan, Y.-X. Yao, X. Chen, X.-B. Cheng, X.-Q. Zhang, J.-Q. Huang and Q. Zhang, *Angewandte Chemie International Edition*, 2018, **57**, 14055-14059.

9. W. Li, H. Yao, K. Yan, G. Zheng, Z. Liang, Y.-M. Chiang and Y. Cui, *Nature Communications*, 2015, **6**, 7436.

10. Y. Liu, D. Lin, Y. Li, G. Chen, A. Pei, O. Nix, Y. Li and Y. Cui, *Nature Communications*, 2018, **9**, 3656.

11. Y. Li, W. Huang, Y. Li, A. Pei, D. T. Boyle and Y. Cui, *Joule*, 2018, **2**, 2167-2177.

12. W. Huang, D. T. Boyle, Y. Li, Y. Li, A. Pei, H. Chen and Y. Cui, *ACS Nano*, 2019, **13**, 737-744.

13. J. Wang, W. Huang, A. Pei, Y. Li, F. Shi, X. Yu and Y. Cui, *Nature Energy*, 2019, **4**, 664-670.

14. X. Cao, X. Ren, L. Zou, M. H. Engelhard, W. Huang, H. Wang, B. E. Matthews, H. Lee, C. Niu, B. W. Arey, Y. Cui, C. Wang, J. Xiao, J. Liu, W. Xu and J.-G. Zhang, *Nature Energy*, 2019, **4**, 796-805.

15. E. Peled, D. Golodnitsky and G. Ardel, *Journal of the Electrochemical Society*, 1997, **144**, L208.

16. E. Peled and S. Menkin, *Journal of The Electrochemical Society*, 2017, **164**,

A1703.

17. D. Aurbach, E. Pollak, R. Elazari, G. Salitra, C. S. Kelley and J. Affinito, *Journal of the Electrochemical Society*, 2009, **156**, A694.

18. K. Xu, *Chemical Reviews*, 2014, **114**, 11503-11618.

19. P. Lu and S. J. Harris, *Electrochemistry Communications*, 2011, **13**, 1035-1037.

20. A. Wang, S. Kadam, H. Li, S. Shi and Y. Qi, *npj Computational Materials*, 2018, **4**, 15.

21. S. J. An, J. Li, C. Daniel, D. Mohanty, S. Nagpure and D. L. Wood, *Carbon*, 2016, **105**, 52-76.

22. R. Mogensen, D. Brandell and R. Younesi, *ACS Energy Letters*, 2016, **1**, 1173-1178.

23. H. Pan, K. S. Han, M. H. Engelhard, R. Cao, J. Chen, J.-G. Zhang, K. T. Mueller, Y. Shao and J. Liu, *Advanced Functional Materials*, 2018, **28**, 1707234.

24. X. Fan, L. Chen, X. Ji, T. Deng, S. Hou, J. Chen, J. Zheng, F. Wang, J. Jiang, K. Xu and C. Wang, *Chem*, 2018, **4**, 174-185.

25. C. Fu, Y. Ma, S. Lou, C. Cui, L. Xiang, W. Zhao, P. Zuo, J. Wang, Y. Gao and G. Yin, *Journal of Materials Chemistry A*, 2020, **8**, 2066-2073.

26. X. Fan, L. Chen, O. Borodin, X. Ji, J. Chen, S. Hou, T. Deng, J. Zheng, C. Yang, S.-C. Liou, K. Amine, K. Xu and C. Wang, *Nature Nanotechnology*, 2018, **13**, 715-722.

27. K. Yan, J. Wang, S. Zhao, D. Zhou, B. Sun, Y. Cui and G. Wang, *Angewandte Chemie*, 2019, **131**, 11486-11490.

28. Y. Li, Y. Li, A. Pei, K. Yan, Y. Sun, C.-L. Wu, L.-M. Joubert, R. Chin, A. L. Koh, Y. Yu, J. Perrino, B. Butz, S. Chu and Y. Cui, *Science*, 2017, **358**, 506.

29. H. Park, O. Tamwattana, J. Kim, S. Buakeaw, R. Hongtong, B. Kim, P. Khomein, G. Liu, N. Meethong and K. Kang, *Advanced Energy Materials*, 2020, **n/a**, 2003039.

30. A. Pei, G. Zheng, F. Shi, Y. Li and Y. Cui, *Nano Letters*, 2017, **17**, 1132-1139.

31. T. Wang, Y. Li, J. Zhang, K. Yan, P. Jaumaux, J. Yang, C. Wang, D. Shanmukaraj, B. Sun, M. Armand, Y. Cui and G. Wang, *Nature Communications*, 2020, **11**, 5429.

32. Y. Gu, W.-W. Wang, Y.-J. Li, Q.-H. Wu, S. Tang, J.-W. Yan, M.-S. Zheng, D.-Y. Wu, C.-H. Fan, W.-Q. Hu, Z.-B. Chen, Y. Fang, Q.-H. Zhang, Q.-F. Dong and B.-W. Mao, *Nature Communications*, 2018, **9**, 1339.

33. W.-W. Wang, Y. Gu, H. Yan, S. Li, J.-W. He, H.-Y. Xu, Q.-H. Wu, J.-W. Yan and B.-W. Mao, *Chem*, 2020, **6**, 2728-2745.

34. C. Zhang, Q. Lan, Y. Liu, J. Wu, H. Shao, H. Zhan and Y. Yang, *Electrochimica Acta*, 2019, **306**, 407-419.

35. R. He, M. Echeverri, D. Ward, Y. Zhu and T. Kyu, *Journal of Membrane Science*, 2016, **498**, 208-217.

36. Y. Zhao, G. Li, Y. Gao, D. Wang, Q. Huang and D. Wang, *ACS Energy Letters*, 2019, **4**, 1271-1278.

37. G. Yoon, S. Moon, G. Ceder and K. Kang, *Chemistry of Materials*, 2018, **30**, 6769-6776.

38. S. Moon, H. Park, G. Yoon, M. H. Lee, K.-Y. Park and K. Kang, *Chemistry of Materials*, 2017, **29**, 9182-9191.

39. G. Wang, X. Xiong, Z. Lin, J. Zheng, Z. Fenghua, Y. Li, Y. Liu, C. Yang, Y. Tang and M. Liu, *Nanoscale*, 2018, **10**, 10018-10024.

40. Z. Liang, G. Zheng, C. Liu, N. Liu, W. Li, K. Yan, H. Yao, P.-C. Hsu, S. Chu and Y. Cui, *Nano Letters*, 2015, **15**, 2910-2916.

41. B. D. Adams, J. Zheng, X. Ren, W. Xu and J.-G. Zhang, *Advanced Energy Materials*, 2018, **8**, 1702097.

42. J. Luo, C.-C. Fang and N.-L. Wu, *Advanced Energy Materials*, 2018, **8**, 1701482.

43. Z. Yu, D. G. Mackanic, W. Michaels, M. Lee, A. Pei, D. Feng, Q. Zhang, Y. Tsao, C. V. Amanchukwu, X. Yan, H. Wang, S. Chen, K. Liu, J. Kang, J. Qin, Y. Cui and Z. Bao, *Joule*, 2019, **3**, 2761-2776.

44. W. Liu, D. Lin, A. Pei and Y. Cui, *Journal of the American Chemical Society*, 2016, **138**, 15443-15450.

45. J. Xiao, *Science*, 2019, **366**, 426-427.

46. C. Fang, J. Li, M. Zhang, Y. Zhang, F. Yang, J. Z. Lee, M.-H. Lee, J. Alvarado, M. A. Schroeder, Y. Yang, B. Lu, N. Williams, M. Ceja, L. Yang, M. Cai, J. Gu, K. Xu, X. Wang and Y. S. Meng, *Nature*, 2019, **572**, 511-515.

47. D. T. Boyle, W. Huang, H. Wang, Y. Li, H. Chen, Z. Yu, W. Zhang, Z. Bao and

Y. Cui, *Nature Energy*, 2021, **6**, 487-494.

48. K. Pu, X. Qu, X. Zhang, J. Hu, C. Gu, Y. Wu, M. Gao, H. Pan and Y. Liu, *Advanced Science*, 2019, **6**, 1901776.

Chapter 3. A bifunctional auxiliary electrode for safe lithium metal batteries

(The content of this chapter has been published in, Reproduced with permission from Tamwattana O. et al. A bifunctional auxiliary electrode for safe lithium metal batteries. *J. Mater. Chem. A.*, 2019, 7, 24807-24813. Copyright 2019, Royal Society of Chemistry)

3.1. Introduction

The demand for rechargeable batteries with higher energy density than lithium ion batteries that are commercially available has been ever increasing[1, 2]. Elemental lithium metal has thus come into the spotlight again as one of the most promising negative electrode materials owing to its exceptionally high theoretical capacity (3860 mAh g^{-1}) and the lowest negative electrochemical potential (-3.040 V *vs*. a standard hydrogen electrode)[3, 4]. However, the commercialization of rechargeable lithium metal batteries (LMBs) has been retarded due to the catastrophic safety issue arising from lithium dendrite formation. Even with a small irregularity in lithium metal deposition during the initial stage of charge, further selective and self-amplifying lithium deposition follows due to the presence of favorable deposition sites. The inhomogeneous lithium deposition depending on operating conditions leads to the formation of dendrite in a variety of morphologies such as filamentary, mossy or fork-like shapes, which is related to the possibility of short circuit phenomena{Bai, 2018 #82}[5-7]. The needle-like lithium dendrite can

penetrate the polymer separator and possibly contact the opposite electrode, and such contact would result in a huge current flow through the internal circuit, triggering joule heating thermal runaway[8,9].

Over the last few decades, tremendous efforts have been focused on elucidating the dendritic growth mechanism [10, 11] and preventing lithium dendrite formation. Although much progress has been made in understanding the lithium dendritic growth, the development of reliable techniques for controlling the surface morphology from heterogeneous reactions still remain an obstacle. Various attempts, such as introduction of electrolyte additives[12-14] to avoid undesirable reactions at the lithium surface, a three-dimension current collector[15, 16] to induce uniform reactions and a physically protective layer have been explored[17, 18]. Unfortunately, it has been revealed that the dendrite formation cannot be completely inhibited and such approaches are only valid at low current densities and/or with low utilization level of lithium metal anodes. Batteries operating under extreme conditions might still be exposed to the potential risk of dendrite growth and the internal short-circuit. Therefore, not only protective techniques for lithium metal, but also sensing technologies to detect dendritic growth in advance are needed. Recently, Wu *et al.* reported an early detection technique, where a metallic copper was sputtered on the separator to detect the electrical shortage caused by lithium metal penetration through the separator[19]. The functional separator could successfully detect the internal shorting when the lithium dendrite penetrated into the separator, enabling the alarming of the cell failure. Nevertheless, it is questionable whether this early detection would be practically linked to the prevention of the actual cell failure in consideration of the typical dendrite growth

rate (5.1 μm sec^{-1} at a current density 50 mA cm^{-2}, Figure 3.1.1). The detection of the shortage means that the lithium has already substantially grown and is at the risk of the contact to counter electrode, having passed through the separator. As the thickness of conventional separator is < 12 μm, the time from the sensing to the potential safety hazard is only less than a few seconds. Moreover, at higher current rates for fast charging or discharging, the detection would not simply offer a sufficient time to stop the catastrophic reaction.

Herein, we explored a more advanced concept of the safety sensor, which not only detects the internal electrical short, but also plays a role of lithium scavenging agent. In this concept, an auxiliary electrode signals an internal short-circuit in real-time, and, upon the short-circuit of the battery, it scavenges a certain amount of lithium, preventing further growth of dendrite, allowing enough time to shut down the circuit without incurring a safety hazard.

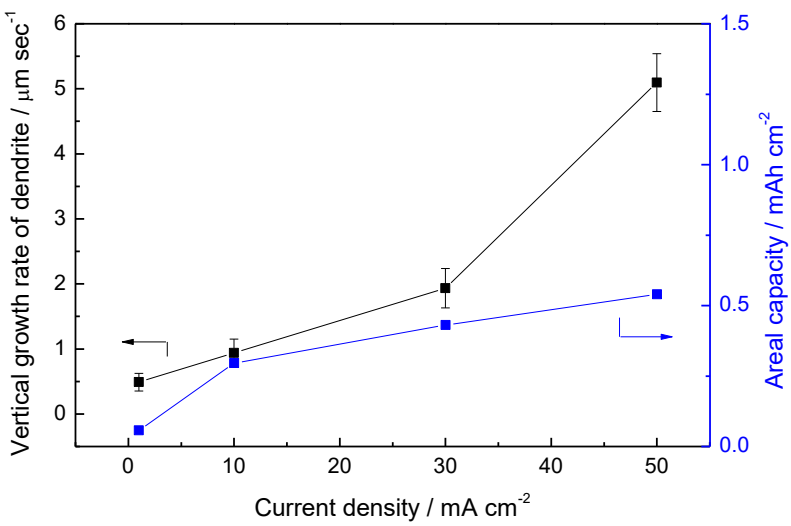

Figure 3.1.1. Vertical growth rate of dendrite at various current densities. The black and blue lines represented vertical growth rate of dendrite and areal capacity,

respectively This experiment was conducted in sandwich cell. The piece of lithium foil was first pressed onto the case part of the cell and cover by customized PVDF rings (outer diameter = 16.5 mm, inner diameter = 8 mm, thickness = 100 μm). The electrolyte was dropped on the surface of lithium. Finally, the second lithium foil was plated on top of the customized PVDF. The whole cell was assembled in an Ar-filled glovebox using a CR2032-type coin cell with 300 μm thick Li foil. The estimate of vertical growth rate, with respect to the planar growth in the inner site of customizes PVDF rings, was possible by checking the time required for short-circuiting involving sudden voltage drops.

3.2. Working principle and auxiliary electrode design

3.2.1. The role and design of auxiliary electrode design

The working principle of an auxiliary electrode in sensing and scavenging is schematically illustrated in Figure 3.2.1, where an auxiliary electrode is inserted between the positive and negative electrodes. In the absence of an auxiliary electrode, the unwanted dendrite growth from the lithium surface eventually reaches the positive electrode, which potentially serves as an electron pathway with very low resistance. A large amount of electrons, driven by the potential difference between two electrodes, will pass through this pathway in an uncontrolled manner within a short time, and can possibly cause a thermal runaway due to the heat generated by the high current. This phenomenon is indicated by the near '0' voltage in the voltammeter shown in Figure 3.2.1a. In contrast, a real-time detection of dendrite growth can be achieved by inserting an auxiliary electrode between the separators (Figure 3.2.1b) [19]. Under this cell configuration, the auxiliary electrode

is designed to physically contact a growing lithium metal dendrite before it reaches the positive electrode. Upon the contact, a voltage change would be detected between the negative and the auxiliary electrodes (Figure 3.2.1b) and gives a warning signal to the battery user in real-time. Moreover, in our design of the bifunctional auxiliary electrode, it was intended that it should be also capable of taking up a certain amount of lithium, so that further development of dendrite growth toward the positive electrode can be inhibited for some time, achieving a partial self-healing with the safety detection.

For this aim, the material for an auxiliary electrode should be carefully selected and machined to fulfill the following requirements: (i) it should be capable of spontaneously accepting lithium ions from lithium metal ($\mu_{\text{auxiliary electrode}} < \mu_{\text{Li metal}}$: μ refers to the chemical potential of lithium) with a reasonably fast rate. (ii) the physical contact between the auxiliary electrode and dendrites should be easily recognizable. (iii) the capacity of the auxiliary electrode must be reliably determined, so that the amount of allowable lithium uptake and the data collection interval in the system can be verified. (iv) the auxiliary electrode should not undergo large volume change upon the lithiation and not interfere with the movement of lithium ions.

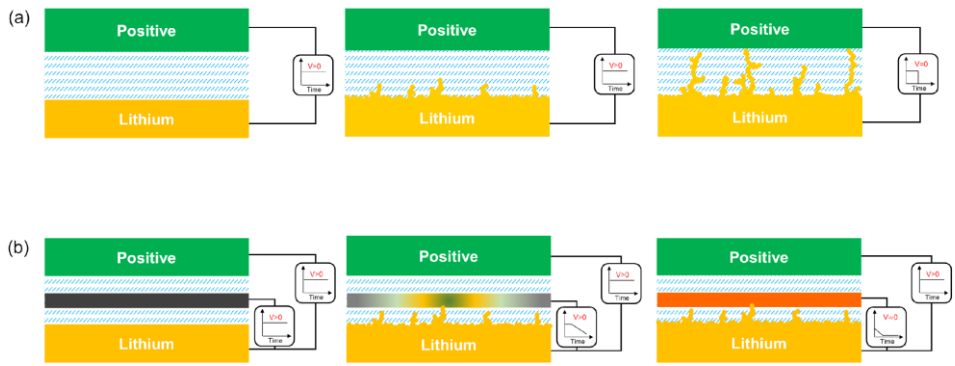

Figure 3.2.1. Schematic mechanism of an auxiliary electrode sensor for safe rechargeable lithium metal batteries. (a) In a conventional battery system, initially formed dendric seeds will grow and create an internal circuit across the separator positioned between the two electrodes, causing to voltage of the battery to drop to 0 V (*vs.* Li/Li^+). (b) With the aid of auxiliary electrode, growing lithium dendrites will reach at auxiliary electrode before they make connection with the positive electrode. Lithium dendrites will not grow further while the auxiliary electrode consumes lithium ions. The reaction of the auxiliary electrode with lithium ions signals danger before a catastrophic event occurs with no damage to the battery.

3.2.2. Synthesis of free-standing graphite auxiliary electrode

Taking all these requirements into consideration, we selected free-standing, flexible and thin graphite layers and prepared them as described in Figure 3.2.2 and 3.2.3. Graphite is well-known to be capable of up-taking lithium ions at reasonably fast rate, with its capacity well-documented[20]. Moreover, the degree of lithiation is clearly observable from 3 V to nearly 0 V with the well-defined voltage plateau and a color change of the graphite (Figure 3.2.4)[21, 22]. In this work, the free-standing

film of graphite was fabricated using poly(vinylidene fluoride-co-hexafluoropropylene) (PVDF-HFP) with the mass ratio of 3:7 (PVDF-HFP : graphite) in 20 μm thickness, considering the reasonable holding time of lithium growth at various current rates in a practical cell as presented in Figure 3.2.5. It should be also noted that such thin free-standing auxiliary graphite electrode still guarantees much higher gravimetric and volumetric energy density of lithium metal anode in spite of the additional weight of the auxiliary electrodes, as comparatively demonstrated in Supplemental Table 3.2.1 and 3.2.2. The electrolyte permeability of the thin layer was confirmed through a simple dropping test of the electrolyte. The images in Figure 3.2.6 show that the fabricated flexible graphite layer has better wettability than the separator[23, 24]. The effect of the auxiliary electrode on lithium ion mobility in the cell was quantitatively analyzed using Electrochemical Impedance Spectroscopy (Figure 3.2.7)[25]. The influence of the auxiliary graphite layer on the ionic conductivity in the cell was negligible with a decrease of 0.12 mS cm^{-1}.

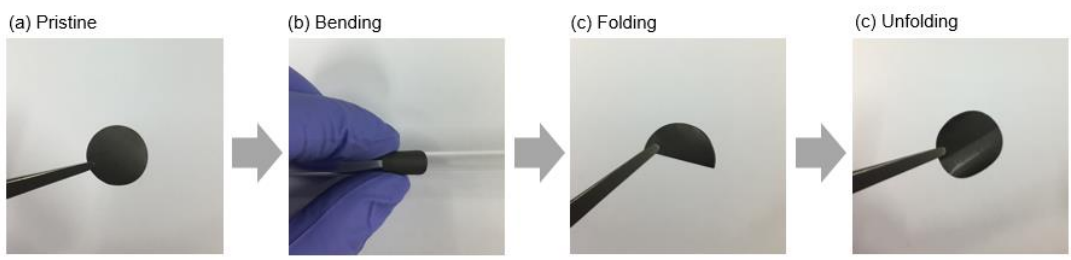

Figure 3.2.2. Images of a flexible graphite layer with 30% PVDF-HFP and 70% flake graphite composition. The pristine graphite layer was not torn and damaged by bending and folding.

Figure 3.2.3. Fabrication processes of a thin graphite layer are described step by step.

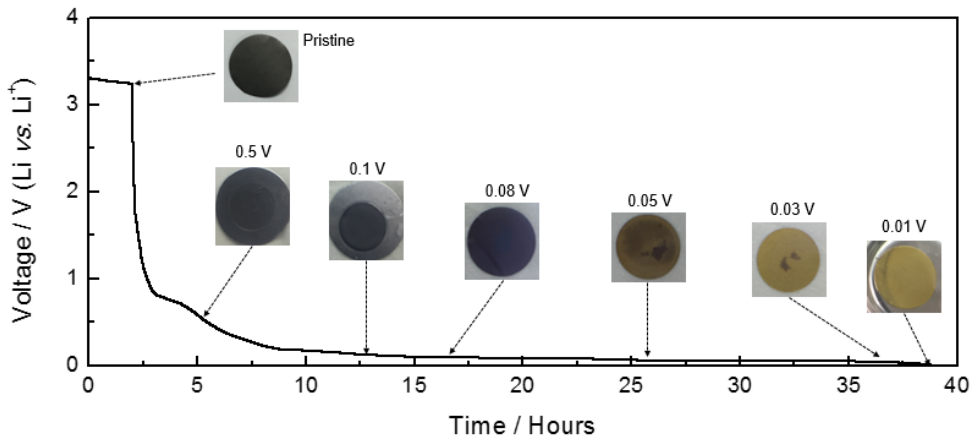

Figure 3.2.4. Typical potential profile of a graphite layer with color change of graphite by lithiation. The pristine graphite layer that is fully de-lithiated is black in color. The color of graphite layer becomes yellow with lithiation. Each cell was discharged with a current density of 10 mA g^{-1} to its cut-off voltage and disassembled to obtain graphite images.

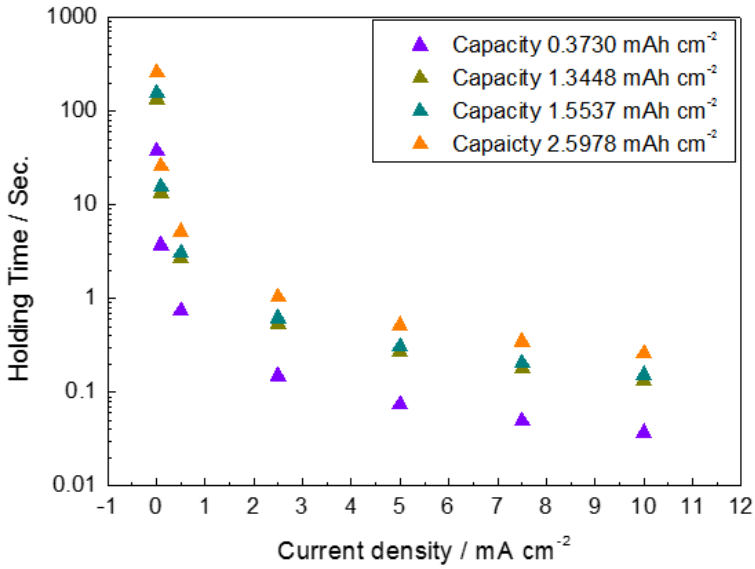

Figure 3.2.5. The delay time that can suppress the growth of lithium dendrite depending on the current density. The larger the capacity of the auxiliary electrode, the longer the allowable dendrite growth delay time.

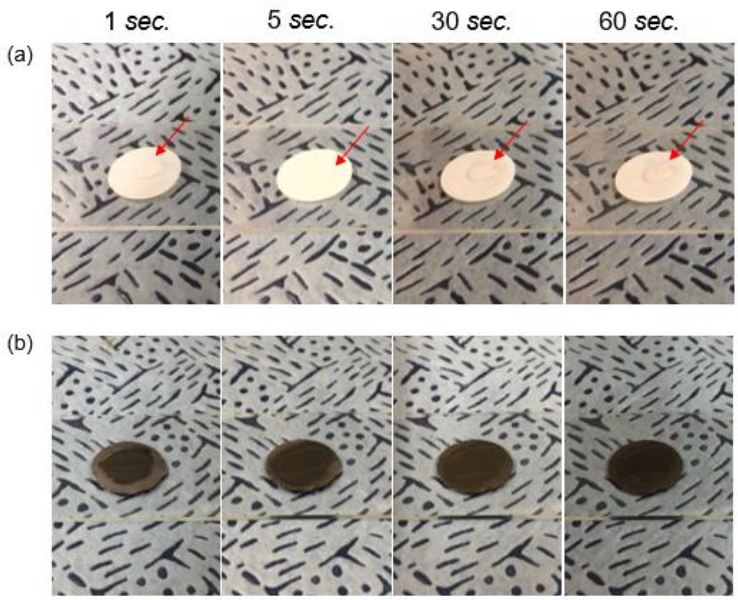

Figure 3.2.6. Images showing the contact angle of dropped electrolyte on (a) separator and (b) an auxiliary graphite layer. The electrolyte on the separator maintains a high contact angle for up to 60 seconds. Conversely, as soon as the

electrolyte was dropped onto the graphite layer, it penetrated the graphite layer.

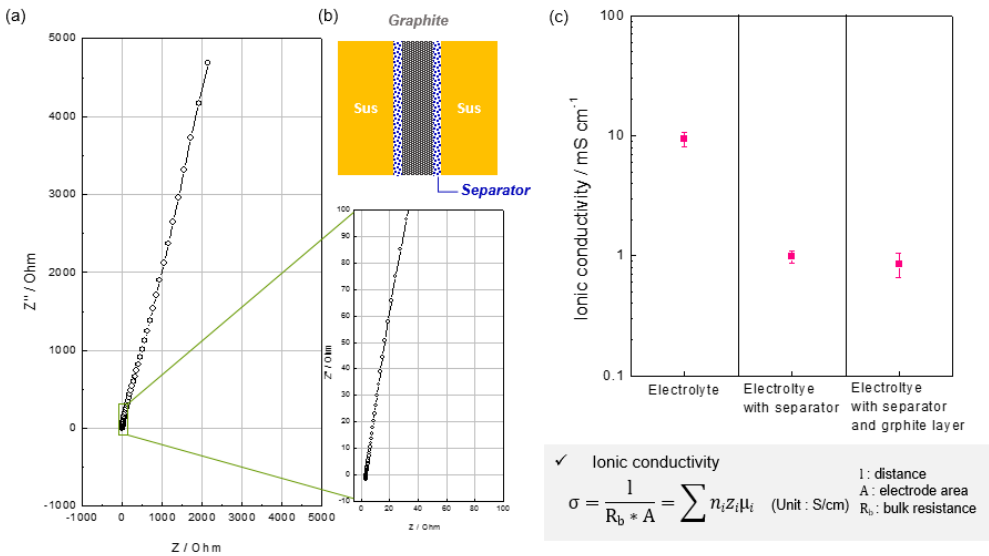

Figure 3.2.7. (a) Nyquist plot of a SUS-SUS symmetric cell with a graphite layer between the plates. (b) A schematic illustration of the cell configuration to measure EIS. Due to the electronic conductivity of the graphite layer, two separator sheets on each side were used to block the electronic path. (c) Ionic conductivity is measured in various cell configurations to determine the effect of each component.

The intercept of the x-axis generally represents bulk resistance, which is mainly influenced by ionic conductivity. In this system, the distance (l) and area (A) are set to the component thickness between the two stainless steel substrates and the area of the stainless steel substrate, respectively. Thus, the bulk resistance can be converted into ionic conductivity using the equation in Figure 3.2.7. To measure the conductivity of the pure electrolyte, a constant distance and area are fixed between two SUS plates by inserting a donut type Teflon ring. Figure 6c shows the ionic conductivity in three different cases. The ionic conductivity of the pure electrolyte was approximately 10 mS cm^{-1}, which is consistent with previous

reports. (Journal of Power Sources, 196, 9743-9750, 2011). Additional conductivity measurements were performed with and without graphite layers between the separators to determine the effect of only the thin graphite layer located between the separators on the ionic conductivity. The presence of separator result in a lower ionic conductivity (0.98 mS cm^{-1}) due to its low porosity, which inhibited the movement of lithium ions through the separator. However, an additional thin graphite layer inserted between two separators did not seem to significantly affect the Li ion mobility (0.86 mS cm^{-1}).

3.3. Results and discussion

3.3.1. Direct in-situ measurement of Li growth in 3 electrode

A detailed function of an auxiliary electrode was verified through *in situ* observations of dendrite growth in lithium metal cell. We prepared a home-made lithium cell to enable capture of images of dendrite growth while measuring auxiliary electrode potential, as illustrated in Figure 3.3.1a. Voltage profiles of V1 (between lithium and copper) and V2 (between lithium and the auxiliary electrode) were simultaneously monitored. Initially, the measured voltages, V1 and V2, were 0 V and ~3 V, respectively, presenting an initial potential difference between the two electrodes. As soon as the current was applied, it was observed that lithium ions began to deposit on the copper, and V1 rapidly fell below 0 V (~ -0.8 V) due to the overpotential. However, V2 remained almost unchanged from the initial voltage at nearly 3 V because the graphite layer is disconnected from the electric circuit. Figure 3.3.1b shows that, with the continuous current flow in the circuit, the

lithium metal deposits irregularly on the surface of the copper foil, and finally makes a contact with the auxiliary graphite layer after about 10 minutes. It is evident from Figure 3.3.1c that, at the moment of the contact between the lithium metal protrusion and the auxiliary electrode, a sudden voltage drop of V2 can be observed, while a small voltage change of V1 is detected (this will be discussed in detail later), which contrasts to a system without the auxiliary electrode[26] in Figure 3.3.2. The change of V2 is ascribed to the gradual lithium intercalation into the graphite auxiliary electrode, which alters the lithium chemical potential in the auxiliary electrode, thus the potential difference between the two electrodes. It implies that the lithium gradually intercalates into the auxiliary electrode. However, it is worth noting that the lithium intercalation to the graphite can take place from both of the lithium sources, once the lithium protrusions are in electrical contact with the graphite layer; (i) chemical lithiation from the lithium protrusions and (ii) partial electrochemical lithiation from lithium metal electrode through the electrolyte. Since the graphite layer becomes a part of the electrical circuit, the electrochemical lithiation into graphite gets possible, which is thermodynamically preferable than being electroplated as lithium metal on the lithium metal electrode. These two processes simultaneously contribute to suppressing the further growth of lithium protrusion. The chemical lithiation into graphite from the lithium protrusion scavenges the protrusion itself, and the further lithium deposition on the lithium metal electrode is temporarily halted by the electrochemical lithiation of the graphite layer.

More careful investigation of the V1 and V2 profiles supports the idea that the auxiliary electrode played a role of a lithium dendrite scavenger. Figure 3.3.1d

depicts the detailed voltage evolutions of V1 and V2 for the initial a few minutes after the contact, showing a close correlation between the two. While V2 continues to drop to 0 V for this period of time, slight perturbations appear intermittently for both V1 and V2. And, it is noteworthy that the peak in V1 profile coincides with the step-wise drop of V2. We believe it is due to the repeated formation and removal of dendrites, forming and breaking an electric circuit. After the first contact by the formation of the dendrite, the instantaneous drop in V2 is followed by a small peak at 10.7 minutes marked as black star in Figure 3.3.1d (*i.e.* the instantaneous reduction in the overpotential of V1) in V1. And, at 11.2 and 11. 45 minutes marked as black star in Figure 3.3.1d, the small peaks in V1 are accompanied by the faster decrease of the V2 voltage. The decrease of the overpotential in V1 upon the contact is likely to be caused by the reduction in the effective anode-cathode distance owing to the electrical contact [27]. And, if more dendrites are generated penetrating into the auxiliary electrode, they provide additional electronic bridges by which electrons can pass, resulting in a further decrease of the overpotential in V1 and faster lithium intercalation into graphite (more rapid reduction in V2 voltage), as presented with green colors in Figure 3.3.1d.

On the other hand, if the dendrites are consumed by the chemical lithiation and thus are removed from the auxiliary electrode, the overpotential in V1 would reappear, as illustrated with grey regions in Figure 3.3.1d. This scavenger role of the auxiliary electrode continued until it was completely lithiated, which is further supported by the additional *ex situ* and *in situ* Li-Li symmetric cell results in Figure 3.3.3 and Supporting Video 1. It should be noted that, as a result, there was no

dendritic lithium penetration to the opposing lithium electrode even after 23 minutes of constant discharging (Figure 3.2.8e).

The results above indicate that not only V2 but also V1 is notably altered, when the dendrite contacts to the auxiliary electrode even though there is no electrical shorting between positive electrode and negative electrode. It implies that in a conventional cell without an additional apparatus to monitor the V2, it might be simply possible to detect the dendrite signal from the change in the nominal voltage (V1) of the cell when the auxiliary electrode begins to scavenge them.

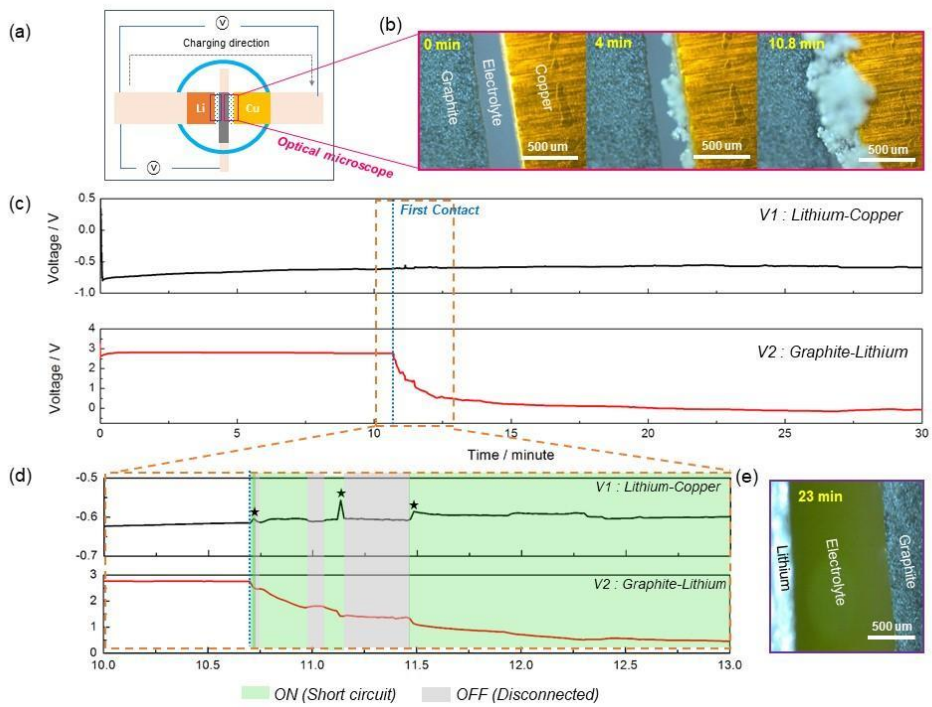

Figure 3.3.1. (a) Detailed cell configuration for *in situ* observations. (b) Images of the auxiliary electrode and positive electrode were taken over deposition time. A mossy-like lithium was observed on the copper foil that gradually grew over the time. (c) The voltage profile of both V1 $_{\text{Lithium-Copper}}$ and V2 $_{\text{Graphite-Lithium}}$ during electroplating on copper foil. (d) V1 $_{\text{Lithium-Copper}}$ and V2 $_{\text{Graphite-Lithium}}$ from 10 to 13

minutes. I Images of the area between the auxiliary electrode and negative electrode after 23 minutes. No trace of lithium deposition was observed, indicating that the mossy-like lithium did not penetrate the graphite layer.

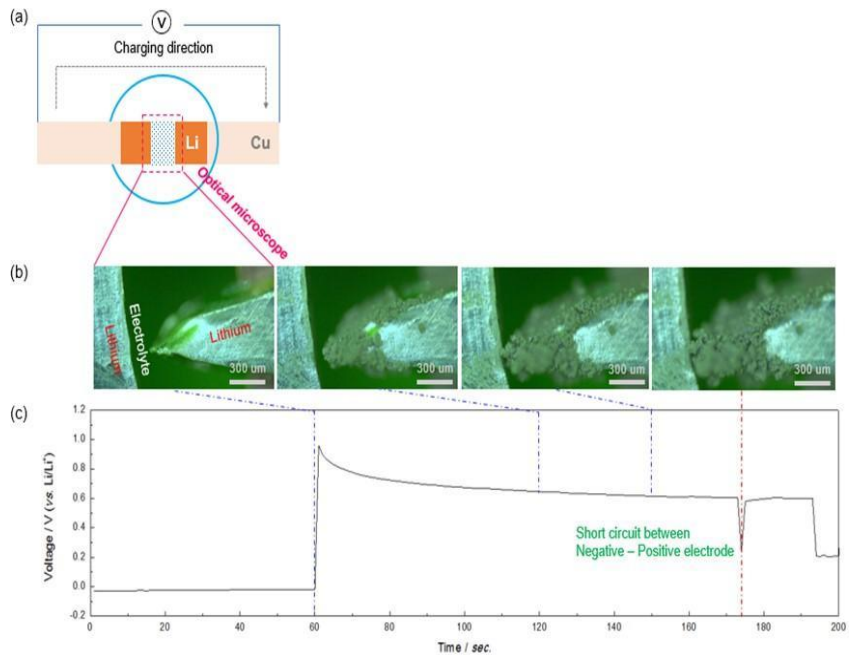

Figure 3.3.2. (a) A schematic illustration of cell configuration for *in-situ* optical measurement. (b) Optical microscopy images of the Li-Li symmetric cell were taken in galvanostatic mode. (c) Potential curve of Li-Li symmetric cell.

Two lithium metal slices were placed on both sides of the copper foil and electrodeposited with lithium in one direction. The initial voltage of between two electrodes was 0 V due to the symmetry of the cells. Once a current was applied, lithium ions were deposited on the lithium surface. The distance between the two lithium metals decreased due to the deposition of lithium metal as shown in Figure 3.2.9b. Finally, the growing lithium metal front contacted the opposite side lithium

metal, causing sudden voltage drop. However, since a large amount of current momentarily flowed through the internal short-circuit, the voltage drop recovered immediately the circuit was disconnected. Continuous electrodeposition of lithium ions creates more dendritic circuits, resulting in a stable voltage drop considered an internal short circuit.

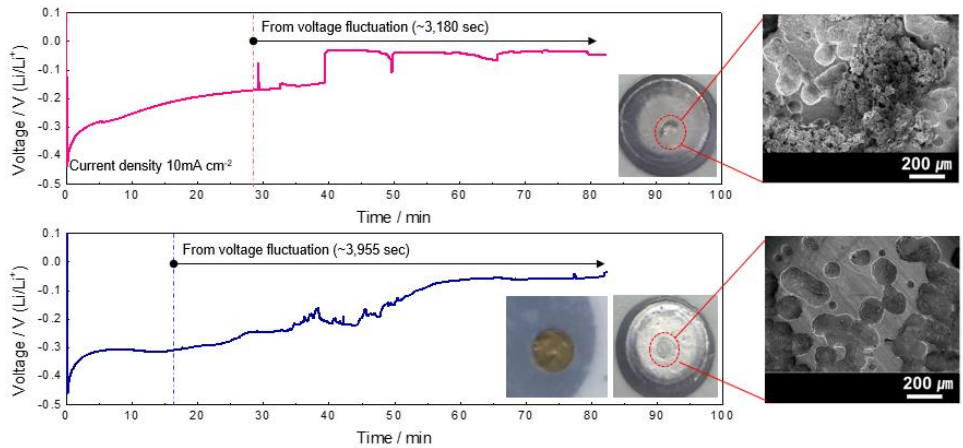

Figure 3.3.3. Typical potential profile and disassembly cell image of Li-Li symmetric cell (a) without a graphite auxiliary electrode (b) with a graphite auxiliary electrode.

The blockage of dendrite by an auxiliary electrode is further confirmed upon battery disassembly analysis. To induce the electroplating of lithium ions on the opposite electrode, we fabricate coin cells with a hollow area between two electrodes with no separators. For the smart battery system containing an auxiliary electrode, the flexible graphite layer as auxiliary electrode was placed on the middle of the hollow area. Figure 3.2.10a presents a typical voltage profile of a Li-symmetric cell during the discharge process. At an initial stage, an activation energy of removal of oxide layer on lithium surface requires a higher overpotential,

up to 0.45 V at 10 mA cm^{-2}. This overpotential converges with a gradual decrease. The first voltage fluctuation was detected after 29 min, indicating the connection of internal circuit by lithium dendrites. A constant current continued to flow for up to 83 minutes to form enough dendrite to be observed after the first detection. An identical experiment was carried out on cells with auxiliary electrodes (Figure 3.2.10b). The first voltage changes in this case were rather undistinguishable and were detected twice as fast because these voltage fluctuations come from not contact between negative and positive electrodes, but from the connection between lithium and auxiliary electrodes located at a half distance between negative and positive electrodes. To confirm the occurrence of short circuit, the lithium electrodes on the side from which lithium ions were extracted during the discharge process were obtained by disassembling each sample. Without an auxiliary electrode, black spots on the dendrites were visually observed and were clearly identified as lithium dendrites by SEM imagery. Not only numerous pores were seen on the lithium surface associated with lithium ion extraction sites, but also lithium deposition morphologies were also found. In contrast, the lithium surface obtained from the cell containing an auxiliary electrode was slightly darkish throughout the entire reaction zone, but had no black spots at all. Furthermore, only pores were observed on the lithium surface through the SEM photograph, while the graphite layer changed to yellow which indicating lithiation of the graphite. Based on the pore images and discoloration of graphite layer, it is inferred that additional lithium ions were not consumed by formation of lithium dendrite. It was consumed for reactions with the auxiliary electrode resulting in the blockage of hazardous dendrite growth

3.3.2. Auxiliary electrode in 2 electrode coin cell configuration

To verify this, we assembled a conventional coin-type cell without an apparatus monitoring V2 and tested the cell in a practically high current rate using a lithium metal negative electrode and a graphite positive electrode in Figure 3.3.4a. The graphite was chosen as a model positive electrode because its characteristic voltage profile is well documented with a minimum variation of the specific capacity at a given voltage range, which is beneficial in monitoring the distinctive voltage changes in the cell. We first discharged the cell at a low current density of 10 mA g^{-1}, *i.e.*, lithiation of graphite positive electrode and stripping of the lithium metal negative electrode, which showed the characteristic lithiation voltage profile of the graphite [28]. (Figure 3.3.4) Then, the electrochemical lithium deposition on the lithium metal negative electrode was carried out by charging the cell at a high current density of 1000 mA g^{-1} to trigger the lithium dendrite formation and growth. Figure 3.3.4b presents the electrochemical profile of the charging, which is followed by the discharging. During a charging process, a sudden voltage drop was detected at ~ 1100 seconds, corresponding to approximately 300 mAh g^{-1} (denoted by the asterisk in Figure 3.3.4c), which hints at a dendrite penetration into auxiliary electrode as discussed. Interestingly, after the perturbed cell voltage, the continued charging of the cell did not lead to the prolonged fluctuations of the profile, which is typically observed in the conventional cell after the short-circuit thus failing in charging the cell and aggravating the cell heating [29, 30]. Moreover, when continued with the second discharge at 10 mA g^{-1}, we did not observe any abnormal discharge behavior.

To elucidate the underlying reason for the perturbed cell voltage denoted with asterisk, we disassembled the cell after the second discharge, as shown in Figure 3.3.4c. It revealed that some dark spots are clearly observable on the separator (anode-facing separator) between the lithium electrode and auxiliary electrode, which is the signature of the dendrite short-circuit. More importantly, the auxiliary electrode exhibited yellow domains at the identical region corresponding to the dark spots on the anode-facing separator. It evidently demonstrates that the auxiliary layer was partially lithiated by dendrites, and the region served as a temporary lithium reservoir. On the other hand, the separator (cathode-facing separator) between the graphite positive electrode and auxiliary electrode did not show any noticeable change, maintaining a clean surface, which confirms that the positive electrode was well protected against the risk of short-circuiting. It suggests that without an apparatus to monitor the V2 of auxiliary electrode, it is feasible to detect the signals of the dendrite growth in a full cell by simply measuring the full cell voltage, carefully probing the reduction of the overpotential when a high current rate is applied. And, this process is not accompanied by the internal shortage between the positive and negative electrodes even with the extended charging process , because the auxiliary electrode continuously scavenges the lithium penetration and serves as an additional lithium reservoir for a certain period of time. It proposes that the concept of auxiliary electrode for sensing can be applied even for the conventional two-electrode systems, while maintaining its scavenging role, thus retarding the safety hazards.

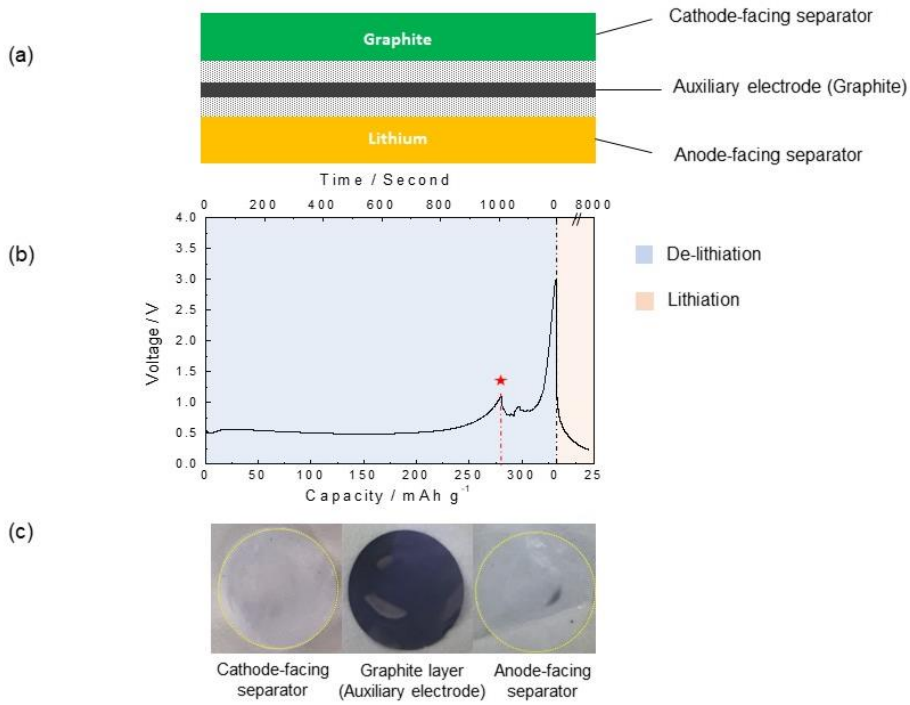

Figure 3.3.4. (a) Schematic of the cell configuration. (b) The first charge voltage profile with a 1000 mA g^{-1} current density and a second charge voltage profile with a 10 mA g^{-1} current density. (c) Images of separators and auxiliary electrodes from a disassembled cell.

3.4. Conclusion

A rechargeable lithium metal battery with reduced safety risk was demonstrated by employing a bifunctional auxiliary electrode. The auxiliary electrode was capable of not only detecting signals of a short-circuit hazard, but also hampering further dendrite growth by scavenging the lithium dendrite in a lithium metal battery. It was confirmed that the auxiliary electrode has no detrimental effect on battery performance with a minimal sacrifice in the energy density, and is activated only when batteries are exposed to the risk of short-circuit. Furthermore, the

feasibility of the auxiliary sensor in a full cell was verified, showing the promise in its applicability to the practical batteries. This report provides an interesting new concept of auxiliary electrode that is capable of sensing and retarding the lithium dendrite growth in lithium metal electrodes, and opens up unexplored pathways of using various auxiliary electrode chemistry toward the development of practical lithium metal batteries.

3.5. Reference

1. B. Dunn, H. Kamath and J.-M. Tarascon, *Science*, 2011, **334**, 928-935.

2. M. Armand and J.-M. Tarascon, *Nature*, 2008, **451**, 652-657.

3. J.-M. Tarascon and M. Armand, *Nature*, 2001, **414**, 359-367.

4. D. Lin, Y. Liu and Y. Cui, *Nature Nanotechnology*, 2017, **12**, 194-206.

5. W. Xu, J. Wang, F. Ding, X. Chen, E. Nasybulin, Y. Zhang and J.-G. Zhang, *Energy Environ. Sci.*, 2014, **7**, 513-537.

6. P. Bai, J. Li, F. R. Brushett and M. Z. Bazant, *Energy Environ. Sci.*, 2016, **9**, 3221-3229.

7. P. Bai, J. Guo, M. Wang, A. Kushima, L. Su, J. Li, F. R. Brushett and M. Z. Bazant, *Joule*, 2018, **2**, 2434-2449.

8. D. P. Finegan, M. Scheel, J. B. Robinson, B. Tjaden, I. Hunt, T. J. Mason, J. Millichamp, M. Di Michiel, G. J. Offer, G. Hinds, D. J. L. Brett and P. R. Shearing, *Nat. Commun.*, 2015, **6**, 6924.

9. D. P. Finegan, E. Darcy, M. Keyser, B. Tjaden, T. M. M. Heenan, R. Jervis, J. J. Bailey, R. Malik, N. T. Vo, O. V. Magdysyuk, R. Atwood, M. Drakopoulos, M. DiMichiel, A. Rack, G. Hinds, D. J. L. Brett and P. R. Shearing, *Energy*

Environ. Sci., 2017, **10**, 1377-1388.

10. K. N. Wood, E. Kazyak, A. F. Chadwick, K.-H. Chen, J.-G. Zhang, K. Thornton and N. P. Dasgupta, *ACS Cent. Sci.*, 2016, **2**, 790-801.
11. T. Nishida, K. Nishikawa, M. Rosso and Y. Fukunaka, *Electrochim. Acta*, 2013, **100**, 333-341.
12. F. Ding, W. Xu, G. L. Graff, J. Zhang, M. L. Sushko, X. Chen, Y. Shao, M. H. Engelhard, Z. Nie and J. Xiao, *J. Am. Chem. Soc.*, 2013, **135**, 4450-4456.
13. Y. Lu, Z. Tu and L. Archer, *Nat. Mater.*, 2014.
14. J. Zheng, M. H. Engelhard, D. Mei, S. Jiao, B. J. Polzin, J.-G. Zhang and W. Xu, *Nat. Energy*, 2017, **2**, 17012.
15. C.-P. Yang, Y.-X. Yin, S.-F. Zhang, N.-W. Li and Y.-G. Guo, *Nat. Commun.*, 2015, **6**.
16. L.-L. Lu, J. Ge, J.-N. Yang, S.-M. Chen, H.-B. Yao, F. Zhou and S.-H. Yu, *Nano Lett.*, 2016, **16**, 4431-4437.
17. H. Lee, D. J. Lee, Y.-J. Kim, J.-K. Park and H.-T. Kim, *J. Power Sources*, 2015, **284**, 103-108.
18. G. Zheng, S. W. Lee, Z. Liang, H.-W. Lee, K. Yan, H. Yao, H. Wang, W. Li, S. Chu and Y. Cui, *Nature Nanotechnology*, 2014, **9**, 618-623.
19. H. Wu, D. Zhuo, D. Kong and Y. Cui, *Nat Commun*, 2014, **5**, 5193.
20. J. Billaud, F. Bouville, T. Magrini, C. Villevieille and A. R. Studart, *Nat. Energy*, 2016, **1**, 16097.
21. S. J. Harris, A. Timmons, D. R. Baker and C. Monroe, *Chem. Phys. Lett.*, 2010, **485**, 265-274.
22. P. Maire, A. Evans, H. Kaiser, W. Scheifele and P. Novák, *J. Electrochem. Soc.*, 2008, **155**, A862-A865.

23. S. S. Zhang, *J. Power Sources*, 2007, **164**, 351-364.

24. T.-H. Cho, M. Tanaka, H. Onishi, Y. Kondo, T. Nakamura, H. Yamazaki, S. Tanase and T. Sakai, *J. Power Sources*, 2008, **181**, 155-160.

25. Y.-J. Kim, H. Lee, H. Noh, J. Lee, S. Kim, M.-H. Ryou, Y. M. Lee and H.-T. Kim, *ACS Appl. Mater. Interfaces*, 2017, **9**, 6000-6006.

26. M. Rosso, C. Brissot, A. Teyssot, M. Dollé, L. Sannier, J.-M. Tarascon, R. Bouchet and S. Lascaud, *Electrochim. Acta*, 2006, **51**, 5334-5340.

27. J. R. Owen, *Chem. Soc. Rev.*, 1997, **26**, 259-267.

28. V. A. Sethuraman, L. J. Hardwick, V. Srinivasan and R. Kostecki, *J. Power Sources*, 2010, **195**, 3655-3660.

29. X. Liang, Q. Pang, I. R. Kochetkov, M. S. Sempere, H. Huang, X. Sun and L. F. Nazar, *Nat. Energy*, 2017, **2**, 17119.

30. L. Li, S. Basu, Y. Wang, Z. Chen, P. Hundekar, B. Wang, J. Shi, Y. Shi, S. Narayanan and N. Koratkar, *Science*, 2018, **359**, 1513.

Chapter 5: Concluding remarks

As part of this thesis research, three main issues that arise with lithium metal anode-free batteries were addressed. These are:

1. The non-uniform electric distribution on the current collector,
2. The non-uniform characteristics of the SEI layer,
3. The use of a technique to prevent short-circuiting.

Ultimately, the research was successful in addressing the issues in each area, which clearly elucidated the root cause. The performance and safety of the Li anode-free battery was successfully improved. **The first section** of this thesis is devoted to investigation of local current distribution on current collectors and the application of the dielectric constant to solve this problem. Experiments were conducted to better understand the effect of the dielectric constant of SEI on the local distribution. A new type of artificial SEI layer with a different dielectric constant was created to better understand the effect of the dielectric constant of SEI on local distribution in this experiment. In this study, I also demonstrate the behavior of Li deposition in a variety of area capacities ranging from 0.5 to 10 mAh/cm^2, to investigate the behavior of Li plating in each sample. Furthermore, we employed a COMSOL simulation to better understand how the dielectric constant affects the behavior of Li deposition. **In the second section**, a simple method is described for removing the unwanted organic SEI layer leaving only the inorganic portion of the layer remaining. Known for being uniform, difficult to dissolve in an electrolyte with stability throughout the cycle, the inorganic component is well-suited for this application. It has been shown that the SEI monolayer can be tuned to increase the cycle performance by more than four times in the Li/Cu system. In

the final section, a sensor application for use in a Li-metal anode-free battery configuration was examined. A model was developed for a critical Li metal anode-free sensor that enabled its fabrication. It was found that graphited film was the most appropriate sensor material to investigate. Graphited film has the ability to chemically absorb Li metal into its structure, causing the voltage to change. With an outer voltammeter, detection of the changing voltage was more easily detected. This enables recognition that a Li dendrite has reached the sensor separator, which is important information. Then it is possible to remove the lithium metal battery from service before thermal runaway occurs.

In conclusion, a rational study with a fundamental strategy for developing superior lithium-metal/anode-free batteries was done and successful further examination of three main issues of lithium-metal/anode-free batteries was conducted in this thesis. I was able to elucidate three clear solutions of the original problems in lithium-metal/anode-free batteries, both experimentally and by simulation. Moreover, these three critical issues of lithium-metal anode-free batteries are addressed. The result is that significantly improved battery performance and safety system were achieved. This approach provides valuable guidelines for designing efficient lithium-metal/anode-free batteries. In future development, we can design lithium-metal/anode-free batteries that incorporate these three solutions in a single battery, providing superior performance and enhancing safety.

Abstract in Korean

초록

에너지의 수요 및 에너지 사용량이 기하급수적으로 증가함에 따라, 기후 변화와 대기 이산화탄소 양의 증가 등의 환경적인 문제가 대두되고 있다. 대체에너지 자원이 기존의 화석 연료를 대신할 새로운 에너지원으로써 부상하고 있으나, 지속적인 전력 공급이 힘들어 에너지 효율이 낮다는 문제점이 있다. 따라서 보다 작고 간편하면서도 효율적인 에너지 저장소가 요구되었으며, 이에 맞추어 휴대전화, 노트북, 전기 자동차와 같은 휴대용 전력을 위해 개발된 기술 역시 진보하고 있다. 그러나 리튬 이온 배터리와 같은 현존하는 에너지 저장 방식의 효율성이 충분하지 않기에, 증가한 전력 수요를 감당하기 위한 새로운 배터리가 필요하게 되었으며, 그 중 하나로 무음극 전지가 주목을 받고 있다. 무음극 전지는 가벼운 무게와 높은 용량, 낮은 전압대를 가짐으로써 매력적인 차세대 에너지 저장 기술로 여겨지고 있지만, 수명 특성과 쿨롱 효율이 상대적으로 낮고, 무엇보다 안전성 문제로 인해 상용화에 어려움을 겪고 있다. 이는 음극이 없는 무음극 전지의 내부 구조로 인해, 양극재에서 나온 리튬 이온이 리튬 메탈이나 집전체 표면에만 쌓여야 한다는 현상에서 기인한 문제점들로 알려져 있다. 음극 표면에 리튬 이온이 대체적으로 불균일하게 침전됨에 따라 전해질과 양극 리튬 소스의 소모가 가속화되어, 종국에는 전해질의 고갈과, 낮은 쿨롱 효율에 따른 짧은 수명을 야기한다. 또한 리튬 이온의 불규칙적인 이동은 리튬 dendrite를

형성하며, 분리막을 뚫고 양극과 닿게 되면 단전 현상과 줄열에 따른 열화가 발생할 수 있다. 이러한 불규칙적인 리튬 이온의 침전의 원인은 크게 두 가지로 꼽히고 있다. 첫 번째로, 집전체나 리튬 박막 음극의 표면이 매끄럽지 못해 집전체 표면에 국부적인 전류 밀도의 집중이 발생하며, 이는 결과적으로 국부적인 리튬 이온의 침전을 야기한다. 전기화학적 반응에 따라 자발적으로 형성되는 SEI층 역시 그 표면이 불규칙하고 표면 특성을 제어하기 힘들어, 리튬이 불균일하게 쌓이는 원인이 될 수 있다. 이로 인해 발생한 리튬 덴드라이트는 사이클이 지나면서 전해질과 리튬 소스를 소모하며 성장해 양극에 도달하게 되며, 단전 현상이 일어나 덴드라이트로 전자가 이동하며 열적 열화와 폭발이 일어날 수 있다. 위에서 언급된, 리튬 메탈 무음극 전지에서의 세 가지 주요한 문제점들을 해결하기 위해 본 연구자는 폭넓은 연구를 수행했다. 본 연구의 파트 1에선 두 가지 전략을 이용해 리튬 이온의 균일한 침전을 유도할 수 있는 방안을 다뤘으며, 그 중 첫 번째가 높은 유전율의 SEI층의 도입을 통한 국부 전류 집중의 방지이다. 고유전율 고분자로 이루어진 SEI층을 집전체에 코팅함에 따라 리튬이 균일하게 도포되고, 표면에서의 과전압과 리튬 돌출 현상, 국부 전류 밀도가 감소하였다. PVDF (polyvinylidene difluoride) 유전 물질의 결정성을 조절함에 따라 리튬 침전 현상을 제어할 수 있으며, 유전체 나노입자를 도입한 PVDF 필름 (LiF-PVDF)은 높은 유전율의 R-PVDF 상을 형성해 리튬의 침전/용출을 균일화한다 두 번째 전략은 불균일한 SEI 층이 전지에 가하는 영향을 분석하고 이해하는 것에서 출발한다. 리튬 이온 배터리나 무음극 전지에선 SEI층이 전지 효율에 지대한 영향을 미친다. 전극 근처에서 전해질이

환원되고 분해되면서 생긴 SEI층으로 인해 리튬 메탈의 전기화학 전위가 0 V 이하로 감소하며, 유/무기의 나노 결정으로 이루어진 SEI층은 조성의 제어가 매우 힘들고 기계적 성질과 이온 전도도가 불균일해 불안정한 리튬 침전을 야기한다. 따라서 쿨롱 효율과 사이클 수명이 급감하고, 전지에서의 화재 발생 가능성이 높아진다. 본 연구에선 간단한 전기화학적 폴리싱을 이용해 나노 유기 결정체를 제거함으로써 견고하고, 균일한 이온 전도도를 가진 단일 무기물 SEI 층을 제작했다. 극저온 전자현미경 (Cryo-TEM)과 전자 에너지 손실 분광법 (EELS), 심층 XPS 분석을 통해 무결점의 단일층 무기 SEI층을 검증하였고, 이에 따른 균일한 리튬 침전/용출을 확인하였다. 파트 2에선 내부 단전을 감지해 리튬 메탈 덴드라이트 형성에 따른 전지의 고장을 막기 위해 리튬 이차 전지에 보조 전극을 도입했다. 보조 전극은 안전 센서와 리튬 스캐빈저를 포함하며, 유연하면서도 self-standing한 소재를 이용해 실시간으로 단전을 감시하고 추가적인 덴드라이트 성장을 효과적으로 막을 수 있다. 이는 안전한 리튬 메탈 이차 전지의 적용 가능성을 확대할 수 있는 연구이다. 결론적으로, 위의 연구들로 하여금 새로운 리튬 메탈 무음극 전지의 상용화에 가치 있는 새로운 과학적 지식이 더해지기를 바라며, 인류를 위한 기술이 한 층 더 환경 친화적으로 발전하는 밑거름이 되기를 소망한다.

학번: 2016-22080

Curriculum Vitae (CV)

Contact Information

Department of Materials Science and Engineering, Building 31 Research Institute of Advanced Materials Seoul National University 1 Gwanak-ro, Gwanak-gu, Seoul, Republic of Korea

Mail: auy2006@gmail.com

Phone: +82-2-880-7165

Cell: +82-10-9466-6062

Education

Ph.D. Department of Materials Science and Engineering – Seoul National University 3/2016 – Advisor: Prof. Kisuk Kang

B.S. Department of Materials Science and Engineering – Khon Kaen University 3/2011 - 8/2015 Major subject GPA: 3.42/4

Publications (1st author)

† denotes equal contributions

[1] Tamwattana, O.; Bai, S.; Park, H.; Kim, B.; Jang, H.; Kang, K. "Dual-function artificial solid electrolyte interface layer for high-efficiency anode-free batteries" , In preparation, 2022.

[2] Tamwattana, O.; Park, H.; Park, H.; Kim, J.; Kim, B.; Park, J.;Kang, K. "Leaching Organic solid electrolyte interface by Electrochemical Dissolution Leads to monolithic inorganic SEI and Enhancing Cycle Stability for Anode Free Battery", In preparation, 2022.

[3] Tamwattana, O.; Park, H.; Kim, J.; Hwang, I.; Yoon, G.; Hwang, T.-H.; Kang,

Y-S.; Park, J.; Meethong, N.; Kang, K. “High-Dielectric Polymer Coating for Uniform Lithium Deposition in Anode-Free Lithium Batteries”, ACS energy letters, 2021, 6(12), 4416.

[4] Park, H.†; Tamwattana, O.†; Kim, J.; Buakeaw, S.; Hongtong, R.; Kim, B.; Khomein, P.; Liu, G; Meethong, N.; Kang, K. “Probing Lithium Metals in Batteries by Advanced Characterization and Analysis Tools”, Advanced Energy Materials, 2021, 11(15), 2003039.

[5] Moon, S.†; Tamwattana, O.†; Park, H.; Yoon, G.; Seong, W. M.; Lee, M. H.; Park, K-Y.; Meethong, N.; Kang, K. “A bifunctional auxiliary electrode for safe lithium metal batteries”, Journal of materials chemistry, 2019, 7(43), 24807.

Publication (Participating author)

[6] Bai, S.†; Kim, B.†; Kim, C.; Tamwattana, O.; Park, H.; Kim, J.; Lee, D.; Kang, K. “Permselective metal–organic framework gel membrane enables ultralong-life cycling of rechargeable organic batteries”, Nature Nanotechnology, 2021, 16, 77.

[7] Eum, D.†; Kim, B.†; Kim, S. J.; Park, H.; Wu, J.; Cho, S.-P.; Yoon, G.; Lee, M. H.; Jung, S.-K.; Yang, W.; Seong, W. M.; Ku, K.; Tamwattana, O.; Park, S. K.; Hwang, I.; Kang, K. “Voltage decay and redox asymmetry mitigation by reversible cation migration in lithium-rich layered oxide electrodes”, Nature Materials, 2020, 19(4), 419.

[8] Kim, J.†; Kim, H.; † Lee, S.; Kwon, G.; Kang, T.; Park, H.; Tamwattana, O.; Ko, Y.; Lee, D.; Kang, K. “A p–n fusion strategy to design bipolar organic materials for high-energy-density symmetric batteries”, Journal of Materials Chemistry A, 2019, 9(25), 18380.

[9] Xu, Z-L.†; Yoon, G.; Park, K-Y.; Park, H.; Tamwattana, O.; Kim, S.; Seong W.

M.; Kang, K. “Tailoring sodium intercalation in graphite for high energy and power sodium ion batteries”, Nature Communications, 2019, 10(1), 2598.

Patents

[10] Kang, K.; Tamwattana, O.; Park, H.; Kim, J.; Yoon, G. “Negative electrode for rechargeable lithium battery and rechargeable lithium battery including same” (2021), KR. Patent No. 1020200114709, Korean Intellectual Property Office.

[11] Kang, K.; Lee, M-H.; Tamwattana, O. “Manufacturing method of lithium anode containing protection layer, lithium anode manufactured thereby and lithium secondary battery applied thereby” (2018), KR. Patent No. 1020160150455, Korean Intellectual Property Office.

[12] Kang, K.; Moon, S.; Park, H.; Yoon, G.; Tamwattana, O. “Secondary battery containing auxiliary electrode sensor and detection method for a short circuit of secondary battery” (2018), US. Patent No. 10,749,221, U.S. Patent and Trademark Office.

Presentations

[13] “Advanced safety sensor for lithium metal battery via bifunctional auxiliary electrode”, MRS Fall Meeting, Boston, USA, December, 2019